**Title**

The Exploitation and Mitigation of Flow Effects in MRI



**Author**

Ali, Fadil Abbas

**Publication Date**

2023

Peer reviewed|Thesis/dissertation

UNIVERSITY OF CALIFORNIA

Los Angeles

# The Exploitation and Mitigation of Flow Effects in MRI

A dissertation submitted in partial satisfaction

of the requirements for the degree

Doctor of Philosophy in Physics and Biology in Medicine

by

Fadil Abbas Ali

2023

ABSTRACT OF THE DISSERTATION

The Exploitation and Mitigation of Flow Effects in MRI

by

Fadil Abbas Ali
Doctor of Philosophy in Physics and Biology in Medicine
University of California, Los Angeles, 2023
Professor John Paul Finn, Chair

The central theme of this thesis is the inherent signal response to flow effects in magnetic resonance imaging (MRI). These effects can be seen as either an asset or a nuisance. The work detailed in the first specific aim exemplifies how flow effects can be used, by using arterial spin labeling to assess for peri-wound perfusion in and around foot ulcers of diabetic patient volunteers. Specific aims two and three aim to mitigate troublesome outflow artifacts in balanced steady-state free precession (bSSFP) imaging. Insight into the nature of k-space encoding in MRI is a prerequisite to posing solutions to address the problem. Therefore, I will review frequency and phase encoding in some detail to explain how outflow artifacts become misregistered during standard 2D bSSFP imaging. After the foundation of signal encoding is laid out, the work presented in the second specific aim narrates these effects as a through-slice aliasing, and proposes applying through-slice phase-encoding ("slice-encoding") to localize outflowing spins from contaminating the target slice. This slice-encoding scheme provides a proof-of-concept for removing outflowing spins, however its practicality is limited as the breath-hold duration scales linearly with the number of encoding steps. Before discussing the third aim, the thesis will recap key concepts in making use of the spatially-varying phased-

array channel sensitivity in MR imaging. The third specific aim explores the use of the NMR phased-array coil sensitivity profile to spatially encode for the outflowing spins, accelerating image acquisition relative to the slice-encoding steps approach. Aim 3 builds on the theory of parallel acquisition, but has novel features that are specific to goal of mitigating outflow artifact in bSSFP.

The dissertation of Fadil Abbas Ali is approved.

Xiaodong Zhong

Holden H. Wu

Michael McNitt-Gray

Michael Albert Thomas

Kim-Lien Nguyen

John Paul Finn, Committee Chair

University of California, Los Angeles

2023

*To my parents and Janet. . . .*

TABLE OF CONTENTS

# LIST OF FIGURES

# LIST OF TABLES

# ACKNOWLEDGMENTS

I am grateful for the many people who gave me their love and support during this journey.

I would like to begin thanking Dr. Peng Hu for bringing me into this program. Joining his lab was my first encounter with MRI. Peng's style of advising comes with a lot of freedom, which is daunting at first. Because of this freedom, I was able to learn how to solve interesting problems and grow as a researcher.

I would also like to thank Drs. Paul Finn and Kim-Lien Nguyen. The two of them took me under their wing when Peng took his opportunity abroad. It took time to adjust to the different atmosphere, but they put up with my antics, and encouraged me to continue on the track I was on before Peng left. Not many who change advisors mid-PhD have that, so I am grateful for them making it easier and for the plenty of constructive feedback that they both provided. They both always knew which direction to point me towards when I was stuck and made sure that I had resources available to make achievements that would put me in a position to graduate. Together, they provided a nurturing atmosphere for a PhD student to grow and learn.

Dr. Xiaodong Zhong provided plenty of MR physics advice and would sit and look at sequence code during his time as a Siemens scientist. I was glad to see him join UCLA as faculty and serve as a member of my committee.

Dr. Michael Albert Thomas always left his door open at Peter V. Ueberoth building, making himself available for discussion on principles of MR physics.

Dr. Holden Wu kindly agreed to serve on my committee and gave suggestions on my methods throughout my tenure here at UCLA.

Dr. Michael McNitt-Gray is head of PBM program and keeps up to date with many students'

works. He always showed support for me and checked in every once in a while. Him, Reth, and Dr. Magnus Dahlbom all make sure that every student is growing in a constructive work atmosphere.

Dr. Dan Ennis was my M219 professor and his lectures made me want to commit to an MRRL lab in the first place.

Dr. Kyunghyun Sung always appreciated the questions I would ask and would respond with his own questions to guide me to the answer. He is an excellent teacher and taught me a lot of MR Physics.

Heather Wilbur, our administrative assistant, holds MRRL together and makes sure everything is running smoothlly.

While doing work at the scanners, I often ran into people including Dr. Victor Sigalov, Dr. Arash Bedayat, Dr. Ashley Prosper, Reevea McCollins, Sergio, Francine, Joy, Jung Sik, Brendan, Nick, and Mario. These people always provided their help when I needed help on the machine. I would like to extend many thanks to Dr. Yan Wu for **always** telling me what to do when I the scanner shut down or glitched during my experiments.

I also would like to thank my office mates, which include people in Ueberoth and MP 300: Nyasha Maforo, Vahid Ghodrati, Zhaohuan Zhang, Andres Saucedo, Ajin Joy, Manuj Sharma, Yongkai Liu, Da Wang, Chang Gao, Ran Yan, Kai Zhao, Alex Hung, Kaifeng Peng, Zixuan Zhao, Guowen Shao, Sanjib Gurung, Mostafa Mahmoudi, Harry, Caroline Colbert, Xinran Zhong, Le Zhang, Felix, and Ziwu.

I would like to thank Dr. Mark Bydder who joined MRRL at the end of my second year of my PhD. He took me under his wing and taught me so much and always made himself available. His way of communicating difficult concepts motivated me. He always encouraged me to dig deeper and was there to discuss the difficult problems I was facing in many instances of this

journey. His support was crucial and key to my growth as a scientist. Him and I went to the machines together many times and ran experiments, showed me how to code stuff on IDEA, and many times sat with me to look at reconstruction code that I was implementing. When I was stuck, he would often tell me his approaches in the past. This hands on approach contributed to my deep understanding of MRI. I cannot say enough to show my gratitude to him.

Without my parents, I would not have been born. With their unconditional love and support, they always made sure I had every opportunity to achieve my goals, and always made sure that I was healthy. I always look to them for motivation, encouragement, and emotional support. I will always be fond of how they took care of me, and my two siblings, Aziz and Yasmin. I thank Aziz and Yasmin for all of the fun times they provided.

I will always be thankful for meeting Janet Hu, my girlfriend. She came into my life during the thick of my PhD and always gave me motivation, love, and support.

I dedicate this thesis to my mom, dad, Aziz, Yasmin, and Janet.

# VITA

2016–Present Graduate Student Research, Physics and Biology in Medicine, The University of California, Los Angeles, California.

2012–2016 Bachelor of Science with honors, Physics; Minors in Mathematics and Biomedical Engineering. The Pennsylvania State University, University Park, PA. GPA 3.7/4.0

# PUBLICATIONS

Ali F, Bydder M, *et al. Slice encoding for the reduction of outflow signal artifacts in cine balanced SSFP imaging. Magnetic Resonance in Medicine*, 2021; 86:2034-2048.

Pantoja JL, Ali F, *et al. Arterial spin labeling magnetic resonance imaging quantifies tissue perfusion around foot ulcers. Journal of Vascular Surgery Cases, Innovations, and Techniques*, 2022; 8:817-823. **co-first author**.

Ali F, *et al. Unfolding Coil Localized Errors from an imperfect slice profile using a Structured Autocalibration Matrix: An application to reduce outflow effects in cine bSSFP imaging.* **In review for publication at** *NMR in Biomedicine.*

Wang D, Chien A, Shao J, Ali F, and Hu P. *Accelerated phase contrast MRI using hybrid one-and two-sided flow encodings only (HOTFEO). NMR in Biomedicine.*, 2018; 31:e3904.

Bydder M, Yang Y, Gay Y, Ali F, Steinberg M, Low D, Hu P. *PDFF Quantification for the*

*Assessment of Red Bone Marrow During RT. Medical Physics.*, 2019; 6:e331.

Kaneko N, Ullman H, Ali F, *et al. In vitro modeling of human brain arteriovenous malformation for endovascular simulation and flow analysis. World Neurosurgery.*, 2020; 141:e873-e879.

Ghodrati V, Bydder M, Ali F, *et al. Retrospective respiratory motion correction in cardiac cine MRI reconstruction using adversarial autoencoder and unsupervised learning. NMR in Biomedicine.*, 2020; 34:e4433.

Bydder M, Ali F, Ghodrati V, *et al. Minimizing echo and repetition times in magnetic resonance imaging using a double half-echo k-space acquisition and low-rank reconstruction. NMR in Biomedicine.*, 2020; 34:e4458.

Bydder M, Ali F, Saucedo A, *et al. A study of 3D radial density adapted trajectories for sodium imaging. Magnetic Resonance Imaging.*, 2021; 83:89-95.

Ghodrati V, *et al. Automatic segmentation of peripheral arteries and veins in ferumoxytol-enhanced MR angiography. Magnetic Resonance in Medicine.*, 2022; 87:984-998.

Bydder M, Ali F, Saucedo A, *et al. Low rank off-resonance correction for double half-echo k-space acquisitions. Magnetic Resonance Imaging.*, 2022; 94:43-47.

2D/3D — two/three dimensional

ASL — Arterial Spin Labeling

bSSFP — balanced steady-state free precession

B0 Field — Magnetic Field of the bore

B1 Field — radiofrequency field on the plane transverse to the axis of the bore

CASL — continuous ASL

CNR — Contrast to noise ratio

DFT — discrete Fourier transform

ECG — electrocardiogram

EPI — echo-planar imaging

FFT — fast Fourier Transform

FID — frequency induction decay

FLASH — fast low angle shot imaging

FOV — field of view

FT — Fourier Transform

FWHM — full-width at half-maximum

$G_pe$ — phase encoding gradient

$G_ro$ — readout gradient

$G_se$ — slice-encoding gradient

GRAPPA — generalized autocalibrated partially parallel acquisition

GRE — gradient recalled echo

HASTE — half-Fourir acquired single-shot turbo-spin echo

IFFT — inverse Fourier transform

INSiL — instantaneous signal loss imulation algorithm

mm — millimeter

MOLLI — modified Look-Locker inversion recovery

MR — magnetic resonance

MRI — magnetic resonance imaging

MRRL — Magnetic Resonance Research Labs

ms — millisecond

OOS — out-of-slice

ppm — parts-per-million

PCA — principal component analysis

PCASL — pseudo-continuous ASL

PASL — pulsed ASL

RF — radio-frequency

RMS — RMS

ROI — region of interest

s — second

SD — standard deviation

SE — slice-encoding

SENSE — sensitivity encoding

SNR — signal to noise

SOS — sum of squares

T — Tesla

T1w, T2w — T1, T2 weighted

TE — echo time

TMS — Tetramethylsilane

TR — repetition time

TI — inversion time

TSE — turbo spin echo

UCLA — The University of California, Los Angeles

UNCLE SAM — unfolding coil localized errors using a structured autocalibration matrix

# CHAPTER 1

# Introduction

## 1.1 Motivation and Specific Aims

Magnetic Resonance Imaging (MRI) provides the highest soft-tissue contrast among the existing imaging modalities. Signal contrast in MRI is a cumulative function of the radiofrequency (RF) excitation profile, how one manipulates magnetic field gradients during the acquisition process, and the spacing of the RF pulses. This multi-parametric dependency makes MRI a versatile choice for diagnostic imaging.

Another notable feature of the MR signal is its inherent sensitivity to flowing spins. The most common approach to spatial encoding in MRI makes the precessional frequency a linear function of position, implemented practically by magnetic field gradients imposed along the direction of interest. During excitation, if the imaging slice intersects or includes vessels, the flowing spins may be exposed to a different history of RF pulses than the target (stationary) spins in the slice, providing a basis for signal contrast between the stationary and flowing spins.

Blood flow in the body (both large and small vessels as well as intracardiac cavities) can be exploited to provide image contrast or need to be mitigated to improve image quality. One such difference in signal contrast is exploited for quantifying tissue perfusion in a family of techniques called Arterial Spin Labeling (ASL) [126, 127, 29]. With ASL, spins in vessels upstream of a slice of interest are excited and they carry their magnetization status with

them as they flow into the capillary bed of the tissue of interest. The slice is imaged with and without the upstream excitation and a subtraction leaves only the signal from spins that have entered the slice from upstream. This family of methods is now mature for brain imaging. The work detailed in the first specific aim applies a specific form of the technique to assess for peri-wound perfusion in diabetic subjects with foot ulcers.

The evaluation carried out for the first specific aim exemplifies how one can exploit the effect of inflowing spins. It is inevitable that flow effects manifest in cardiac imaging. The workhorse sequence used in cardiac imaging [24, 35, 89, 1] is balanced steady-state free precession (bSSFP)[84]. The "balanced" term refers to zero net gradient induced intravoxel dephasing by the end of a repetition between adjacent RF excitation pulses. In addition, the RF pulses for bSSFP follow a linear $\pi$ rad/TR phase ramp which refocuses most spins mid-TR [97]. Both of these features preserve spin signal history. These two physical mechanisms in bSSFP imaging results in $\pi$ rad/TR stationary spins to have no signal intensity in steady-state, resulting the commonly seen banding artifacts [96]. For outflowing spins, as Markl et al [72, 73] showed, the RF phase-cycling in bSSFP imaging makes outflowing spins with $\pi$ rad/TR add coherently, resulting in a signal pileup that projects onto the target plane being imaged. These spin outflow issues are problematic in any imaging slice that is adjacent to pulsatile structures and severe outflow artifacts can render the image non-diagnostic. The frequency dependence in bSSFP imaging makes these artifacts a larger concern in higher fields, 3 Tesla and above, where field inhomogeneity becomes more pronounced.

The motivations behind specific aims 2 and 3 is to develop methods to mitigate artifacts from outflowing spins in bSSFP imaging. The first of these is a proof-of-concept, showing that explicitly spatially encoding these outflowing spins using through-slice phase-encoding ("slice-encoding", "SE") can unfold them from the target slice, providing a cleaner image at the expense of increased scan time [3]. The work presented in specific aim 3 uses localized coil channel sensitivity to unalias outflowing spins from the target slice.

## 1.2 Thesis Outline

Chapter 2 provides a brief introduction in MRI. It provides the background necessary to comprehend the methods carried out in the specific aims and includes spatial encoding, ASL techniques, and 2D bSSFP imaging. The spatial encoding discussion will narrate a Bloch simulation of frequency and phase-encoding, from which a conceptual basis of parallel imaging techniques can be described.

Chapter 3 goes over our feasibility study where an arterial spin labeling technique was used to visualize peri-wound foot perfusion of subjects with diabetic foot ulcers [85]. The discussion of this work begins with the clinical relevance and the standard methods to assess perfusion, emphasizing why a non-invasive MRI technique would be beneficial for diabetic foot ulcer subjects. We then review the methods of obtaining the perfusion-weighted information, followed by a discussion of the results obtained and their clinical implications.

The work described in chapter 4 formulates through-plane flow effects in 2D bSSFP imaging as a volumetric imaging problem, treating outflow artifacts a s aliased signal projected onto the imaged 2D plane. This method explicitly spatially encodes spins outflowing from a 2 D excitation profile by implementing s lice-encoding gradient lobes [3]. The unaliased slice can be reconstructed separately from the outflowing spins after a volumetric Fourier transform. The cost is a substantial increase in scan time scaled by the number of slice-encoding steps.

In chapter 5, we address how to achieve the goals outlined in chapter 4 in a more practicable way, by implementing a method that UNfolds Coil Localized Errors of a distorted slice profile using a Structured Autocalibration Matrix. This method, abbreviated as UNCLE SAM, captured coil-localization of the outflowing s pins in a calibration subspace to unfold their effects from the target slice.

In chapter 6, I summarize the contributions to my work to flow effects in MRI.

# CHAPTER 2

# Fundamentals of MRI

I will detail the topics that I found core to my understanding of MRI. All illustrations of the concepts discussed in this thesis (such as Bloch simulations or reconstruction) were implemented by me and can be found in my GitHub page `https://github.com/faa5115`.

The core of MRI rests in the principles of "nuclear induction" [11, 12]. Nuclear induction results in the precession of magnetic moments around a static magnetic field after being perturbed by an applied radio-frequency pulse. The observed behavior is a bulk effect due to the superposition of a large number of hydrogen nuclei within a macroscopic sample, which we will refer to as "spin ensembles." Because the quantum-mechanical expectation value in the macroscopic scale exactly follows the classical equations of motion, the underlying work will only consider a classical description.

By default, we will consider processes in the rotating frame of reference. While describing these processes, it's important to distinguish between the axes of the ***magnet*** and the ***image***. While these are both Cartesian in 3-space, with orthonormal bases, the magnet coordinates are fixed, whereas the image coordinates are in general rotated and displaced relative to the magnet coordinates (depending on the orientation and position of the image element). I will use $\vec{r}$ to denote the position vector whose tip is at coordinates $< u_x, u_y, u_z >$ and whose tail is at the isocenter of the magnet with coordinates $< 0, 0, 0 >$.

As we will see in this chapter, matrices are a convenient tool when describing the behavior

of the magnetization in nuclear magnetic resonance. Rotation matrices are commonly used in describing the rotation behavior of a spin ensemble. In this writeup, $R_{\vec{v}}(\theta)$ to describe the counterclockwise (positive) rotation of angle $\theta$ around an axis that points along of vector $\vec{v}$. Rotation matrices around the directions $u_x$, $u_y$, and $u_z$ are:

$$
\begin{aligned}
R_{\hat{u}_x}(\theta) &= \begin{bmatrix} 1 & 0 & 0 \\ 0 & cos(\theta) & -sin(\theta) \\ 0 & sin(\theta) & cos(\theta) \end{bmatrix} \\
R_{\hat{u}_y}(\theta) &= \begin{bmatrix} cos(\theta) & 0 & sin(\theta) \\ 0 & 1 & 0 \\ -sin(\theta) & 0 & cos(\theta) \end{bmatrix} \\
R_{\hat{u}_z}(\theta) &= \begin{bmatrix} cos(\theta) & -sin(\theta) & 0 \\ sin(\theta) & cos(\theta) & 0 \\ 0 & 0 & 1 \end{bmatrix}
\end{aligned}
\tag{2.1}
$$

## 2.1 Introduction of the Fourier Transform

In order to understand the concept of spatial localization in MRI, it is important to be familiar with the Fourier transform. Most commonly, the Fourier transform is introduced by considering a one-dimensional time signal and its representation in the temporal frequency domain. A fundamental postulate of Fourier theory is that any periodic time signal can be represented as a sum of sinusoids, of appropriate amplitude and phase. The term "sinusoid" is equally applicable to a cosine or sine function, because one is simply a phase shifted version of the other, where the phase shift is $\frac{\pi}{2}$. A general sinusoid can be considered as a linear combination of a sine and cosine function at the same frequency, $g_{cos}[n]cos(n\omega_0 t) + g_{sin}[n]sin(n\omega_0 t)$. This linear combination results in what is known as a ***phasor***. This phasor can be thought of as a vector rotating around the circumference of a circle at the frequency of

the composite sinusoids and with a starting phase, $\phi[n]$ determined by the relative amplitude of the sine and cosine coefficients, $g_{sin}(n)$ and $g_{cos}[n]$ according to $\phi[n] = arctan(\frac{g_{sin}[n]}{g_{cos}[n]})$. By adding together all of the constituent phasors in a time signal Fourier tells us that we can create any arbitrary periodic time signal. An alternative, and intuitive, way to represent the combination of cosine and sine functions is to consider the motion along the circumference of the unit circle. In this case, cosine function represents the projection along the horizontal direction and the sine functions represents the direction on the vertical axis. These are clearly 90° out of phase, but their sum represents the position of a point on the circumference of the circle at any time $t$. This point can also be represented by a two dimensional vector, whose coordinates are $< cos(n\omega_0 t), sin(n\omega_0 t) >$. It is common practice to represent the cosine and sine components of the unit circular motion in the two dimensional ***complex plane*** where the horizontal axis is the "*real*" axis of the complex plane and the vertical axis is the "*imaginary*" axis of the complex plane. In this notation, motion around the unit circle is represented by $cos(n\omega_0 t) + i \cdot sin(n\omega_0 t)$. In what is widely regarded as the most beautiful equation in mathematics, Euler derived a compact representation of the complex motion around the unit circle by pointing out that $cos(n\omega_0 t) + sin(n\omega_0 t)$ is equal to $e^{in\omega_0 t}$. The proof of Euler's equation above can be seen by considering the infinite Taylor series expansion for the sine, cosine, and exponential functions. As mentioned above, any periodic time signal can be expressed as the sum of its sinusoidal components. This is summarized mathematically in the Fourier synthesis equation, which is as follows:

$$\begin{aligned} f(t) &= \sum_{n=-\infty}^{\infty} [g_{cos}[n]cos(n\omega_0 t) + g_{sin}[n] \cdot sin(n\omega_0 t)] \\ &= \sum_{n=-\infty}^{\infty} [c[n]e^{-in\omega_0 t}] \end{aligned} \tag{2.2}$$

Because the left and right hand sides of equation 2.2 represent the same signal, the signal can be expressed unambiguously as either a function of time or a function of frequency where the transform between these two domains is described in equation 2.2. Note that so far, our assumption is that the time signal is periodic. In practice, this is rarely the case for

physical signals so we need a generalization for this relationship for non-periodic signals. In practice this is done by considering the period of the signal as being extended progressively, such that in the limit as the period approaches infinity, then the signal is no longer periodic. This limiting process leads to the definition of the continuous Fourier transform, where the summation in equation 2.2 becomes an integral and the discrete $n\omega_0$ becomes continuous $\omega$. This process is summarized in:

$$F(\omega) = \int f(t)e^{-i\omega t}dt \tag{2.3}$$

Implicit in the definition of the Fourier transform, the function is continuous. However, when the signal is sampled in real life, the *discrete* sampling process unavoidably generates a periodic representation of the non-periodic signal. This in effect produces periodic copies of the signal, separated by a distance determined by the sampling frequency. We will discuss this in more detail later in this chapter. A diagram illustrating these concepts is illustrated in Figure 2.1.

We now consider the physical processes whereby a detectable MRI signal is generated and manipulated. The fundamental interactions relating magnetic fields and radio waves in this context are summarized in a set of equations called the Bloch equations, named after professor Felix Bloch.

## 2.2 The Bloch Equation

Felix Bloch [11, 12] and Edward Purcell [91] independently developed the modern concepts of magnetic resonance. Any magnetization (the sum of magnetic dipole moments, such as the sum of multiple hydrogen nuclei), $\vec{M}$ experiences a torque when exposed to a magnetic field $\vec{B}$ that is described as follows:

$$\frac{d\vec{M}}{dt} = \gamma \cdot \vec{M} \times \vec{B} + \frac{M_0 - M_{u_z}}{T_1} + \frac{M_\perp}{T_2} \tag{2.4}$$

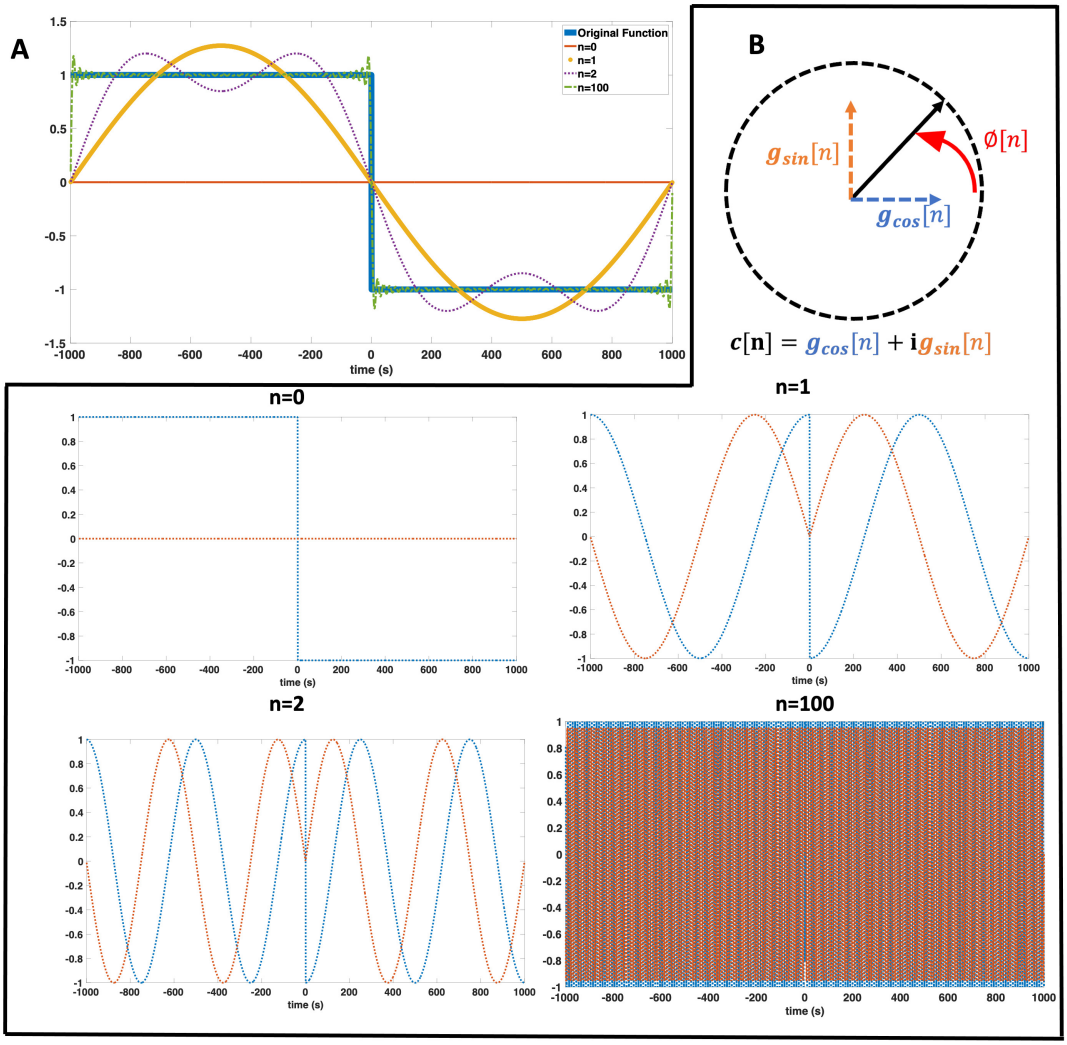


*Figure 2.1: A: An example function centered at time 0, with negative time coordinates being* $1$ *and positive coordinates being* $-1$ *in addition to* $n$*-sum Fourier series estimates for* $n = 0$*,* $n = 1$*, and* $n = 100$*. B: On top we have a graphical illustration of a complex number.* $g_{sin}(n)$ *and* $g_{cos}(n)$*, which are shown in equation 2.2, are the sine and cosine weights of the* $n^{th}$ *term in the Fourier series, respectively. They are both shown in equation 2.2. The remaining four plots are individual sinusoidal terms used to estimate the example function in its Fourier series expansion. The "vector sum" of each of the sinusoidal terms provides the Fourier coefficient of sinusoid* $n$ *of the example function.*

where $M_0$, $M_{u_z}$, and $M_\perp$ are the equilibrium, longitudinal, and transverse magnetization respectively. "Longitudinal" refers to the direction along the primary external magnetic field. $\gamma$ is specific to nuclei. It is the Gyromagnetic ratio, which is a relationship constant between a magnetization and the angular momentum of a nucleus. It is $42.57 \cdot 10^6$ Hz/T for hydrogen nuclei. $T_1$, and $T_2$ are constants that are specific to materials and tissues and are recovery and relaxation terms that are specific to the local environments of a magnetization. Respectively, they are exponential terms describing longitudinal recovery and transverse relaxation.

Intuitively, equation 2.4 tells us that the magnetization will rotate around the magnetic field it perceives in a given reference frame at a frequency $\gamma \cdot |\vec{B}|$, while simultaneously having its longitudinal component recover to its equilibrium and its transverse component decay. The cross product term can be described by a rotation matrix during a time $\Delta t$ as $R_{\vec{B}}(-2\pi\gamma|\vec{B}|\Delta t)$. The second two terms of equation 2.4 are exponential, describing changes in the magnitude of the magnetization over time. Over a time $\Delta t$ the transverse decay (or "relaxation") is described as $M_\perp(t+\Delta t) = M_\perp(t)e^{-\Delta t/T_2}$ and the recovery of the longitudinal magnetization can be described as $M_{u_z}(t+\Delta t) = M_0 \cdot (1 - e^{-\Delta t/T_1}) + M_{u_z}(t)e^{-\Delta t/T_1}$. These two terms can be described in a matrix format as

$$
\begin{aligned}
\begin{bmatrix} M_{u_x}(t+\Delta t) \\ M_{u_y}(t+\Delta t) \\ M_{u_z}(t+\Delta t) \end{bmatrix} &= \begin{bmatrix} M_{u_x}(t)e^{-\Delta t/T_2} & 0 & 0 \\ 0 & M_{u_y}(t)e^{-\Delta t/T_2} & 0 \\ 0 & 0 & M_{u_z}(t)e^{-\Delta t/T1} + M_0 \cdot (1 - e^{-\Delta t/T_1}) \end{bmatrix} \\
&= \begin{bmatrix} e^{-\Delta t/T_2} & 0 & 0 \\ 0 & e^{-\Delta t/T_2} & 0 \\ 0 & 0 & e^{-\Delta t/T1} \end{bmatrix} \begin{bmatrix} M_{u_x}(t) \\ M_{u_y}(t) \\ M_{u_z}(t) \end{bmatrix} + M_0 \begin{bmatrix} 0 \\ 0 \\ (1 - e^{-\Delta t/T_1}) \end{bmatrix} \\
\vec{M}(t+\Delta t) &= \mathrm{A}_R(\Delta t, T_2, T_1)\vec{M}(t) + M_0 \mathrm{B}_D(\Delta t, T_1)
\end{aligned}
\tag{2.5}
$$

where $\mathrm{A}_R(\Delta t, T_2, T_1)$ and $\mathrm{B}_D(\Delta t, T_1)$ are used as a to describe the T2 decay and T1 recovery.

Incorporating all effects will therefore describe the magnetization precession over a time $\Delta t$ as $\vec{M}(t+\Delta t) = R_{\vec{B}}(-2\pi\gamma|\vec{B}|\Delta t)\mathrm{A}_R(\Delta t, T_2, T_1)\vec{M}(t) + M_0\mathrm{B}_D(\Delta t, T_1)$.

MRI deals with hydrogen nuclei primarily coming from water and fat molecules that are exposed to the strong static field of the bore $\vec{B_0}$ that points along its axis, $\hat{u}_z$. The behavior described in equation 2.4, conveys that the nuclei exposure to this field polarizes most of the spins along the bore's axis. The signal in an MR image is a result of manipulating the net magnetic moment such that a component lies in the transverse plane. Any temporary perturbation to this magnetic field could cause the magnetization to be "excited" or "tip" from the longitudinal axis, resulting in a transverse component. This will cause the transverse component of the magnetization to precess around the static field of the bore, $\hat{u}_z$ at frequency $\gamma B_0$, which is referred to as the "Larmor frequency." The magnetization will simultaneously exhibiting relaxation and recovery characterized by the rate constants 1/T2 and 1/T1 respectively.

## 2.3 Resonance Frequency

The local field felt by a spin ensemble determines its resonant frequency according to $\gamma \cdot |\vec{B}|$, where $\vec{B}$ is the vector sum of $\vec{B_0}$ and local off-resonance effects. These local off-resonance effects include imperfections in how the scanner system preserves field homogeneity, susceptibility induced off-resonant effects, and chemical shifts. These sources of off-resonance are present once the subject enters the bore. In addition to these, applied magnetic field gradients also induce off-resonance, which can be turned on or off with time-varying amplitudes. I will use $\Delta B_0(\vec{r})$ to refer to the spatially varying, cumulative B-field inhomogeneity of the first three sources mentioned, and use $\Delta B(\vec{r})$ to refer to the cumulative B-field effect of all four sources. By definition, spin ensembles with $\Delta B_0 = 0$ are referred to as "on resonant."

### 2.3.1 Hardware Imperfections

Once a magnet is assembled in a hospital or research center, its field uniformity is impacted by the presence of nearby equipment along with imperfections in its own assembly. The process of countering these imperfections is called "shimming" which stems from the name of the hardware used: a wedge shaped sheet metal being fixed at various locations of the bore to preserve field uniformity [5, 94] . This has been referred to *passive shimming*. *Active shimming* refers to the use of currents to generate additional fields to compensate for the inhomogeneity.

### 2.3.2 Magnetic Susceptibility

Every subject will be magnetized when exposed to to an external magnetic field. Magnetic susceptibility is a measure of how much the object magnetized. **Paramagnetic** objects polarize in the direction of the external field, while **diamagnetic** objects polarize opposite to the field. These two classes of magnetization refer to objects only when they are exposed to an external field. **Ferromagnetic** objects polarize along the direction of the external field and *maintain* their magnetization when no longer exposed. Different tissues and regions within the tissue magnetize differently, and therefore contribute to the local field inhomogeneity [98].

### 2.3.3 Chemical Shift

Chemical shift refers to the local field a hydrogen nucleus is exposed to as a result of its molecular chemical environment. Because it is a phenomenon in the localized molecular level, hydrogen nuclei in the same molecule may have different chemical shifts. These local environments are called *functional groups*. The chemical shift of a functional group is described in a relative sense as:

$$\delta = \frac{[f_{sample} - f_{ref}][Hz]}{f_{ref}[MHz]} \tag{2.6}$$

where $f_{sample}$ and $f_{ref}$ are the resonant frequencies of the hydrogen nucleus residing in the functional group of interest and reference functional group, respectively. The units of the difference in the numerator is in Hz and the unit for the denominator is MHz, giving chemical shift the unit "parts-per-million", or ppm. This is a convenient metric because it is invariant to field strength. The imaging community uses $\gamma|\vec{B}_0|$ as the reference.

### 2.3.4 Magnetic Field Gradients

Spatially linear magnetic field gradients provide another source of off-resonance. Unlike the previous sources, these are deliberately imposed onto the imaged subject. Unlike the previous sources, these are induced onto the imaged subject. The off-resonance applied by gradients only are described as

$$\Delta\vec{B}(\vec{r}) = \vec{G} \cdot \vec{r} \tag{2.7}$$

where $G_x(t) = \frac{dB_z(\vec{r},t)}{dx}$, $G_y(t) = \frac{dB_z(\vec{r},t)}{dy}$, and $G_z(t) = \frac{dB_z(\vec{r},t)}{dz}$ Time-varying magnetic field gradients are used to guide spatial encoding in the image acquisition, which we will discuss later. These gradients will be described in the context of the orthogonal axes of an image.

In MR imaging, these off-resonance effects can be characterized as rotations around the axis of the bore, $R_{\hat{u}_z}(\theta)$ for $\theta = \gamma\Delta B(\vec{r},t)t$. For a single ensemble located at $\vec{r}$ at some reference time $t = 0$, the transverse magnetization of the ensemble will behave as:

$$\vec{M}_\perp(\vec{r},t) = \vec{M}_\perp(\vec{r},t) \cdot e^{\frac{-t}{T_2(\vec{r})}} \cdot e^{i\gamma\Delta B(\vec{r},t)t} \tag{2.8}$$

It must be noted, and will be discussed in the next section, that signal reception is the vector sum of all spins. Therefore, the transverse signal is the integral sum of over all space:

$$\int \vec{M}_\perp(\vec{r},t)d\vec{r} = \int \vec{M}_\perp(\vec{r},t) \cdot e^{\frac{-t}{T_2(\vec{r})}} \cdot e^{i\gamma\Delta B(\vec{r},t)t}d\vec{r} \tag{2.9}$$

## 2.4 Rotating Reference Frame

It is easier to interpret magnetic resonance behavior in the reference frame of Larmor frequency, the "rotating frame." As distinct from the laboratory frame, the rotating frame is at rest relative to spins rotating at the Larmor frequency. The Larmor frequency is defined as the central frequency at a given field strength as $\gamma B_0$. Figure 2.2 illustrates this for three spin ensembles with the following resonant frequencies — -3.5, 0, and 3.5 ppm — displayed for 0.1T (a low field was used to easily illustrate the advantage of interpreting in the Larmor frame). The top half of the figure shows the transverse precession in the stationary frame while the bottom show their precession in the rotating frame. Both abide by the Bloch equation, 2.4, because it considers the magnetic field perceived in the particular frame of reference. The stationary reference frame perceives $\vec{B}_{perceived} = \vec{B}_0 + \Delta\vec{B}_0$ for each spin ensemble. Because $\vec{B}_0 >> \Delta\vec{B}_0$, it is difficult notice off-resonance. For this reason it is easier to interpret the MR signal in the rotating reference frame, which only perceives magnetic field causing off-resonant effects. Throughout this thesis, I will be referring to the Larmor rotating frame, unless mentioned otherwise.

## 2.5 Spatial Encoding

Magnetic field gradients are pivotal for spatial localization. The first image from gradient encoding was carried out by Lauterbur [62] and independently by Mansfield [71]. Gradients impose a spatial distribution of frequencies that can be used to encode the spins along the axis of the gradient. Unless otherwise mentioned, our discussion on spatial encoding will only feature gradient-induced off- resonance. That is $\Delta B_0 = 0$. This section will discuss the mechanisms of using gradients for spatial encoding.

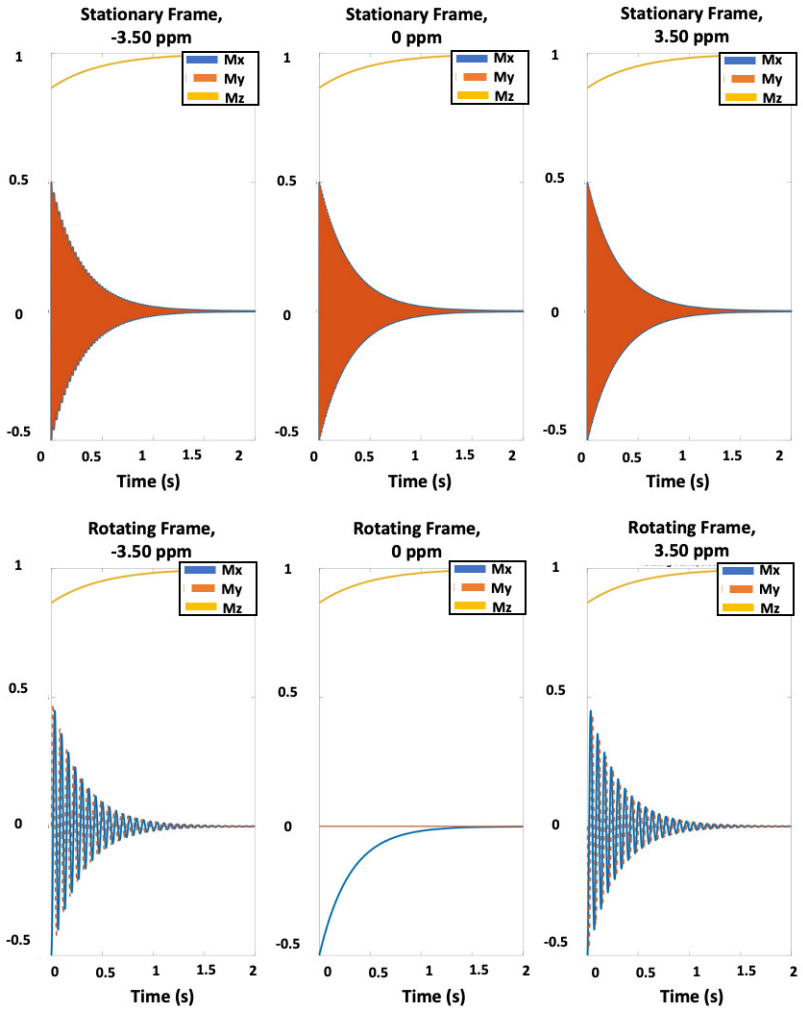


*Figure 2.2: An illustration using Bloch simulation results to illustrate the convenience of visualizing in the rotating (bottom) frame instead of the stationary (top, for 0.1 T) frame. These results describe the time-varying magnetization on spin ensembles with T2/T1 = 300/500 ms the following relative off-resonances: -3.5, 0, and 3.5 ppm. Despite only having a difference of $\pm 15Hz$, it is difficult to even distinguish the three ppm in the top plots because they have not been demodulated by the Larmor frequency, $\gamma|\vec{B}_0|$, unlike in the bottom three plots.*

### 2.5.1 Slice Selection

#### 2.5.1.1 $B_1$ Excitation

Slice selection refers to exciting the spins in the physical region to be imaged [36]. A radio frequency (RF) field is applied in the transverse plane that tips the bulk magnetization away from the bore's axis, providing a transverse magnetization component that can induce an electromotive force in the receiver coil and therefore a detectable signal. We will first discuss excitation for a single ensemble only being exposed to a time-varying $B_1$ field. Such an excitation process can be visualized in Figure 2.3. In the **rotating frame** this spin-ensemble only perceives a (time-varying) $B_1$ component as the total magnetic field, $\vec{B}_{perceived} = \vec{B}_1(t)$. According to 2.4, during each infinitesimal time, $dt$,the magnetization will rotate around the $\vec{B}_1(t)$ by frequency $\gamma \cdot |\vec{B}_1(t)|$. In this setting the fact that $\vec{B}_1(t)$ lies in the transverse plane will rotate the longitudinal magnetization into the transverse plane such that its projection into the transverse plane will be orthogonal to $\vec{B}_1(t)$. The rotation of the longitudinal magnetization around the axis of the $B_1$ field will continue for as long as the $B_1$ field persists. If relaxation and recovery effects are ignored during the excitation process, then the flip angle, $\alpha$, represents the cumulative rotation of the magnetization caused by the $B_1$ field and is expressed as:

$$\alpha = \gamma \cdot \int_0^{T_{RF}} |\vec{B}_1(t)| dt \tag{2.10}$$

#### 2.5.1.2 Slice Selective Excitation

In the presence of off-resonance, an observer in the rotating frame would now perceive a total magnetic field given by

$$\vec{B}_{perceived} = \vec{B}_1(t) + \Delta\vec{B}(\vec{r}, t) \tag{2.11}$$

where $\Delta\vec{B}(\vec{r}, t) = |\Delta\vec{B}(\vec{r}, t)|\hat{u}_z$. Spins with $\gamma|\Delta\vec{B}(\vec{r}, t)| >> \gamma|\vec{B}_1(t)|$ will primarily rotate around $\hat{u}_z$, and therefore have little (if any) tip. Conversely, spins with $\gamma|\vec{B}(\vec{r}, t)| << \gamma|\vec{B}_1(t)|$

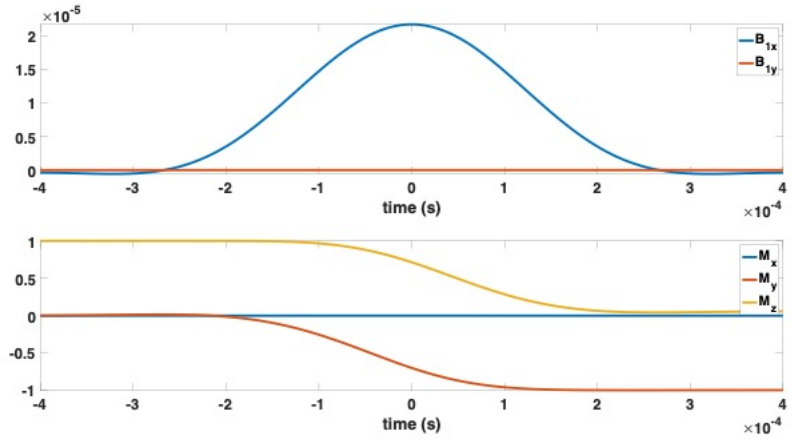


*Figure 2.3: A Bloch (along $\hat{u}_z$) simulation of a time-varying $B_1$ envelope function (top) being applied to a magnetization vector that is initially in thermal equilibrium. The bottom plot shows the behavior of the magnetizations' components as the $B_1$ tips the magnetization onto the transverse plane.*

will be tipped into the transverse plane. This means that the $B_1(t)$ field has a frequency dependent signal response, which is core to selecting the imaged slice (for 2D applications) or slab (for 3D applications). In the absence of other off-resonance contributions ($\Delta B_0 = 0$), externally applied controlled gradients can be used to impose off-resonance conditions in a linear, direction-dependent fashion. Denoting this arbitrary direction by $\hat{u}_s$, a linear spread of frequencies along $\hat{u}_s$ is imposed according to

$$f_s = \gamma \vec{G}_s \cdot \vec{r} \tag{2.12}$$

where $\vec{G}_s$ is the gradient pointing along $\hat{u}_s$. Earlier we noted that an arbitrary position vector has its tail at coordinate $< 0, 0, 0 >$. Therefore, at isocenter the magnitude of $\vec{r}$ is 0, such that 2.12 evaluates to zero. This means that there is no frequency offset at isocenter, and in the presence of a linear gradient, the spins at isocenter are on-resonance. This is illustrated by Bloch simulation in Figure 2.4 for two cases in the rotating frame: where the $\vec{B}_1(t)$ doesn't change direction (selecting a slice at isocenter) and where the direction of $\vec{B}_1(t)$ changes linearly over time to target a slice off isocenter. This Bloch simulation illustrates the Fourier shift property described in Pauly's k-space interpretation of the RF excitation

[88]: where a linear time-dependent phase in $B_1$ results in a spatial shift in the excited slice.

By the end of RF excitation, a phase dispersion across the width of the slice occurs according to

$$\phi_{0,slice} = 2\pi\gamma \int_{T_{peak,RF}}^{T_{RF}} \vec{G}_s(t) \cdot \vec{r} dt \tag{2.13}$$

where $T_{peak,RF}$ is the time the peak $B_1(t)$ of the RF pulse is delivered. Figure 2.5, illustrates the complex (vector) transverse magnetization profile along the slice direction from the sinc pulse previously shown in Figure 2.4. Because the MR signal is a vector sum of all spins, refocusing gradient must be applied in order to minimize signal loss. The resulting profile after a gradient refocusing lobe is shown in the bottom plots of Figures 2.5A and 2.5B. Imaging can start after slice refocusing.

#### 2.5.1.3 Repetition

As we will see later in this chapter, multiple excitation pulses are required as the signal is acquired to generate an image. The time in between adjacent excitation pulses is called the "*repetition time*" and is often denoted as TR.

#### 2.5.1.4 Transverse Magnetization after Excitation Pulse

If generalized to any B-field inhomogeneity term, $\Delta B$, the transverse magnetization behavior at at time $t$ from the peak RF can be expressed as:

$$\vec{M}_{\perp}(\vec{r}, t) = \vec{M}_{\perp,0}(\vec{r}) \cdot e^{-\frac{t}{T_2}} \cdot e^{-i2\pi\gamma\Delta B(\vec{r},t)} \tag{2.14}$$

where $\vec{M}_{\perp,0}(\vec{r})$ is the transverse magnetization immediately after excitation. The imaginary exponential term captures the transverse magnetization rotating around the perceived magnetic field in the rotating frame, $\Delta B(\vec{r}, t)\hat{z}$, as according to 2.4:

$$\phi(\vec{r}, t) = e^{-i2\pi\gamma\Delta B(\vec{r},t)} \tag{2.15}$$

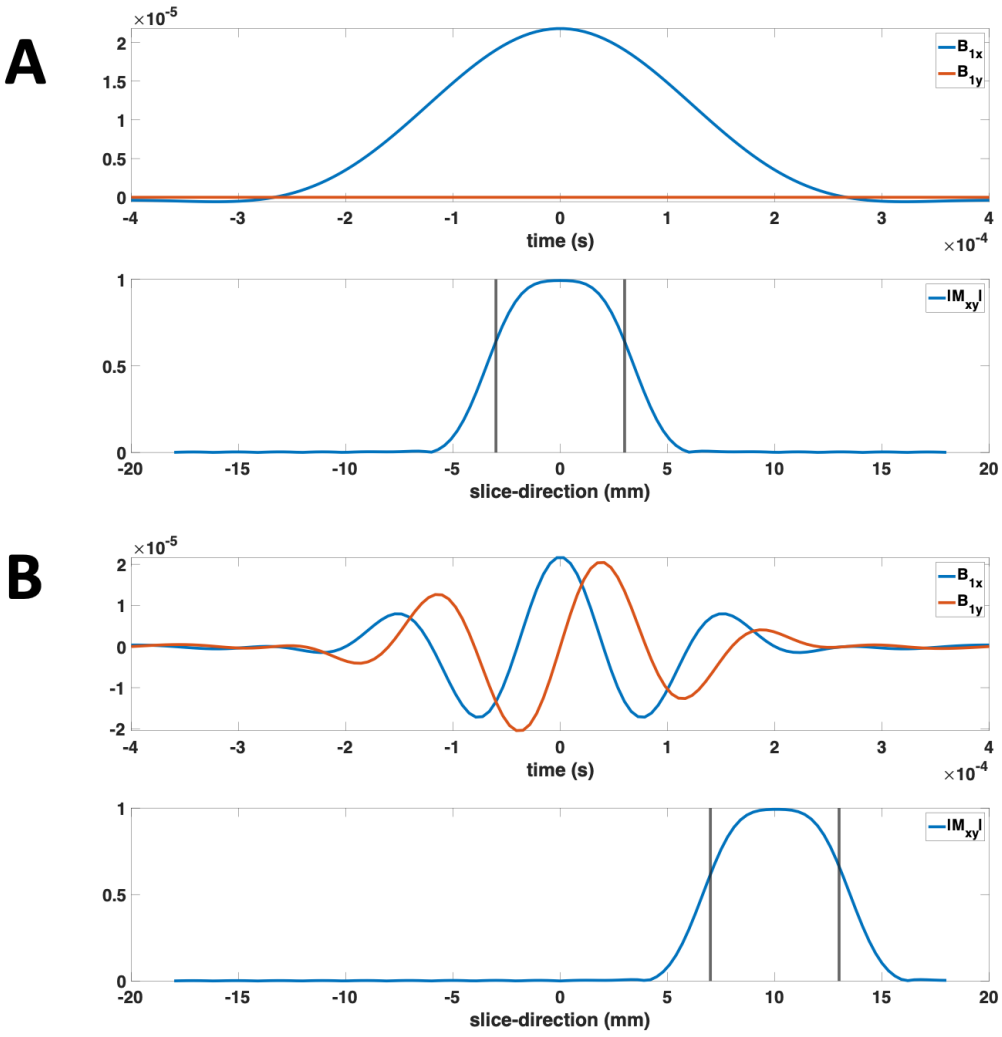


*Figure 2.4: Bloch simulation of a time-varying $B_1$ envelope function with a $90°$ flipangle. In (A) $\vec{B}_1(t) = B_1(t)\hat{u}_x$ leading to the excitation profile being along the isocenter, whereas in (B) there $\vec{B}_1$ has a time-varying phase, which in this case resonates with spins 10mm away from isocenter.*

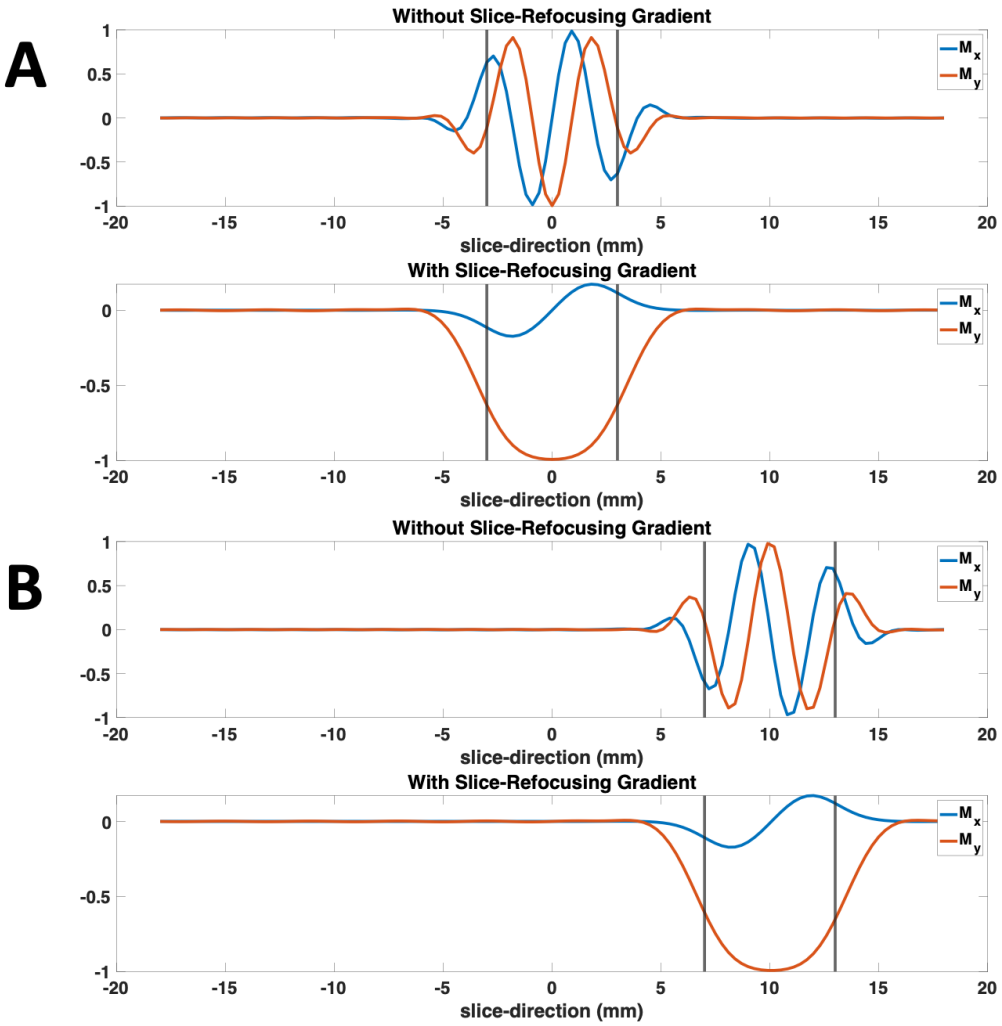


*Figure 2.5: Transverse magnetization profiles from the same Bloch simulations shown in Figure 2.4, respectively, with (A) showing the excitation at isocenter and (B) showing the excitation 10mm off isocenter. For both, the top shows the transverse profile immediately before gradient refocusing and the bottom shows immediately after gradient refocusing.*

### 2.5.2 MR Readout

Transverse spins induce signal in the receivers by Faraday's law of induction. The signal readout during this measurement is time-varying and each timepoint consists of the vector sum of all transverse spins. If the maximum off-resonance present in the pool of excited spins is termed $\Delta B_{max}$, then the range of all frequencies present in the rotating frame is $\pm\gamma \cdot \Delta B_{max}$.

#### 2.5.2.1 Spatial Localization of the MR Signal by Frequency Encoding

In section 2.1, we discussed the time-domain and temporal frequency-domain representation of a signal. We will now revisit this concept, but in the context of spatial-domain and spatial-frequency domain to perform spatial localization of the MRI signal. Up until now, we followed the process of generating transverse magnetization in a given slice of interest. However, we now need a method to localize the MR signal from different spatial locations within that 2D plane. We will now explore the process of how the spins within the plane can be made to declare their unique location.

The most widely used approach to spatial encoding within the plane is to use methods known as *frequency encoding* and *phase encoding* respectively. As we will see, these methods define the Cartesian coordinates of spins within the plane independently and using orthogonal bases. The directions of these orthogonal bases are termed the frequency encoding and phase encoding directions. At this point it is helpful to note that these coordinates have a well-defined relationship to the physical coordinates of the object in 3D space and to the direction of the main magnetic field, but they can be arbitrarily defined by the direction of imposed magnetic field gradients as we will discuss. The three orthogonal axes defining the directions of the frequency-encoding, phase-encoding, and slice-encoding gradients are termed the *logical* gradient directions, denoted by $< u_{ro}, u_{pey}, u_s >$ as noted earlier.

If the MR signal is acquired during or in the presence of a constant magnetic field gradient,

$\vec{G}_{ro}$, along a particular direction, $\hat{u}_{ro}$, then the signal will become distributed over a range of frequencies that depend on the strength of the gradient and the location of the spins along the gradient direction by, $\gamma\vec{G}_{ro} \cdot \vec{r}$. Therefore, the Fourier transform of the acquired time signal should generate a one-to-one correspondence between time frequency and position. This gradient is named the *frequency encoding* or *readout* gradient.

If the receivers were able to capture the ***continuous*** signal, its continuous Fourier Transform would display peaks of each (demodulated) frequency, $\gamma\Delta B$, present with the amplitude of each peak being the vector sum of all transverse spins precessing at the given frequency. However, the requirement for discrete signal sampling means that we have to use the discrete Fourier transform. The sampling process discretizes and digitizes the signal by sampling at an interval, $\Delta t_d$, which is often referred to as the dwell time. A given sampling rate, $f_s = \frac{1}{\Delta t_d}$ encodes unambiguously for a bandwidth of frequencies in the range $\pm\frac{Bw_{ro}}{2}$, $Bw_{ro} = \frac{1}{\Delta t_d}$ . The discrete Fourier transform is periodic and as a consequence any spin ensemble with frequency greater than $\frac{\Delta t_d}{2}$ will be folded into the sampled bandwidth $[-\frac{1}{2\Delta t_d}, \frac{1}{2\Delta t_d}]$. This phenomenon is known as aliasing and has profound implications for the entire field of MRI and signal processing. Mitigating the consequences of aliasing is central to much of the work in my thesis.

No spatial localization along $\hat{u}_{ro}$ can be made in the absence readout gradient. Without this gradient being played during the readout, the signal will manifest as a single peak centered around 0 Hz. Every spin in the object will share the same frequency such there is no spatial localization. This is illustrated in Figure 2.6 for an ACR phantom.

#### 2.5.2.2 The Concept of k-Space

Up until now, we have considered the Fourier transform of a time-varying signal, which is expressed in temporal frequency. Because of $G_{ro}$ provides a linear relationship between frequency and projection of spin ensembles along $u_{ro}$, then the gradient must actually be

traversing the spatial frequency of the spin distribution during the MR readout. This spatial frequency is referred to as "k-space." In terms of equation 2.9, where $\Delta B = \vec{G}_{ro} \cdot \vec{r} + \delta B_0(\vec{r})$, each sampled timepoint in the readout, $n_{ro}$ can be expressed as:

$$\begin{aligned} S(n_{ro}) &= \int \vec{M}_{\perp}(\vec{r}, T_{rostart}) \cdot e^{-\frac{n_{ro}\Delta t_d}{T_2}} \cdot e^{-i2\pi\gamma n_{ro}\Delta t_d(\vec{G}_{ro}\cdot\vec{r}+\Delta B_0(\vec{r}))} dr \\ &\approx \int \vec{M}_{\perp}(\vec{r}, T_{rostart}) \cdot e^{-i2\pi\gamma n_{ro}\Delta t_d(\vec{G}_{ro}\cdot\vec{r}+\Delta B_0(\vec{r}))} dr \end{aligned} \tag{2.16}$$

where the readout starts at a time $T_{rostart}$ after excitation and the second line serves as an approximation for $N_{ro}\Delta t_d << T_2$. The exponential term describes the phase accrual of the transverse receives from the gradient and off resonance. By inspection, one can see the following as the Fourier inverse for the spatial distribution of spins along $u_{ro}$:

$$k_{ro}[n_{ro}] = n_{ro}\gamma G_{ro}\Delta t_d \tag{2.17}$$

Therefore, the time during the readout acts as a "dummy" variable k-space sampling. More generally, the application of gradients to manipulate spins for spatial encoding can be described as a function of time while any or a set of gradients, $\vec{G}$ is turned on:

$$k(\tau) = \gamma \int_0^{\tau} \vec{G}(t) dt \tag{2.18}$$

In Fourier sampling theory, the resolution of one domain corresponds to the encoded field of view (FOV) of its inverse. From equation 2.17, the encoded FOV along the $u_{ro}$ can then be described as:

$$\Delta k_{ro} = \frac{1}{FOV_{ro}} = \gamma \Delta t_d G_{ro} \tag{2.19}$$

However, during the acquisition, most vendors actually sample twice as fast as the prescribed dwell time, $\Delta t_d$, encoding for twice of the $FOV_{ro}$. This *oversampling* the readout does not impose any penalty on the acquisition time, and therefore provides a convenient way to avoid aliasing along $\hat{u}_{ro}$.

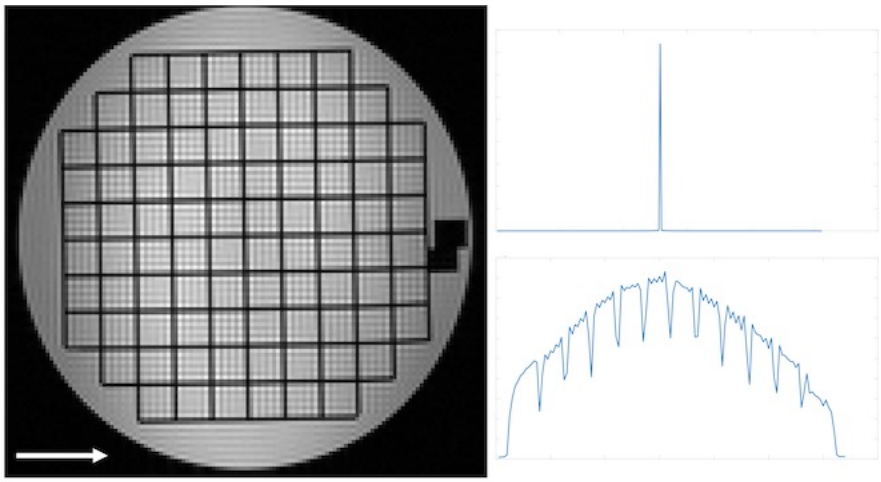

*Figure 2.6: The left is a picture of an ACR phantom which consists of a homogenous solution. The readout encoding direction is indicated by the white arrow. The top right shows the frequency response in the acquisition if no gradient is used to distinguish the spins off of their location along the readout direction. With proper shimming on a homogenous solution, all nuclei have essentially the same frequency during the readout without the presence of a frequency encoding gradient. The bottom shows the result if a frequency encoding gradient is used, which is a projection along the readout direction. An image can be formed if multiple readout projections are made (as initially done by Lauterbur [62]) or by using phase-encoding gradients [107].*

Up until now, we have seen that the MR readout consists of the sum of sinusoidal, or spatial-harmonic, functions, being provided by the frequency encoding gradient. For cases when $|\gamma \Delta B_0(\vec{r})| < \frac{Bw_{ro}}{N_{ro}}$, the Fourier transform of this gradient-induced frequency-encoded signal is a projection of the transverse signal distribution along the designated $\hat{u}_{ro}$, with a spatial resolution of $\frac{FOV_{ro}}{N_{ro}}$. If $|\gamma \Delta B_0(\vec{r})| > \frac{Bw_{ro}}{N_{ro}}$, errors in frequency encoding are observed, mis-mapping the anatomy along the readout direction.

#### 2.5.2.3 Readout Prephaser

The frequency-encoding gradient causes a phase dispersion across the readout FOV according to

$$\frac{\phi_{ro}(n_{ro})}{FOV_{ro}} = 2\pi\gamma n_{ro}\Delta t_d G_{ro} \tag{2.20}$$

By $n = \frac{N_{ro}}{2}$, the dephasing caused by $G_{ro}$ vectorially cancels transverse components across the readout FOV. This effectively contributes very little signal to the final reconstructed projection beyond $n_{ro}\Delta t_d/2$, leaving the second half of samples to be dominated by noise. Because of this, it is advantageous to include a readout *prephaser* that opposes the dephasing before the frequency-encoded readout begins. Including the prephaser will allow sampling to take place with the readout gradient induced intravoxel dephasing to satisfy $|\frac{\phi_{ro}(n_{ro})}{FOV_{ro}}| < \frac{\phi_{ro}(n_{ro}=\frac{N_{ro}}{2})}{FOV_{ro}}$, while still acquiring the $N_{ro}$ samples needed to satisfy the desired frequency encoding resolution. The refocusing of the spins during the readout from the dephasing of the spins caused by the readout prephaser is called a gradient recalled echo, or "gradient echo", or "GRE." Applying the prephaser before the readout changes to formulation of equation 2.16 to the following:

$$\begin{aligned} S(n_{ro}) &= \int \vec{M}_{\perp}(\vec{r}, T_{rostart}) \cdot e^{-i2\pi\gamma T_{pre}(\vec{G}_{rop}\cdot\vec{r})} \cdot e^{-i2\pi\gamma n_{ro}\Delta t_d(\vec{G}_{ro}\cdot\vec{r}+\Delta B_0(\vec{r}))} d\vec{r} \\ &= \int \vec{M}_{\perp}(\vec{r}, T_{rostart} \cdot e^{-i2\pi\vec{k}_{pre}\cdot\vec{r})} \cdot e^{-i2\pi n_{ro}\Delta\vec{k}_{ro}\cdot\vec{r}} d\vec{r} \end{aligned} \tag{2.21}$$

$T_{pre}$ refers to the duration of any prephasing done before frequency encoding begins and $\Delta B_0 \approx 0$. In the second line of equation 2.21, $k_{rop} = \gamma\vec{G}_{rop}T_{pre}$, serving as the k-space trajected by the readout prephaser. The $\Delta B_0(\vec{r})$ and $T_2$ decay components during $T_{pre}$ are absorbed into $\vec{M}_{\perp}(\vec{r}, T_{rostart})$ according to equation 2.14. For $G_{ro}$ to unwind the effects of the prephaser, it must have a polarity opposite to $G_{rop}$.

### 2.5.3 Phase Encoding

Frequency encoding the readout only provides the projection of the transverse magnetizations after an IFFT is applied, which isn't enough to provide an image for their 2D or 3D arrangement. T his readout signal is a sum of multiple spatial harmonic functions where all harmonic functions of the same $\hat{u}_{ro}$ coordinate have the same frequency, $\gamma\vec{G}_{ro}\cdot\vec{r}$. This does nothing to localize different spins along $\hat{u}_{pey}$ that are located along the same $\hat{u}_{ro}$, as illustrated in the frequency encoded plot of Figure 2.6. In order to distinguish $N$ harmonic signals, $N$ observations must be made with each observation having a different phase offset

between between the signals. In the case for MR imaging, if $N_{pey}$ and $N_{se}$ different localizations are needed to be made along $\hat{u}_{pey}$ and $\hat{u}_s$ respectively, frequency encoding must be repeated $N_{pey} \times N_{se}$ times with each having its own spatially-varying phase offsets along these two directions. This is illustrated in Figure 2.7 for a varying number of phase encoding steps. The phase offsets needed is achieved by applying a *phase encoding* gradient along $\hat{u}_{pey}$ or ($\hat{u}_{pey}$ and $\hat{u}_s$ if 3D imaging is being done), with the phase-encoding gradient achieving a different phase dispersion along the phase-encoding FOV for each readout. The gradient-induced dispersion is described by:

$$M_{\perp}^{n_{pey}}(\vec{r}) = M_{\perp}(\vec{r}) \cdot e^{-i2\pi\gamma n_{pey}\Delta G_{pey} T_{pre} y} \tag{2.22}$$

where $\Delta G_{pey}$ is a gradient along the $\hat{u}_{pey}$ direction and $n_{pey}$ is any integer such that $n_{pey} \in [-\frac{N_{pey}}{2}, \frac{N_{pey}}{2}]$. Equation 2.22 shows that applying a phase-encoding gradient before the readout creates an $n_{pey}$ factored harmonic across the $\hat{u}_{pey}$ direction, as illustrated in Figure 2.8. The same can be applied for the $\hat{u}_s$ direction in which case the notations for the gradient and number of phase-encoding steps are $\vec{G}_{se}$ and $N_{se}$ where se stands for "slice-encoding". This updates the signal equation of 2.21 to the following:

$$S(n_{ro}, n_{pey}, n_{se}) = \int \vec{M}_{\perp}(\vec{r}, T_{rostart}) \cdot e^{-i2\pi\gamma T_{pre}((\vec{G}_{rop} + n_{pey}\Delta\vec{G}_{pey} + n_{se}\Delta\vec{G}_{se})\cdot\vec{r})} \cdot e^{-i2\pi\gamma n_{ro}\Delta t_d(\vec{G}_{ro}\cdot\vec{r} + \Delta B_0(\vec{r}))} dr \tag{2.23}$$

If only one partition is desired along the slice direction, as in for 2D imaging, then $n_{se} = 1$. $G_{se}$ is often merged with the slice-select refocusing gradient. Given the phase-dispersion relationship in equation 2.22, equation 2.23 can be simplified if written in the k-space formalism. Adopting the k-space formalism alluded to in equation the k-space trajected during prephasing is:

$$k_{pre} = \gamma \cdot (\vec{G}_{rop} + \Delta\vec{G}_{pey} + \Delta\vec{G}_{se}) \cdot T_{pre} \tag{2.24}$$

where the amplitudes of $\Delta\vec{G}_{pey}$ and $\Delta\vec{G}_{se}$ are defined as

$$\begin{aligned} \Delta\vec{G}_{pey} &= \frac{\Delta k_{pey}}{\gamma T_{pre}} = \frac{1}{\gamma T_{pre} FOV_{pey}} \\ \Delta\vec{G}_{se} &= \frac{\Delta k_{se}}{\gamma T_{pre}} = \frac{1}{\gamma T_{pre} FOV_{se}} \end{aligned} \tag{2.25}$$

Given this (cookie-cutter) k-space formalism, assuming $\Delta B_0(\vec{r})$ effects are negligible, 2.23 can be simplified to 2.21 to the following:

$$S(n_{ro}, n_{pey}, n_{se}) = \int \vec{M}_{\perp}(\vec{r}, T_{rostart}) \cdot e^{-i2\pi(\vec{k}_{rop} + n_{pey}\Delta\vec{k}_{pey} + n_{se}\Delta\vec{k}_{se})\cdot\vec{r})} \cdot e^{-i2\pi n_{ro}\Delta\vec{k}_{ro}\cdot\vec{r}} dr \quad (2.26)$$

which is equivalent to

$$S(k_{ro}, k_{pey}, k_{se}) = \int \vec{M}_{\perp}(\vec{r}, T_{rostart}) \cdot e^{-i2\pi(\vec{k}_{ro} + \vec{k}_{pey} + \vec{k}_{se})\cdot\vec{r}} dr \quad (2.27)$$

where $\vec{k}_{ro} = \vec{k}_{rop} + n_{ro}\Delta\vec{k}_{ro}$, $\vec{k}_{pey} = n_{pey}\Delta\vec{k}_{pey}$, and $\vec{k}_{se} = n_{se}\Delta\vec{k}_{se}$ and $n_{ro}\epsilon(\frac{-N_{ro}}{2}, \frac{N_{ro}}{2}]$, $n_{pey}\epsilon(\frac{-N_{pey}}{2}, \frac{N_{pey}}{2}]$, and $n_{se}\epsilon(\frac{-N_{se}}{2}, \frac{N_{se}}{2}]$.

## 2.6 Parallel Imaging

MR imaging uses localized receivers in the form of a phased array. This results in significantly improved SNR from using the receiver within the bore. For a given array with $N_c$ channels, each channel will have its own spatial arrangement $C_l(\vec{r}), l \in [1, N_c]$. Based off of 2.26, the k-space readout of each channel can be described as:

$$S_l(k_{ro}, k_{pey}, k_{se}) = \int C_l(\vec{r})\vec{M}_{\perp}(\vec{r}, T_{rostart}) \cdot e^{-i2\pi(\vec{k}_{ro} + \vec{k}_{pey} + \vec{k}_{se})\cdot\vec{r}} dr \quad (2.28)$$

In this section and throughout this thesis, $I_j(\vec{r})$ will describe the complex value of the image of channel $j$ at location $\vec{r}$. $S_j(\vec{k})$ will describe the complex k-space value at coordinate $\vec{k}$ of channel $j$. The vectors $\vec{I}(\vec{r})$ and $\vec{S}(\vec{k})$ are $N_c \times 1$ vectors, where each entry are the channels image or k-space values. We will use $c_j(\vec{r})$ to refer to a channel's sensitivity at $\vec{r}$, and use $\vec{c_j}(\vec{r})$ to refer to the vector of all channel sensitivities.

In this section, we will whitening the data, combining the multi-channel data, and then how one could use localized channel sensitivity profiles to reduce the scan time.

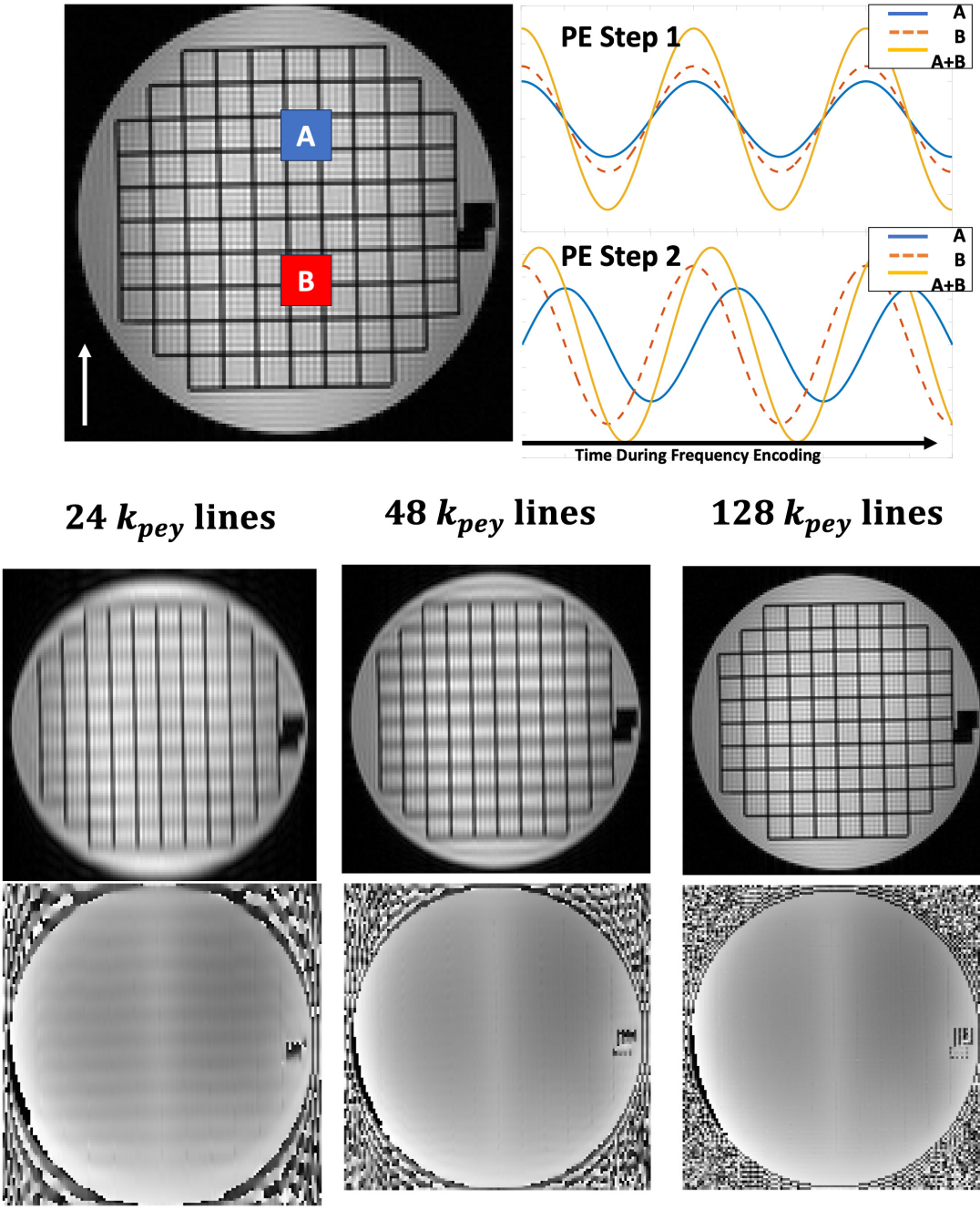


*Figure 2.7: Caption on next page.*

.

*Figure 2.7: Multiple readouts are needed, with each following a different phase dispersion along the $u_{pey}$ direction (white arrow) in order to distinguish two different points along its direction that have the same $u_{ro}$ coordinate, such as points A (blue) and B (red) in this illustration, as seen in Figure 2.6. This provides different phase shifts between spins at different $u_{pey}$ locations during frequency encoding. Therefore, $N_{pey}$ different phase dispersions along $u_{pey}$ (phase-encoding steps) are needed to distinguish $N_{pey}$ different points, with the greater value of $N_{pey}$ resulting in higher resolution along $u_{pey}$. This is shown in the bottom (magnitude on top and phase in the bottom) for cases where $N_{pey} = 24, 48,$ and $128$. The plot in Figure 2.6 corresponds to $N_{pey} = 1$ where sampling is done at $k_{pey} = 0$.*

### 2.6.1 Whitening

Mutual inductance is inevitable for channels in the phased array. This has subtle effects in the noise power amplitude of the combined image from the $N_c$ channels, $I_{com}(\vec{r})$ and results in each channel having its own noise variance. Whitening the data will decorrelate the data from the channels and result in the same noise variance for each channel.

Before an acquisition begins, a "noise" scan is done, where $N_\tau$ (usually $N_\tau = 512$) timepoints are sampled without any excitation. This acquisition leaves us with an $N_\tau \times N_c$ dimensional noise matrix, $N$. The correlation between the channels can be seen by multiplying the noise matrix by itself:

$$\Psi(N) = N^H N \tag{2.29}$$

where the $^H$ superscript indicates the Hermitian transpose. This correlation is shown in the top half of Figure 2.9 as noticeable off-diagonal entries. A whitened noise matrix, $N_w$, will satisfy $\Psi(N_w) = I_{d,N_c}$ where $I_{d,N_c}$ is an $N_c \times N_c$ identity matrix. A whitening transform, $W$, can be defined such that $N_w = NW$. Using the eigenvalue decomposition of the noise covariance matrix can be used to determine $W$. This decomposition is described by $\Psi(N) = V_N \Lambda_N V_N^H$ where $\Lambda_N$ is a diagonal matrix of the eigenvalues and the corresponding columns of $V_N$ hold the corresponding eigenvectors, normalized to value one. The whitening transform

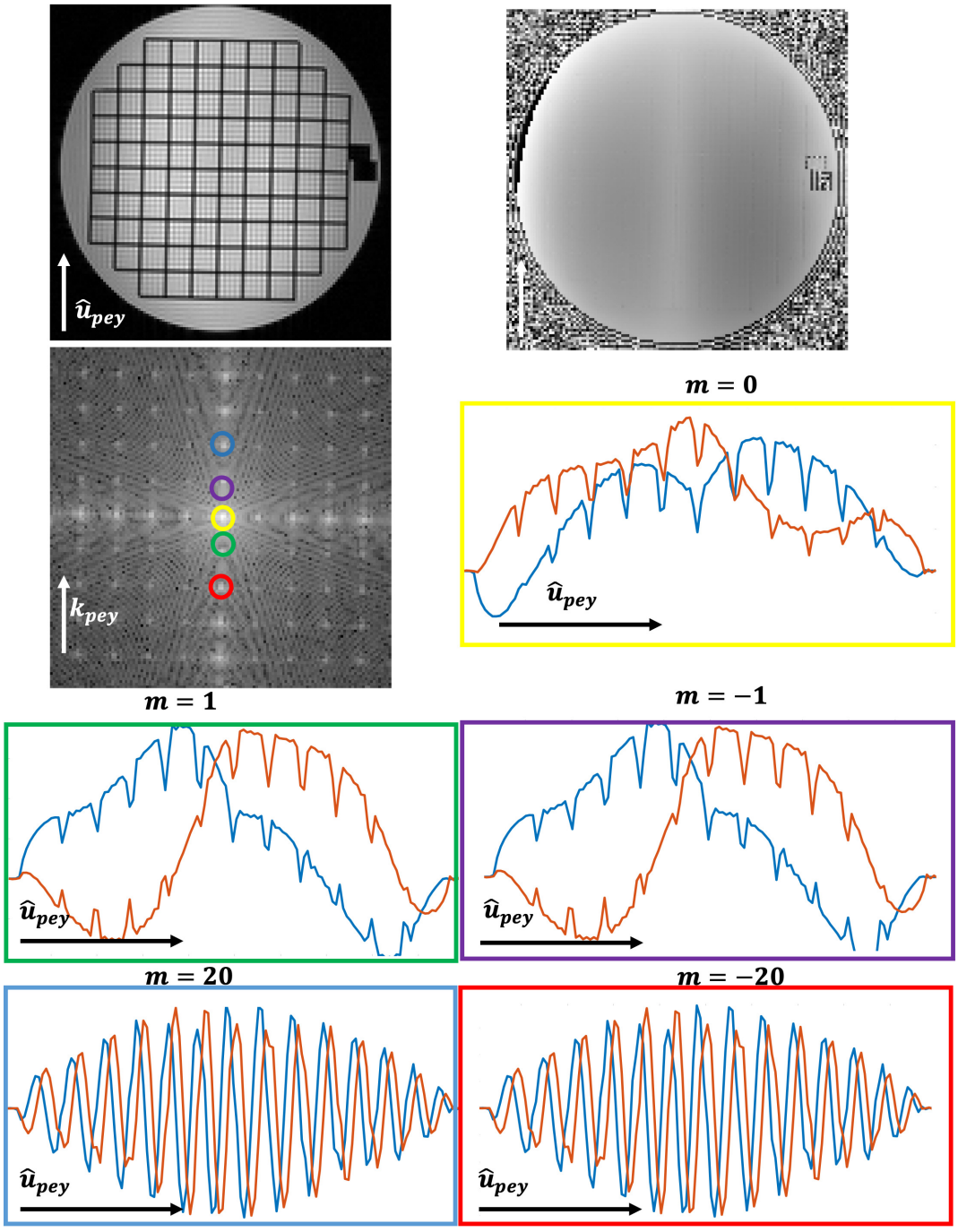


*Figure 2.8: Top row: magnitude and phase of the ACR phantom with the phase-encoding direction indicated by the white arrow. Beneath the magnitude image is a map depicting the log of k-space with the $\vec{k}_{pey}$ pointing vertically. The spatial harmonic phase-dispersion, induced by $G_{pey}$, across the phase-encoding direction is shown, with the color of the box corresponding to its indicated phase encoding step in the k-space map.*

can be determined below

$$\begin{aligned} N_w^H N_w &= I_{d,N_c} \\ (NW)^H(NW) &= I_{d,N_c} \\ W^H N^H NW &= I_{d,N_c} \\ W^H V_N \Lambda_N V_N^H W &= I_{d,N_c} \\ W^H V_N \Lambda_N^{\frac{1}{2}} \Lambda_N^{\frac{1}{2}} V_N^H W &= I_{d,N_c} \\ (\Lambda_N^{\frac{1}{2}} V_N^H W) &= I_{d,N_c} \\ W &= V_N(\Lambda_N^{-\frac{1}{2}}) \end{aligned} \tag{2.30}$$

Multiplying $\vec{I_l}^T(\vec{r})$ by by $W = V_N(\Lambda^{-\frac{1}{2}})$ transforms the data to a whitened vector space, where $^T$ is the transpose. The same can be done in k-space by post-multiplying $\vec{S_l}^T(\vec{k})$ by $W$. To have the whitened data in the original channel vector space, the whitening transform would have to be $W = V_N(\Lambda^{-\frac{1}{2}})V_N^H$ . For the rest of the thesis, any reference to channel data or noise data is assumed to have already been pre-whitened, unless otherwise mentioned. That is, all channel image/k-space data would have already gone through the whitening transformation. The whitened noise covariance matrix, $\Psi(N_w)$ is illustrated in the bottom half of Figure 2.9.

### 2.6.2 Combination

Roemer et al carried out an in depth evaluation of the SNR optimal phased array arrangement [117] and combination of the channel signals. The two methods he describes are the square-root sum of squares (SOS) and the spatial matched filter. The square root SOS is given by:

$$I_{sos}(\vec{r}) = \sqrt{|\vec{I_l}(\vec{r})^H \vec{I_l}(\vec{r})|} \tag{2.31}$$

The spatial matched filter provides SNR optimal combination while removing the greatest extent of local channel shading by using the distribution of the magnetic field generated

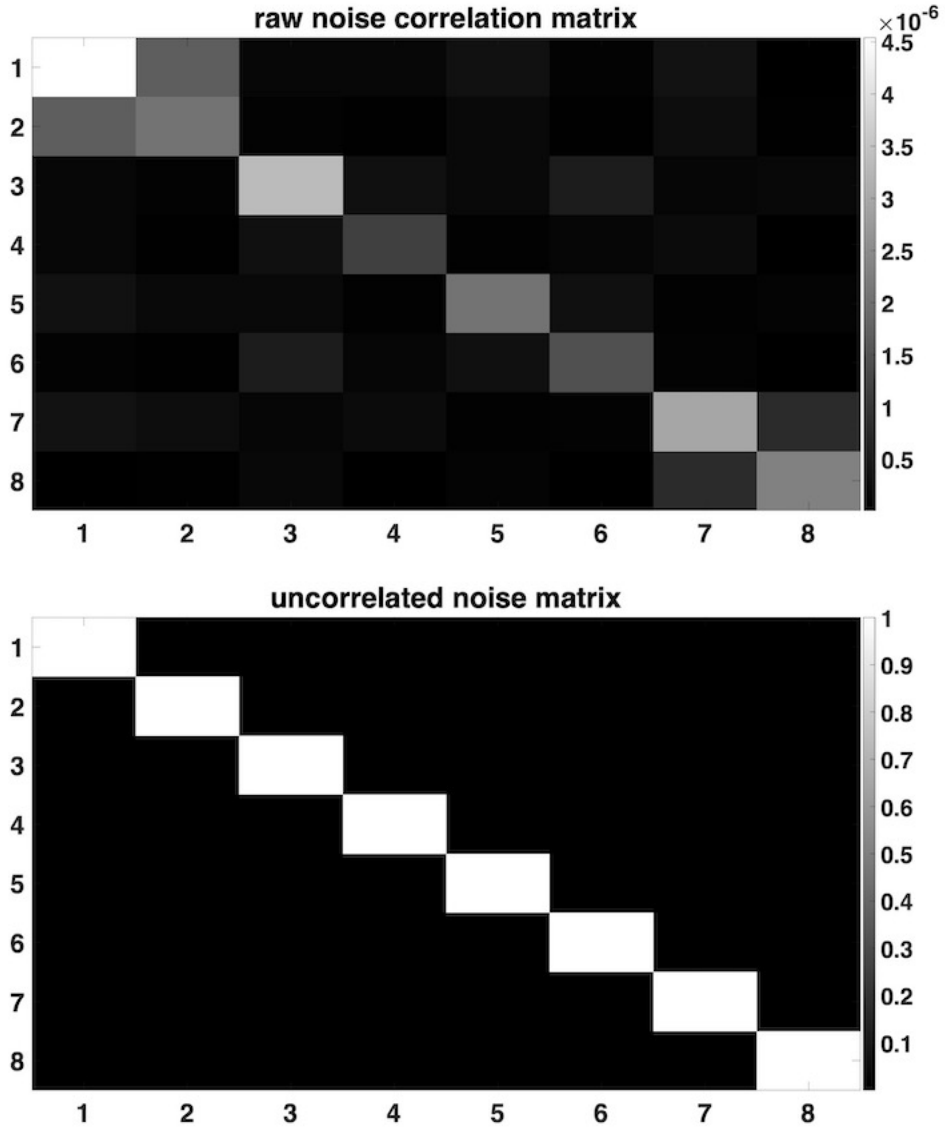


*Figure 2.9: Top the noise covariance matrix of raw noise data directly out of the scanner. The mutual inductance between channels in the phased array causes correlation between any two channels [117]. The whitening process described in equation 2.30 uncorrelates or whitens the receivers (bottom).*

.

by each channel (the sensitivity profile of each channel). Using the sensitivity profiles to estimate for a combined channel image preserves the relative phase the voxels. The weights for the spatial matched filter can be described as:

$$\vec{m}(\vec{r}) = \Psi^{-1}(N)\vec{c}(\vec{r}) \tag{2.32}$$

where $\vec{c}(\vec{r})$ is an $Nc \times 1$ complex vector giving the sensitivity for each channel. This ultimately gives a combined channel image as

$$I_{mf}(\vec{r}) = \vec{m}(\vec{r})^H \vec{I}(\vec{r}) \tag{2.33}$$

Properly estimating $\vec{c}(\vec{r})$ is difficult. One could do so by dividing the individual channel images by the square root sum of squares image or by dividing by an image from the body coil. An adaptive method to estimate for the optimal matched described by Walsh [122]. It borrows from the stochastic matched filter formulation of temporal signal processes commonly described in radar [121]. For each location $\vec{r}$, the weights needed to sum the channel entries are determined from a patch of voxels across all channels. A side-by-side comparison of Walsh and square root sum of squares is illustrated in Figure 2.10.

### 2.6.3 Parallel Imaging for Accelerated Acquisitions

In this section, we will go over common methods to reduce an acquisition in MRI that exploits multi-channel redundancy. In many cases, the acquisitions could be too long. Because the scan time scales linearly with the number of acquired phase encoding steps, $N_{pey} \cdot N_{se}$, reducing the number of encoding steps would provide a means of reducing the scan time. Skipping every $R$ k-space lines along a phase-encoding direction reduces the FOV by a factor of $R$, resulting in aliasing. Unaliasing is impossible with a single channel. However localized channel sensitivity profiles can be exploited to unalias as long as there is a significant difference in channel sensitivity profiles between superimposed pixels. This is illustrated in Figure 2.11.

Parallel imaging acceleration techniques rely on the use of a fully sampled, low resultion

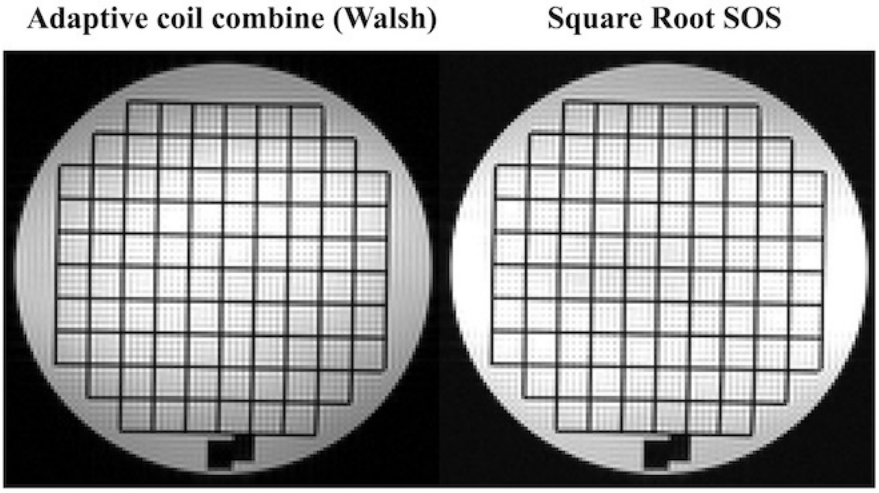


*Figure 2.10: Adaptive method from Walsh [122] on the left and square root sum of squares [117] on the right.*

.

calibration as a means of obtaining sensitivity profiles of each channel. For simplicity, and to save space, I will only discuss undersampling along the $k_{pey}$ direction. This can be easily generalized to the $k_{se}$. For *non-Cartesian* cases (which I don't plan on discussing), a lot of the techniques can be generalized across all three k-space coordinate axes.

#### 2.6.3.1 Sensitivity Encoded Unaliasing

A common method to unalias the image is by *explicitly* exploiting the localized channel sensitivity, called *sensitivity encoding* (SENSE). SENSE is a generalization of the spatial matched filter of equation 2.33 [90]. For *generous simplicity* when narrating SENSE, let's assume the noise covariance matrix is $\Psi(N) = I_{d,N_c}$. Then the matched filter becomes:

$$I_{comb} = \vec{c}^{H}(\vec{r})\vec{I}(\vec{r}) \tag{2.34}$$

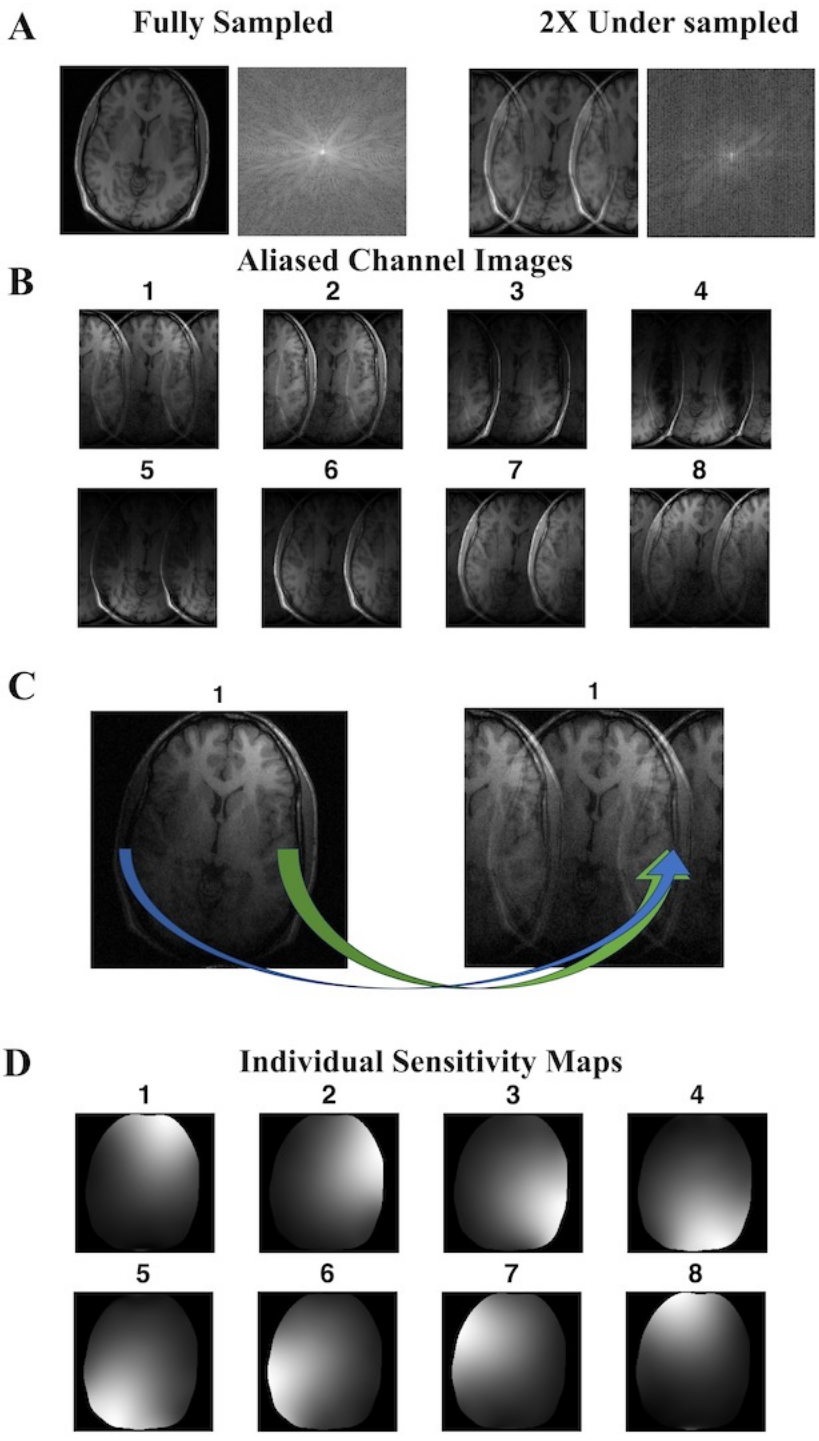


*Figure 2.11: Caption on next page.*

.

*Figure 2.11: (A) Coil combined images fully sampled data on the left and the same data with even numbered phase-encoding lines skipped (R=2) on the right. (B) The individual aliased channel images of the undersampled data. Pixels $\frac{FOV_{pey}}{R}$ apart superimpose on each in the aliased image with noticeable channel sensitivity differences (C). Localized sensitivity profiles of the individual channels (D) must be used to unalias the image. These sensitivity profiles can be determined from a low resolution calibration acquisition. As we will see later, channel sensitivities are explicitly used in image-based unaliasing, and they are implicitly used in k-space based unaliasing. Details of how the sensitivity profiles in (D) was calculated can be found in Appendix A.*

Equation 2.34 can be expanded into matrix form as:

$$\begin{bmatrix} I_1(\vec{r}_1) \\ I_1(\vec{r}_2) \\ ... \\ I_1(\vec{r}_{N_{vox}}) \\ I_2(\vec{r}_1) \\ I_2(\vec{r}_2) \\ ... \\ I_2(\vec{r}_{N_{vox}}) \\ ... \\ I_{N_c}(\vec{r}_1) \\ I_{N_c}(\vec{r}_2) \\ ... \\ I_{N_c}(\vec{r}_{N_{vox}}) \end{bmatrix} = \begin{bmatrix} c_1(\vec{r}_1) & 0 & ... & 0 \\ 0 & c_1(\vec{r}_2) & ... & 0 \\ ... & ... & ... & ... \\ 0 & 0 & ... & c_1(\vec{r}_{N_{vox}}) \\ c_2(\vec{r}_1) & 0 & ... & 0 \\ 0 & c_2(\vec{r}_2) & ... & 0 \\ ... & ... & ... & ... \\ 0 & 0 & ... & c_2(\vec{r}_{N_{vox}}) \\ ... & ... & ... & ... \\ c_{N_c}(\vec{r}_1) & 0 & ... & 0 \\ 0 & c_{N_c}(\vec{r}_2) & ... & 0 \\ ... & ... & ... & ... \\ 0 & 0 & ... & c_{N_c}(\vec{r}_{N_{vox}}) \end{bmatrix} \begin{bmatrix} I_{comb}(\vec{r}_1) \\ I_{comb}(\vec{r}_2) \\ ... \\ I_{comb}(\vec{r}_{N_{vox}}) \end{bmatrix} \tag{2.35}$$

$$\begin{bmatrix} I_1(\vec{r}) \\ I_2(\vec{r}) \\ ... \\ I_{N_c}(\vec{r}) \end{bmatrix} = \begin{bmatrix} C_1(\vec{r}) \\ C_2(\vec{r}) \\ ... \\ C_{N_c}(\vec{r}) \end{bmatrix} I_{comb}(\vec{r})$$

$$I(\vec{r}) = C_{sense} I_{comb}(\vec{r})$$

where $N_{vox} = N_{ro} \cdot N_{pey} \cdot N_{se}$ is the total number of voxels in an image and $\vec{r}_j$, with $j \epsilon [1, N_{vox}]$ refers to the location of each voxel. The second line of 2.35 is written in a block matrix format to conserve space. Each block matrix, $C_i(\vec{r})$, is a diagonal matrix with each being the complex channel sensitivity of location $\vec{r}_j$.

Equation 2.35 can be generalized as the following to describe aliasaing when skipping each $R$ $k_{pey}$ line (see Figure 2.11):

$$\begin{bmatrix} I_1(\vec{r}) \\ I_2(\vec{r}) \\ ... \\ I_{N_c}(\vec{r}) \end{bmatrix} = \begin{bmatrix} C_1(\vec{r}) & C_1(\vec{r} + \frac{FOV_{pey}}{R}\hat{u}_{pey}) & ... & C_1(\vec{r} + \frac{(R-1)FOV_{pey}}{R}\hat{u}_{pey}) \\ C_2(\vec{r}) & C_2(\vec{r} + \frac{FOV_{pey}}{R}\hat{u}_{pey}) & ... & C_2(\vec{r} + \frac{(R-1)FOV_{pey}}{R}\hat{u}_{pey}) \\ ... & & & \\ C_{N_c}(\vec{r}) & C_{N_c}(\vec{r} + \frac{FOV_{pey}}{R}\hat{u}_{pey}) & ... & C_{N_c}(\vec{r} + \frac{(R-1)FOV_{pey}}{R}\hat{u}_{pey}) \end{bmatrix} \begin{bmatrix} I_{comb}(\vec{r}) \\ I_{comb}(\vec{r} + \frac{FOV_{pey}}{R}\hat{u}_{pey}) \\ ... \\ I_{comb}(\vec{r} + \frac{(R-1)FOV_{pey}}{R}\hat{u}_{pey}) \end{bmatrix} \tag{2.36}$$

$$I(\vec{r}) = C_{sense,R} I_{comb}(\vec{r})$$

Where $I_{comb}(\vec{r})$ can be solved for by least-squares. A common way to estimate for the entries of the sensitivity matrix is to simply divide the image of each channel by their sum of squares (equation 2.31), followed by some filtering to smooth the data and threshold only for voxels with anatomical support. Figure **??** illustrates an example of unaliasing using SENSE. Another way to generate the sensitivity maps using principles described in the next subsection is detailed in appendix A.

As mentioned earlier, the channel sensitivity profiles are explicitly used to achieve the necessary spatial encoded to unalias the image. Although this narration featured a simplified explanation of the spatial matched filter, a thorough investigation on the ideal channel sensitivities used for the matched filter has the potential to achieve an SNR optimal parallel

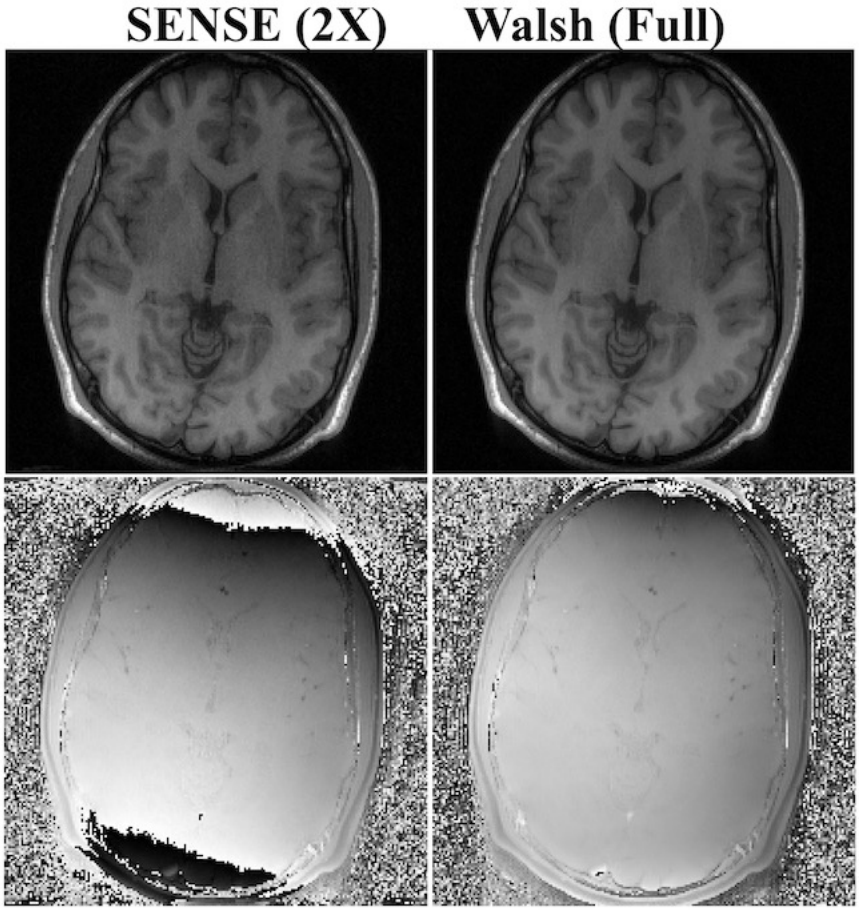


*Figure 2.12: SENSE reconstruction of R=2 using the sensitivity profiles shown in Figure 2.11 on the left [90] and fully sampled coil combining ("Walsh" [122]) on the right.*

.

imaging scheme.

#### 2.6.3.2 Estimating Phase Encoding Spatial Harmonics

Another point of view of unaliasing is to *mimic* the phase-encoding steps. These family of methods are "SMASH" based, which stands for *simultaneous acquisition of spatial harmonics* [104, 55, 52, 103, 75, 17]. As we recall from equation 2.22 and Figure 2.8 a single phase-encoding step, $n_{pey}\Delta G_{pey}$, disperses the spin ensembles along $\hat{u}_{pey}$ to form $n_{pey}$ harmonics of

the transverse magnetization. Equation 2.28 can be re-written as the following:

$$\begin{aligned} & S_l(k_{ro}, k_{pey}) \\ &= \int C_l(\vec{r})\vec{M}_\perp(\vec{r}, T_{rostart}) \cdot e^{-i2\pi(\vec{k}_{ro}+\vec{k}_{pey})\cdot\vec{r}} dr \\ &= \int C_l(\vec{r})\vec{M}_\perp(\vec{r}, T_{rostart}) \cdot e^{-i2\pi(\vec{k}_{ro}+(\vec{k}_{pey}+m_{pey}\Delta\vec{k}_{pey}))\cdot\vec{r}} \cdot e^{-i2\pi(-m_{pey}\Delta\vec{k}_{pey})\cdot\vec{r}} dr \\ &= \int e^{-i2\pi(\vec{k}_{ro}+(\vec{k}_{pey}+m_{pey}\Delta\vec{k}_{pey}))\cdot\vec{r}} \cdot C_l(\vec{r})\vec{M}_\perp(\vec{r}, T_{rostart}) \cdot e^{-i2\pi(-m_{pey}\Delta\vec{k}_{pey})\cdot\vec{r}} dr \end{aligned} \tag{2.37}$$

This implies that if $S_l(k_{ro}, k_{pey})$ is not explicitly acquired, it can be determined from an acquired k-space $S_l(k_{ro}, k_{pey} + m_{pey}\Delta\vec{k}_{pey}, k_{se})$ if a $-m_{pey}$ harmonic function weighted by the signal distribution is known. The channels are used in these SMASH based methods to mimic the spatial harmonics needed to complete the k-space grid. Based off of equation 2.37 the set of linear weights should be estimated from the following linear equation [103, 75]:

$$\begin{aligned} \sum_{l=1}^{N_c}\left[n_l^{(m_{pey})} \cdot \left(C_l(\vec{r})\vec{M}_\perp(\vec{r}, T_{rostart})\right)_{pey}\right] &= \left[n_l^{(m_{pey})} \cdot \left(f(\vec{r})\right)_{pey}\right] \cdot e^{-i2\pi(-m_{pey}\Delta\vec{k}_{pey})\vec{r}} \\ \sum_{l=1}^{N_c}\left[n_l^{(m_{pey})} \cdot \left(I_l^{cal}(\vec{r})\right)_{pey}\right] &= \left[n_l^{(m_{pey})} \cdot \left(f(\vec{r})\right)_{pey}\right] \cdot e^{-i2\pi(-m_{pey}\Delta\vec{k}_{pey})\vec{r}} \end{aligned} \tag{2.38}$$

where $\left(C_l(\vec{r})\vec{M}_\perp(\vec{r}, T_{rostart})\right)$ is the calibration image of the channel, $I_l^{cal}(\vec{r})$, and $f(\vec{r})$ is a spatial target fitting function. $\left(I_l^{cal}(\vec{r})\right)_{pey}$ and $\left(f(\vec{r})\right)_{pey}$ are the projection of the channel image and the target fitting function onto the phase-encoding axis, respectively. $n_j^{(m_{pey})}$ describes the linear weights from channel $l$ to estimate the $m_{pey}$ ordered spatial harmonic. These weights form a convolution kernel that works to estimate one k-space entry from neighboring entries across all channels. The target fit function should suitably describe a "ground truth" distribution of the transverse magnetization, $\vec{M}_\perp(\vec{r}, T_{rostart})$. However it is difficult to find a composite signal profile without avoiding destructive interference from the multiple channels. Because of this it was later shown that one could use the transverse magnetization distribution perceived by each channel [75]. Therefore, it makes more sense to treat each individual channel image, $I_l^{cal}(\vec{r})$ as the fitting function [75] where the k-space

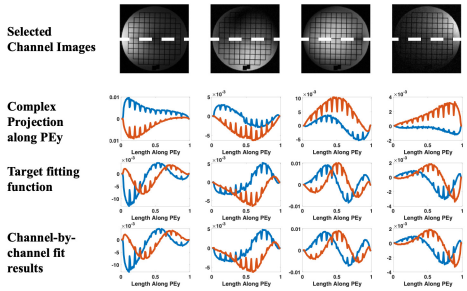


*Figure 2.13: An illustration of channel-by-channel SMASH fitting, where missing k-space indices of all channels are estimated as a linear combination of all channels. The top shows selected channel images, with the white line indicating the phase-encoding direction, $\hat{u}_{pey}$. The second row shows their projection onto the phase-encoding direction. The third row shows the fitting function the weights from equation 2.39, $\left(I_j^{cal}(\vec{r})\right)_{pey} \cdot e^{-i2\pi(-m_{pey}\Delta\vec{k}_{pey})\vec{r}}$. For this example we are fitting to harmonic $m_{pey} = 1$. The fourth row shows the estimation of the harmonic profile of each channel when doing the weighted sum of all channels.*

.

entry of a single channel is estimated from neighboring entries across all channels. This expands equation 2.38 to channel-by-channel fitting as follows:

$$\sum_{l=1}^{N_c}\left[n_l^{(m_{pey},j)} \cdot \left(I_l^{cal}(\vec{r})\right)_{pey}\right] = \left(I_j^{cal}(\vec{r})\right)_{pey} \cdot e^{-i2\pi(-m_{pey}\Delta\vec{k}_{pey})\vec{r}} \tag{2.39}$$

The weight, $n_l^{(m_{pey},j)}$ describes the coefficient to fit from channel $l$ to channel $j$. Figure 2.13 illustrates the harmonic functions achieved when doing a weighted sum of $(I_l^{cal}(\vec{r}))_{pey}$. These weights can then be used to estimate an unacquired k-space entry of a given channel as a linear combination of surrounding entries across all channels:

$$S_j(\vec{k}'_{ro}, \vec{k}'_{pey}) = \sum_{l}^{N_c}\left[n_l^{(m_{pey},j)} \cdot S_l(\vec{k}'_{ro}.\vec{k}'_{pey} + m_{pey}\Delta\vec{k}_{pey})\right] \tag{2.40}$$

Seeing this relationship in equation 2.40 makes it more convenient to solve for the weights from the calibration k-space: [55, 52]:

$$S_j^{cal}(\vec{k}'_{ro}, \vec{k}'_{pey}) = \sum_{l}^{N_c}\left[n_l^{(m_{pey},j)} \cdot S_l^{cal}(\vec{k}'_{ro}.\vec{k}'_{pey} + m_{pey}\Delta\vec{k}_{pey})\right] \tag{2.41}$$

k-Space estimations are improved when using *both* directions for fitting, such that $m_{pey} = 0, \pm 1, .. \pm M_{pey}$ [17, 43]:

$$S_j(\vec{k}'_{ro}, \vec{k}'_{pey}) = \sum_{l}^{N_c} \left[ \sum_{m_{pey}=-M_{pey}}^{M_{pey}} \left[ n_l^{(m_{pey},j)} \cdot S_l(\vec{k}'_{ro}.\vec{k}'_{pey} + m_{pey}\Delta\vec{k}_{pey}) \right] \right]_{m_{pey}\neq 0} \tag{2.42}$$

where $m_{pey} \neq 0$ because $m_{pey} = 0$ corresponds to $\vec{k}'_{pey}$ and $2M_{pey}$ is the total number of k-space neighbors used. In its current form, equation 2.42 only considers channel variations along the $\hat{u}_{pey}$. Despite the readout direction being fully sampled, this formulation can be extended by exploiting channel sensitivity variation along the $\hat{u}_{ro}$ direction when estimating for missing k-space entries. This will provide a more accurate estimate of the missing sample $(\vec{k}'_{ro}, \vec{k}'_{pey})$:

$$S_j(\vec{k}'_{ro}, \vec{k}'_{pey}) = \sum_{l}^{N_c} \left[ \sum_{\substack{m_{ro}=-M_{ro}, \\ m_{pey}=-M_{pey}}}^{M_{ro},M_{pey}} \left[ n_l^{(m_{ro},m_{pey},j)} \cdot S_l(\vec{k}'_{ro} + m_{ro}\Delta\vec{k}_{ro}, \vec{k}'_{pey} + m_{pey}\Delta\vec{k}_{pey}) \right] \right]_{\substack{m_{ro} \\ \wedge m_{pey}\neq 0}} \tag{2.43}$$

where $m_{ro}$ *and* $m_{pey}$ cannot both simultaneously equal zero because that corresponds to the unacquired target k-space coordinate, $\vec{k}'_{ro}, \vec{k}'_{pey}$ and $2M_{ro} \times 2M_{pey}$ is the $k_{ro} \times k_{pey}$ kernel dimension for the neighborhood. This formulation is known as commonly used for Generalized Autocalibrating Partial Parallel Acquisition (GRAPPA) [43]. A comparison of forward $(+m_{pey})$, negative $(-m_{pey})$, two-sided $(\pm m_{pey})$, and GRAPPA $(\pm m_{ro}, \pm m_{pey})$ are shown in Figure 2.14. Equation 2.43 implies that when using a phased-array that has coils with localized sensitivities at different regions across the imaging FOV, any element in k-space of a particular channel can be described as a linear combination of its surrounding neighbors across all channels.

Until now, we only determined unacquired k-space elements from their acquired neighbors. SPIRiT [67] was developed to estimate k-space elements from all members of the neighborhood by treating equation 2.43 as a constraint for the proper solution of k-space. That means, convolving the complete k-space with the kernel should output itself. This constraint,

along with consistency with acquired k-space data, is enforced iteratively until a solution for the complete k-space converges.

#### 2.6.3.3 Low Rank Modelling of Multi-Channel k-Space

Moving all terms of equation 2.42 to the same side results in the following

$$\sum_{l}^{N_c}\left[\sum_{\substack{m_{ro}=-M_{ro},\\ m_{pey}=-M_{pey}}}^{M_{ro},M_{pey}}\left[n_l^{(m_{ro},m_{pey},j)}\cdot S_l(\vec{k}'_{ro}+m_{ro}\Delta\vec{k}_{ro},\vec{k}'_{pey}+m_{pey}\Delta\vec{k}_{pey})\right]\right]_{\substack{m_{ro}\\ \wedge m_{pey}\neq 0}} - S_j(\vec{k}'_{ro},\vec{k}'_{pey}) = \sum_{l}^{N_c}\left[\sum_{\substack{m_{ro}=-M_{ro},\\ m_{pey}=-M_{pey}}}^{M_{ro},M_{pey}}\left[n_l^{(m_{ro},m_{pey},j)}\cdot S_l(\vec{k}'_{ro}+m_{ro}\Delta\vec{k}_{ro},\vec{k}'_{pey}+m_{pey}\Delta\vec{k}_{pey})\right]\right] = 0 \tag{2.44}$$

When $m_{ro}$ and $m_{pey} = 0$ (written as $m_{ro} \wedge m_{pey} = 0$), $n_l^{m_{ro},m_{pey},j} = -1$ when $l = j$ and equals 0 for all other values of $l$.

One could structure an autocalibration matrix, $\mathbf{A}^{\text{cal}}$, as the kernel convolves through k-space, with each row of $\mathbf{A}^{\text{cal}}$ being the vectorized entries of the kernel at each k-space location. Because each row of $\mathbf{A}^{\text{cal}}$ is the vectorized entries of a local k-space neighborhood, the linear dependence of local k-space neighbors described in equation 2.44 guarantees that there exists a null space of the entries of reach row of $\mathbf{A}^{\text{cal}}$ [129, 100]. The vectorized weights from GRAPPA [43] and SPIRiT [67] reside in this null space, $V_\perp$:

$$\mathbf{A}^{\text{cal}}\mathbf{V}_\perp^{\text{cal}} = 0 \tag{2.45}$$

This null space can be determined from the singular value decomposition (SVD) of $\mathbf{A}^{\text{cal}}$, where the singular vectors corresponding to the *insignificant* singular values are the null space. More of this is discussed in chapter 5.

The earliest approach that determined a null space from the calibration data these nullspace based methods include PRUNO [129], SAKE [100], LORAKS [48, 46, 47, 49], E-SPIRiT [118], ALOHA [63], and GIRAF [83].

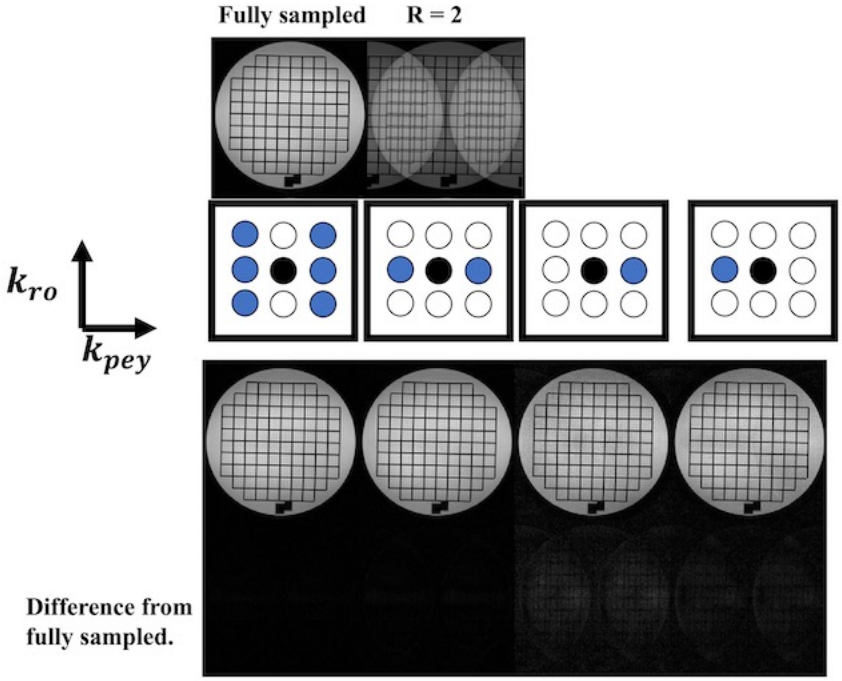


*Figure 2.14: A comparison of different fitting for SMASH-based parallel imaging. The top row shows the fully sampled image next to the aliased (R=2). The second row of images shows the following parallel imaging schemes from left to right: GRAPPA [43] fit from equation 2.43 with $M_{ro} = M_{pey} = 1$, bi-directional SMASH from equation 2.42 where $M_{pey} = 1$, $+m_{pey}\Delta k_{pey}$ harmonic fitting, and $-m_{pey}\Delta k_{pey}$ harmonic fitting for $m_{pey} = 1$. The last two columns correspond to channel-by-channel SMASH fitting [75]. The fitting in the right column is equivalent to the fitting seen in Figure 2.13. The target entries in the kernel is indicated by the black dot, while the neighbors used in the fitting are colored blue. The purpose of this figure is to illustrate the progression in harmonic fitting parallel imaging, which can be seen by the reduced difference in the difference map when scrolling from right to left.*

# CHAPTER 3

# Arterial Spin Labeling Magnetic Resonance Imaging Quantifies Tissue Perfusion Around Foot Ulcers

## 3.1 Introduction

Foot ulcers are a prevalent source of morbidity in diabetic patients and may lead to major amputation. Patients with diabetes have a 25% risk of developing a foot ulcer over their lifetime, leading to major amputation in 17% of them by one year [69, 102, 13, 79, 80]. Although neuropathy is the dominant etiology of foot wounds in the diabetic population, ischemia impacts 65% of these wounds [77]. A key factor in determining the healing potential of these wounds is the perfusion deficit in the limb. The physiologic assessment of limb perfusion is now a recommended standard practice for evaluation of patients with chronic limb threatening ischemia[110]. Yet the tools to quantify limb perfusion are deficient. The current tools to assess perfusion are either indirect or qualitative, not providing a quantitative assessment of perfusion. The use of indirect tools like ankle-brachial index and toe-brachial index are widespread and have been included in recent disease grading classification systems [54, 28]. However, these tools are limited by medial calcinosis and do not provide a localized assessment around a wound [93]. Transcutaneous oxygen measurement is another widely used tool whose sensitivity and its specificity for predicting wound healing in the diabetic population is higher than the aforementioned indirect tools [124]. However, this tool provides averaged data over large regions of the limb and is limited by tissue factors like edema

and vasoconstriction [42]. More recent qualitative methods including hyperspectral imaging and indocyanine green angiography can detail local tissue perfusion throughout the foot [27, 86, 116]. However, these tools limit their assessment to a superficial level and do not provide information on deeper tissue layers including muscle. Arterial spin labeling (ASL) is a non-invasive magnetic resonance imaging (MRI) technique that quantifies tissue perfusion at various tissue depths, without intravenous contrast. Clinically, it has been used in neuroimaging to quantify brain tissue perfusion [115, 53]. Briefly, it tags protons in blood with radio frequency pulses upstream from the tissue of interest. Images of the tissue of interest are acquired before and after perfusion with this labeled blood. Their subtraction yields a spatial map of perfusion throughout the imaged tissue. This has been applied to skeletal muscle in the extremities and more recently to the diabetic foot [130, 128, 33, 113].

The objective of this study is to investigate the novel application of ASL to assess foot perfusion in both healthy volunteers without wounds and diabetic volunteers with foot ulcers. This pilot study aims to quantify peri-wound foot perfusion at various tissue depths and compare this to foot perfusion in healthy volunteers.

## 3.2 Methods

### 3.2.1 Study Volunteers

To conduct this pilot study, 20 healthy volunteers were recruited from a university health campus and 10 diabetic volunteers were recruited from a university affiliated wound care center. All volunteers were required to be at least 18 years of age and be capable to undergo an MRI study. Additionally, diabetic volunteers were required to have an active foot wound, formally diagnosed diabetes mellitus via hemoglobin A1c or serial blood glucose examinations, and an objective physiologic assessment of macrovascular peripheral arterial disease with duplex ultrasound, ankle-brachial index, or toe-brachial index. Exclusion criteria for the healthy volunteers included structural or functional heart disease, diabetes, history of

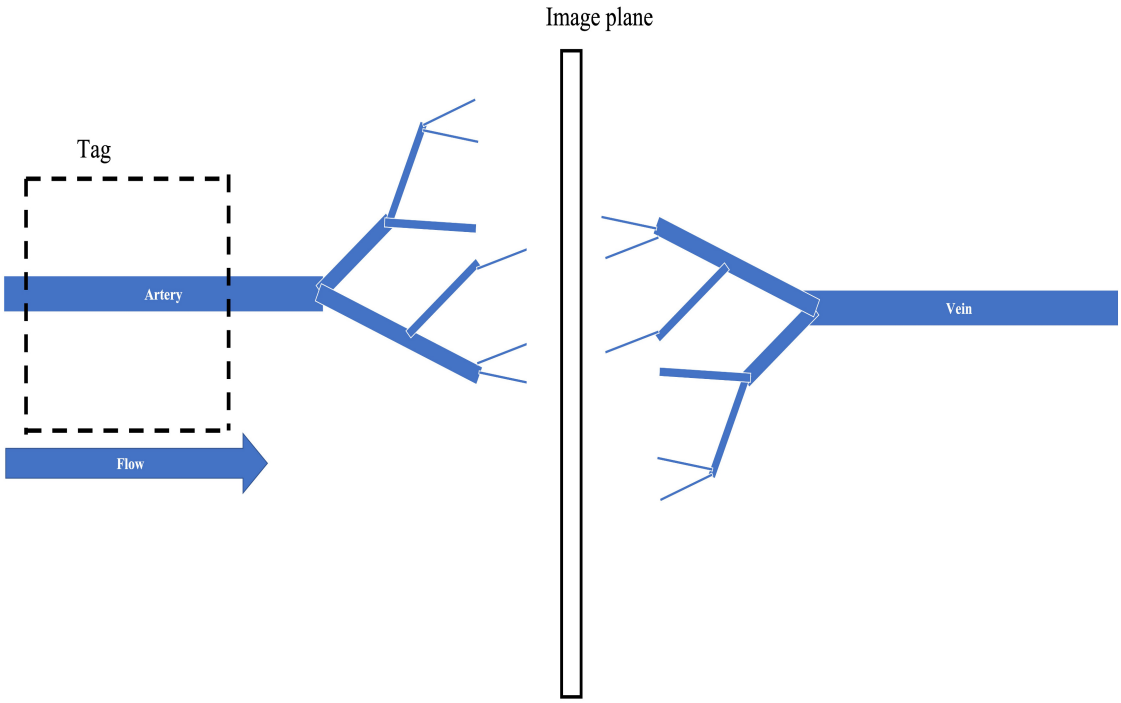


*Figure 3.1: A diagram illustrating the positioning of the tagging pulse targeting a slab upstream (arterial flow) from the target slice in ASL imaging. Once spins are tagged, they flow into the capillary bed where they exchange with water molecules in the tissue. Because the spins leaving the capillary bed into the target slice have already been perturbed by RF excitation from the tag, the NMR signal in the image acquisition is different from if they were entering the slice, completely unsaturated. This difference is how perfusion measurements are captured in (classical) ASL.*

peripheral arterial disease, claudication or rest pain in any extremity, arterial injuries of the lower extremities, active tobacco use, or an abnormal ankle-brachial index (less than 0.9). This study was approved by the Institutional Review Board of the University of California Los Angeles. Written consent was obtained from all volunteers prior to participation in the study.

### 3.2.2 Study Design

After obtaining consent and screening volunteers, the ankle-brachial index was measured in healthy volunteers. Since the diabetic participants already had objective assessment of macrovascular disease, ankle-brachial index was not measured at the time of the study. Next the participants were positioned supine on the MRI table with the foot of interest in a foot coil. All volunteers were allowed to rest for 5 minutes on the MRI table prior to commencing imaging. For healthy volunteers, the dominant foot was imaged while in diabetic volunteers, the foot with the wound was imaged. All imaging was performed on a 3.0T Siemens Magnetom Skyra MR system (Siemens Healthineers, Erlange, Germany). Scout images were initially obtained in the axial and sagittal planes. Then a high resolution T2-weighted image was obtained throughout the foot to discern soft tissue anatomy including wound edges. Finally, the arterial spin labeling sequence was performed using the same slice number and thickness. The ASL images were registered over the T2-weighted image, providing an anatomically aligned perfusion map. Healthy volunteers underwent a second round of imaging during sustained toe flexion. This imaging sequence was used to confirm the ability to detect changes in perfusion in an expected location in the foot. They were asked to plantarflex their toes such that they reduced the distance between the metatarsal head and the heel. This published method reduces the medial longitudinal angle of the foot and activates the intrinsic muscles of the foot especially the abductor hallucis muscle [57, 131]. The exercise was demonstrated and volunteers were allowed to practice. The volunteer's foot was once again placed in the foot coil. They were asked to flex their toes as

far as possible and hold the position throughout the duration of the study. Although they were asked to exert maximal force, there was no measure of the effort they exerted.

#### 3.2.2.1 Arterial Spin Labeling Technique

We specifically used pseudo-continuous ASL to measure tissue perfusion [29] Briefly, ASL administers two acquisitions: a control and tagging. Prior to either acquisitions, an inversion process is applied upstream to the tissue of interest. For pseudo continuous ASL, this inversion is only sensitive to flowing spins, borrowing from concepts of flow-induced inversion. Furthermore, the inversion is split into a series of low flip angle Hanning shaped radiofrequency pulses, having a lower energy deposition than a continuous adiabatic inversion. The inverted spins in the blood stream will enter the capillary bed and exchange with the water molecules in the tissue. What distinguishes the tagged from the controlled images are the net effects of the RF and gradients on the flow spins. For the tagging pulse, gradients are left turned on in between to cause a phase dispersion along the flow direction, which equal to the phase accumulation from a single continuous selective flow-induced in continuous ASL [126]. The cumulative effect of these pulses yields an inversion of the arterial flow spins. The control scan uses a similar pulse train, however each consecutive pulse tips the spins in the opposite direction and the slice select gradient is also balanced. This in zero net tip in the control pulse, while also having the same magnetization transfer effects as the tag pulse, leading to the difference between the tag and control images to not have any magnetization transfer effects.

After the control or tagging pulses, the upstream spins will flow into the capillary bed of the slice intended for imaging and exchange with tissue water. The inversion of the tagged spins limits the amount of excitable water molecules in the tissue of interest. Therefore, the signal difference between the control and tagged images is proportional to perfusion.

#### 3.2.2.2 Parameters

Our pseudo-continuous ASL acquisitions were based on a 3D Turbo Gradient Spin Echo's (TGSE) pulse sequence. It was employed with ten spin echo trains, a sixty-three echo-planar factor, a 38.44 ms effective echo time, 4300 ms repetition time, a fat saturation pulse, and an 1800 ms inversion time. We had an in-plane 192 x 192 mm field of view with a corresponding 64 x 64 in-plane matrix. A single slab was sampled which featured eight 3-mm slices parallel to the plantar foot or plane of the wound. With thirty averages, our scan was achieved in 8:40 minutes per foot.

#### 3.2.2.3 Perfusion Maps

An estimate of perfusion is proportional to the difference between the tag and control images and is based off the two compartment model between vascular and tissue components [4, 123].

$$\Delta M = \frac{2M_0 f \alpha}{\lambda R_{1\alpha}} [e^{-wR_{1\alpha}} - e^{-(\tau+w)R_{1\alpha}}] \tag{3.1}$$

where $\tau$ is the labeling pulse duration, $R_{1a}$ is the longitudinal recovery rate of the blood, $M_0$ is calf equilibrium magnetization, $w$ describes the delay time, $f$ is the tissue blood flow, $\lambda$ is the blood-tissue water partition coefficient, and $\alpha$ is the tagging efficiency. Modified to get a more accurate measure, the image acquisition was interleaved between labeling and control pulses. The assumed parameters values were 2 sec delay time, 1.5 sec label time, 0.8 tagging efficiency, 0.83 sec-1 longitudinal recovery rate, and a 0.8 g/mL blood-tissue water partition coefficient. We would subtract the control image from the label image for each voxel ($\Delta M'$), and then solve for the tissue flow with the parameters mentioned above.

### 3.2.3 Outcome Measurements and Data Analysis

For diabetic patients, the wound size, presence of infection, and vascular assessment were gathered during the pre-scan exam or from the electronic chart. Using this data, the Wound, Ischemia, and Foot Infection (WIfI) grades of the wounded limbs were calculated according

to previously published guidelines [77]. After imaging, a perfusion map was generated using custom image analysis software (MATLAB, MathWorks, Natick, MA) that implemented the FEAST perfusion calculation. A perfusion map was generated for each imaged ASL slice. Then a region of interest (ROI) was created around the foot at each slice on the T2-weighted images. The foot ROI for healthy volunteers was subdivided into lateral and medial plantar and calcaneal regions (Figure 3.2A). The medial and lateral division was between the 2nd and 3rd metatarsal while the plantar and calcaneal division was at the transverse tarsal joint. For the volunteers with wounds, the ROI (unique to each image slice) was sectioned into 4 areas: wound, proximal border zone, distal border zone, and remote zone. The proximal border zone is an area surrounding the wound that is 125 percent of the wound area while the distal border zone is 150 percent, both centered around the wound (Figure 3.2B). The remote zone is the tissue outside the distal border zone. When comparing diabetic and healthy volunteers, the entire ROI of the plantar foot in healthy volunteers corresponded to the remote zone in volunteers with wounds. In healthy volunteers, regional perfusion at rest and during sustained toe flexion were compared. The average remote zone perfusion in diabetic volunteers was compared to that in healthy volunteers at rest. Lastly, we compared the average perfusion amongst peri-wound zones.

### 3.2.4 Data Analysis

All perfusion values are expressed as mL/100g of tissue/min. Descriptive statistics are expressed as mean +/-standard error for quantitative variables and frequency (percentiles) for categorical variables. WIfI grades are expressed as median (range). Continuous variables were analyzed with regression using generalized linear mixed models, which can perform differences in means analysis for 2 or more group while accounting for both fixed and random effects. In each analysis, the individual was held as a random variable. The R Statistical package was used to perform all statistical analysis (Version 3.5.1, R Core Team, Vienna, Austria) [114].

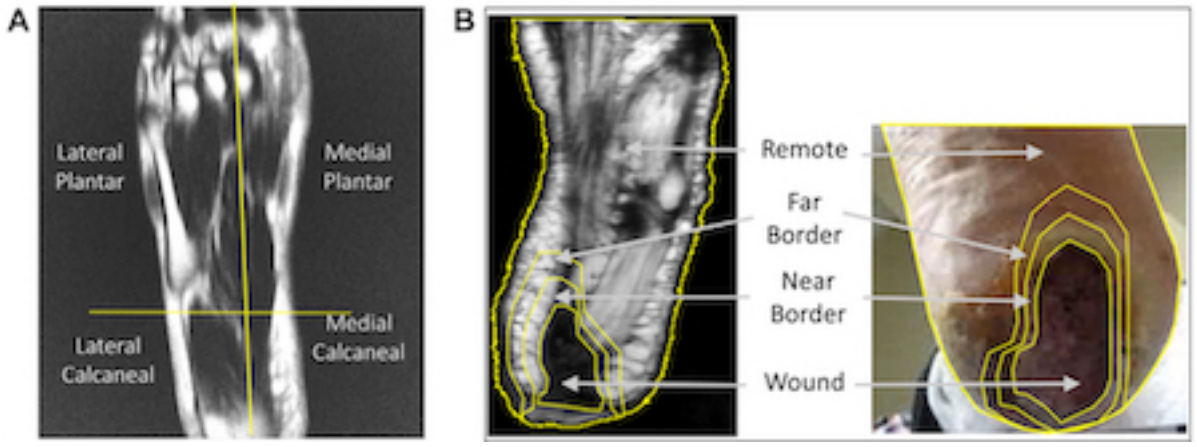


*Figure 3.2: The plantar foot of healthy volunteers (A) was segmented into the medial and lateral plantar and calcaneal regions while that of the diabetic foot (B) was segmented into the following peri-wound region: wound, near border, far border, and remote zones. We published this figure in [85]*

## 3.3 Results

#### 3.3.0.1 Volunteer Demographics and Wound Characteristics

The diabetic group of patients were older and had higher rates of smoking compared to the healthy volunteer group (Table 3.1). The ABI between the two groups were similar (1.0+/- 0.3 versus 1.1 +/- 0.03). Three patients in the diabetic group had undergone a transmetatarsal amputation in the past for infection. The diabetic group had a median WIfI stage of 2 (range: 1-3). The median wound grade was 2 (range: 1-3), ischemia grade was 0 (range: 0-1), and foot infection grade was 0 (range: 0-1). There was one volunteer with an ischemia grade of 1; the others had grades of 0. There were 3 volunteers with a foot infection grade of 1; the others had grades of 0. The mean duration of the wounds was 14.1+/-3.0 months and size was 4.3+/-1.9 cm2, at the time of the study. Wounds were located at the metatarsal head (5), heel (2), and at the transmetatarsal amputation stump (3).

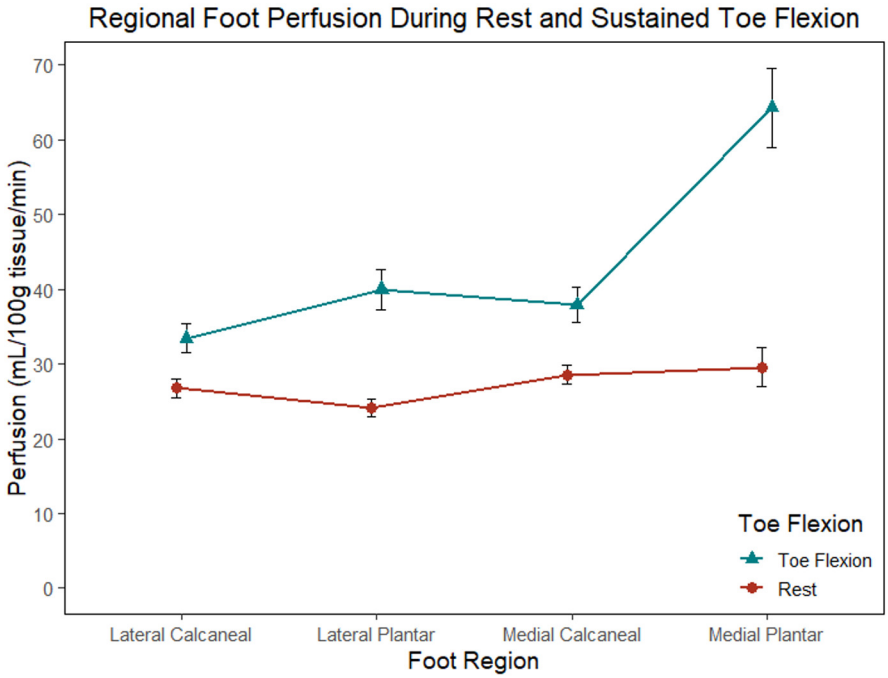


*Figure 3.3: Regional foot perfusion in healthy volunteers during rest and sustained toe flexion. We published this in [85]*

#### 3.3.0.2 Perfusion in the Plantar Foot

In healthy volunteers the average tissue perfusion in the plantar aspect of the foot at rest was 27.3+/- 2.7 mL/100g/min. There was no gradient of perfusion across the foot at rest (3.3). During sustained toe flexion the average foot perfusion was 43.9+/-1.7 mL/100g/min and was significantly different compared to rest (p¡0.001). The most substantial increase in perfusion occurred over the medial plantar foot during toe flexion compared to the resting state (64.3+/-5.3 vs 29.6 +/-2.6 mL/100g/min, p¡0.001). This increase in perfusion was detected throughout the thickness of the foot and most prominent superficially (Figure 3.4). The perfusion in the healthy plantar foot tissue was significantly higher in diabetics with wounds compared to healthy volunteers at rest (62.8+/-2.7 versus 27.3+/- 2.7 mL/100g/min, p<0.001).

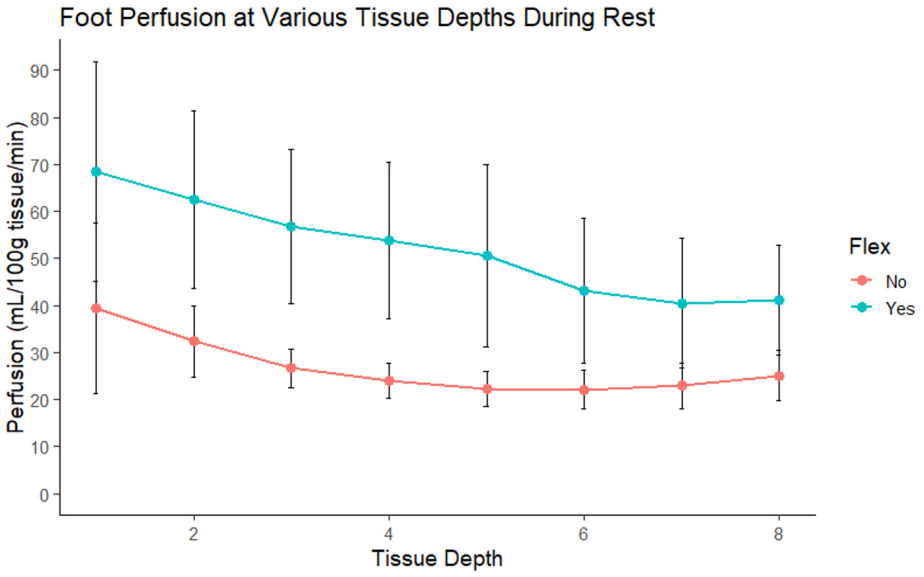


[scle=0.5]

*Figure 3.4: Plantar foot perfusion at various depths in healthy volunteers during rest and sustained toe flexion. We published this in [85]*

#### 3.3.0.3 Peri-wound Perfusion

There was a distinct perfusion gradient around the wounds in diabetic volunteers (Figure 3.5). Perfusion in the wound (96.1+/- 10.7 mL/100g/min) and the proximal border zone (92.7 +/- 9.4 mL/100g/min) was significantly higher than that in the remote zone tissue (62.8+/-2.7 mL/100g/min, p¡0.001 and p=0.002 respectively). There was no significant difference between the wound and proximal border zone perfusion (p=0.984). Perfusion at the distal border zone (73.4+/-8.2 mL/100g/min) was higher than the remote zone but not significantly (p=0.549). In Figure 3.6, the peri-wound perfusion pattern at various tissue depths can be seen. Tissue perfusion in the wound and proximal border zones are highest superficially. Furthermore, the difference in perfusion between peri-wound zones and the remote zone are not significant at greater tissue depths (Table 3.2). There was a marked decrease in perfusion at 60 percent of the wound depth in the wound region and proximal border. When comparing the wound and remote regions, the variation in perfusion at 60 percent is not significantly different (76.6 +/- 23.7 vs 56.7 +/- 6.7 mL/100g/min, p=0.403).

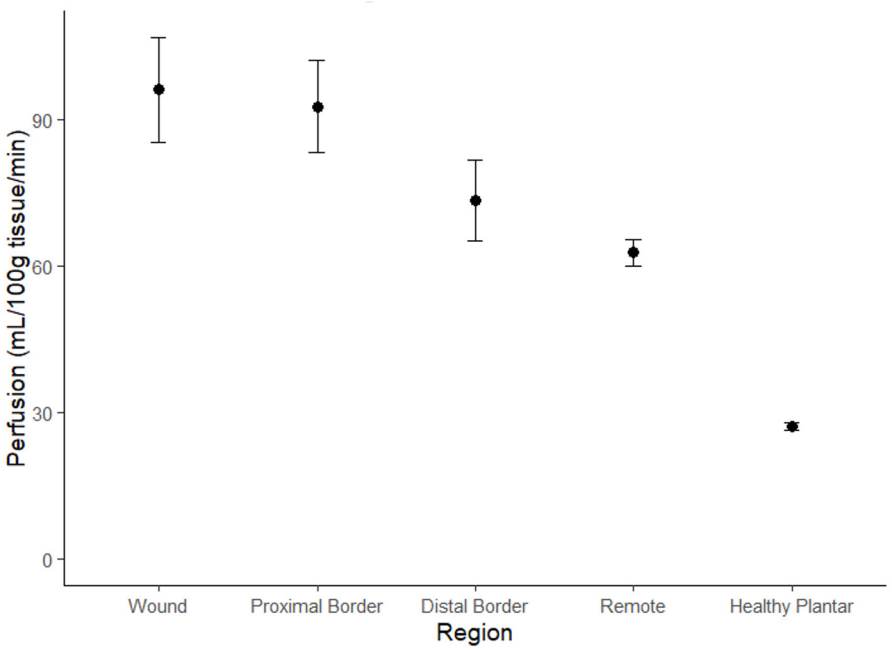


*Figure 3.5: Regional foot perfusion around nonischemic diabetic foot ulcers. We published this in [85]*

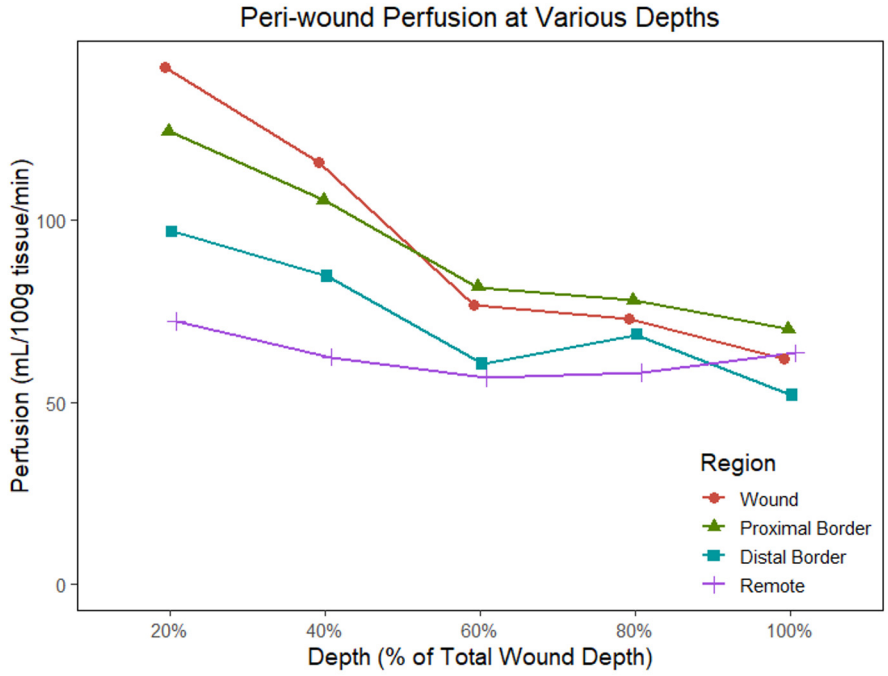


*Figure 3.6: Regional foot perfusion around nonischemic diabetic foot ulcers. We published this in [85]*

## 3.4 Discussion

Although adequate perfusion is paramount to healing diabetic foot ulcers, the tools to quantitatively and directly assess foot perfusion are currently lacking. This pilot study assesses the feasibility of using ASL, an MRI technique without the use of intravenous contrast, to measure foot perfusion both in healthy volunteers and diabetics with neuropathic wounds. Using ASL, we measured regional foot perfusion in the healthy foot as well as peri-wound perfusion. In healthy volunteers, there was a detectable increase in perfusion with activation of intrinsic foot muscles. In diabetics with neuropathic, non-ischemic wounds, we show that the foot is hyperemic relative to healthy volunteers at rest and that the peri-wound tissue is hyperemic compared to the tissue far from the wound.

Perfusion measurements of the plantar foot during toe flexion are in line with previously reported values, yet observed variations can be attributed to testing conditions and image processing. There was an expected increase in perfusion with maximal sustained toe flexion, compared to rest, with the largest increase at the medial plantar foot from 30 to 64 mL/100g/min. Zheng et al similarly found that plantar foot perfusion during subjective toe flexion (volunteers were told to flex and hold) was highest on the medial aspect at 93 mL/100g/min [130]. Edalati et al also found the greatest perfusion in the medial plantar foot during toe flexion in an MRI compatible dynamometer at 20% of their maximal effort, increasing to 17 from 9.8 mL/100g/min [33]. Though the type of exercise used to activate intrinsic foot muscles was similar, the degree of effort was variable in these studies. The image processing protocols also differed both in creating the region of interest used to average the imaging voxels and the thickness of imaging slices used to average perfusion. Lastly, the type of tissue included in the perfusion measurement also varied as some studies included only muscle while our study included all tissue. The variations in results suggests that perfusion measurements using ASL require consistency in imaging protocol and conditions to obtain reproducible measurements. In this study, we also described a quantitative peri-wound per-

fusion pattern that builds upon currently published qualitative perfusion patterns. We found that perfusion in the wound bed and the tissue immediately adjacent to the wound bed is hyperemic with an approximate 50% increase in perfusion compared to the tissue far from the wound. The peri-wound perfusion pattern is in line with qualitative perfusion patterns measured by other tools including near infrared imaging and laser speckle contrast imaging [7, 92, 59, 105]. The surprising result of increased perfusion does not agree with the recently published results of peri-wound perfusion analyzed by ASL. Edalati et al found that perfusion around the wound was reduced compared to tissue far from the wound (9.5 vs 8.6 mL/100g/min) [33]. However, this group only included skeletal muscle perfusion in their region of interest. In contrast, we included all tissues in the foot including superficial soft tissue, which is the tissue perfusion primarily measured by the aforementioned qualitative tools. This specific pattern of peri-wound perfusion is known to occur in healing wounds instead of stalled non-healing wounds where the perfusion pattern indicates a hypoperfused peri-wound region compared to the remote region [7, 41]. It is likely that the perfusion profile of these patients actively undergoing wound care, would reflect the perfusion pattern of healing instead of a stalled non-healing wound. However, this increased blood flow around a wound may not be sufficient to heal the wound, underlining the importance of a perfusion deficit. Currently, the perfusion threshold that would lead to wound healing has not been quantified nor are the factors that modulate this threshold known. Although, the pattern of perfusion is important, yet the quantification of perfusion provides more insight on the wound. Ultimately, a tool to quantify tissue perfusion will allow for the exploration of a wound's perfusion deficit and its implications on healing. The perfusion pattern along the wound depth may provide a more complete picture of the perfusion status of a wound. Currently, the direct assessment of tissue perfusion beyond the superficial layer is limited to indirect measures of perfusion like optical coherence tomography. Although these types of tools have been used in documenting angiogenesis at the wound edges along a tissue depth, their implications on wound healing are unknown [105]. In this feasibility study, we showed

that the peri-wound hyperemia diminishes along the tissue depth and nearly normalizes at the base of the wound. Increased wound depth has been associated with higher amputation rates and is used in wound clinical severity scores [77, 112, 6]. The implication of this perfusion pattern along the wound depth and the quantitative differences between superficial and deep tissue perfusion are unknown. There were several limitations in this feasibility study. The study group was small and recruited during a recurring wound care clinic day where there are a large number of diabetic patients with neuropathic wounds. The lack of patients with ischemic wounds limits the conclusions of this feasibility study. It is unknown whether the perfusion pattern seen in this cohort would be observed around ischemic wounds. Additionally, the conclusions drawn from the comparison between the healthy and diabetic groups were limited since their demographics were different. Furthermore, all of the diabetic patients were male further narrowing the applicability of its findings. The cohort demographics and lack of matching between the healthy and diabetic volunteers required study resources that were not available for this small feasibility study. Other seemingly feasible comparison groups like using the contralateral foot in diabetics as a control group were not possible secondary to logistical constraints of this feasibility study and went beyond the study's scope. Other features of the imaging modality that limited the study included image processing. There were small movements in the foot during the scan that we were unable to correct and may have contributed to measurement error. Lastly, the novel application of this imaging study precluded a standardized manner of imaging volunteers. Though we imaged all of the volunteers in the same fashion, there were some parameters that were not controlled such as the room temperature in the imaging suite, the volunteer's activity prior to the scan, or avoidance of substances that may affect perfusion. The significance of these uncontrolled factors on perfusion assessed by ASL is unknown at this time.

## 3.5 Conclusion

We have demonstrated the feasibility of using ASL MRI to quantify foot perfusion both in healthy volunteers and diabetic volunteers with neuropathic wounds. This imaging modality provides a non-invasive means of quantifying perfusion with standard medical equipment rendering granular of detail of foot perfusion throughout the volume of tissue. We have demonstrated that the perfusion around a non-ischemic diabetic foot ulcer is 1.5 times greater than perfusion tissue far from the wound and that the foot is hyperemic relative to the non-diabetic foot without a wound. The application of ASL to quantitative foot perfusion assessment is promising, yet requires larger study to elucidate its clinical implications on wound healing and the exploration of a wound's perfusion deficit.

| Characteristics | Diabetic Wounds (n=11) | Healthy Volunteers (n = 20) |
|---|---|---|
| Male sex | 11(100%) | 14(70%) |
| Age, years | $60.1 \pm 3.1$ | $26.8 \pm 0.8$ |
| Diabetes mellitus | 11(100%) | 0 |
| Current smoking | 7 (65%) | 0 |
| Ankle-brachial index | $1.0 \pm 0.3$ | $1.1 \pm 0.03$ |
| wound duration, months | $14.1 \pm 3.0$ | — |
| Wound Location: Metatarsal head, plantar | 5(45%) | — |
| Wound Location: Mid foot, planter | 1(9%) | — |
| Wound Location: Transmetatarsal amputation stump | 3(27%) | — |
| Wound location: Heel | 2(18%) | — |
| Wound area. $cm^2$ | $4.3 \pm 1.9$ | — |
| Wifi classification score: Wound | 2(1-3) | — |
| Wifi classification score: Ischemia | 0(0-1) | — |
| Wifi classification score: Foot infection | 0(0-1) | — |

*Table 3.1: Volunteer demographics and wound characteristics. Wifi stands for Wound, Ischemia, and Foot Infection. Data are presented as number (%), mean (standard error), or median (range). We published this table in [85].*

| % Depth | 20 | 40 | 60 | 80 | 100 | p Value |
|---|---|---|---|---|---|---|
| | | | | | | (20%$vs.$ 100%) |
| Region | | | | | | |
| Wound | $141.7 \pm 33$ | $115.5 \pm 23.6$ | $76.6 \pm 23.7$ | $72.6 \pm 14.6$ | $61.7 \pm 10.3$ | 0.015 |
| Near border | $124 \pm 35.6$ | $105.2 \pm 19$ | $81.5 \pm 15.8$ | $77.9 \pm 16.2$ | $69.9 \pm 10.1$ | 0.006 |
| Far border | $96.7 \pm 27$ | $84.4 \pm 17.5$ | $60.4 \pm 16.8$ | $68.5 \pm 16.7$ | $58.1 \pm 9.4$ | 0.27 |
| Remote | $72.1 \pm 6.1$ | $62.3 \pm 5.5$ | $56.7 \pm 6.7$ | $58.1 \pm 4.5$ | $63.4 \pm 7.5$ | 0.27 |
| p-value (wound, remote) | 0.0116 | 0.0115 | 0.403 | 0.322 | 0.322 | |

*Table 3.2: Volunteer demographics and wound characteristics. Wifi stands for Wound, Ischemia, and Foot Infection. Data are presented as number (%), mean (standard error), or median (range). We published this table in [85].*

# CHAPTER 4

# Slice Encoding for the Reduction of Outflow Signal Artifacts in Cine Balanced Steady State Free Precession Imaging

## 4.1 Introduction

Balanced Steady-State Free Precession (bSSFP)[84] is the workhorse in cardiac cine MRI for a wide spectrum of clinical indications [24, 35, 89, 1]. Of the broad family of "steady-state" sequences–those whose kernel demands repetitions to be short and frequent enough to achieve eventual equilibrium between the magnetization's relaxation and recovery [87, 125, 45, 44] bSSFP has become the imaging technique of choice for many cardiac MRI applications. The kernel in bSSFP lacks any net gradient-caused intravoxel phase dispersion and has a $\pi$ rad/TR incremental RF-phase ramp, causing off-resonance induced dephasing to be almost completely refocused midway between pulses [97, 96]. This effect credits bSSFP readouts with relatively high signal-to-noise ratio (SNR) and T2/T1 signal-dependence, both of which are useful for enhancing blood-myocardium contrast [35, 34, 101].

Unfortunately, the features providing bSSFP with the aforementioned benefits also make it vulnerable to flow-effects. With balanced gradients, excited spins leaving the slice linger on, tapering-off via T2-decay to ultimately contribute to the bulk signal [73]. Therefore, a signal profile originally intended for 2D space spans a 3D volume. This outflowing signal

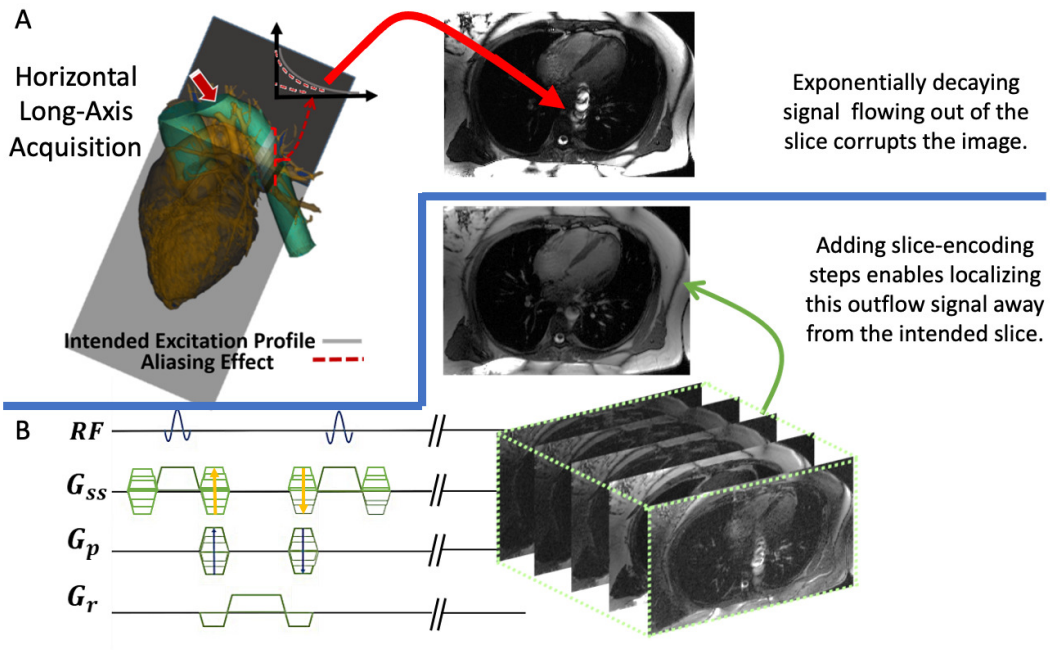


*Figure 4.1: An overview describing our proposed sequence. (A) The slice intended to be acquired is positioned through a heart's horizontal-long axis (HLA), which is penetrated by the descending aorta. Any through-plane flow from the aorta will have signal tapering off via T2 decay. Having this unaccounted for will have the out-of-slice signal corrupting the final image as indicated by the red arrow. (B) Our proposed sequence is displayed: adding slice-encoding steps to treat the signal as a 3D space, without any change to the 2D excitation's profile. Upon a 3D IFFT the final image will be found in the center-partition without any influence from the out-of-slice spins, which will be spatially encoded to their respective locations. We published this in [3]*

aliases along the axis it is projected on, as illustrated in Figure 4.1, causing commonly seen outflow artifacts in cine imaging [72]. These artifacts include a coherent out-of-slice (OOS) contribution mis-projected onto the intended slice during the readout, often appearing as an erroneous signal pileup, and "ghosts" or "zippers" that run along the phase-encoding direction [111].

The extent of the outflowing spins' impact on the images depends on their off-resonances. Markl et al. called this coherent sum of the OOS spins "frequency offset-dependent outflow effects" [72, 73]where outflowing spins exhibit noticeable signal enhancement. This is most

particular for isochromats with $\pi$ rad/TR phase accumulation and is visualized in Figure 4.2. The on-resonance spins, by definition, don't have added phase accrual in the rotating frame. The $\pi$ rad/TR RF-phase ramp will therefore cause adjacently excited inflowing on-resonance spins to cancel, while causing adjacently excited $\pi$ rad/TR spins to add coherently. Outflowing spins are still subject to the MRI bore's gradients. As such– as long as they are in the receivers' sensitivity region–they are prone to be mis-frequency-encoded, causing their mis-projection onto the resulting slice15. Further complications arise if the flow is pulsatile: inconsistent spin-inflow contributes to signal phase variations between adjacently acquired k-space lines, causing mis-encodings ("zippers") along a Cartesian grid's phase-encoding direction [95]. This provides three main "ingredients" for the flow artifacts in bSSFP cardiac cine imaging: existence of outflowing spins, those spins having off-resonance, and them having pulsatile time-varying velocities [72, 73, 111, 95, 108]. The first two ingredients pose issues for the frequency-encoding direction because any tipped spin in the receiving coils' proximity contributes to the bulk signal during the readout [72]. The third contributes to phase-encoding issues because the pulsatile spin-inflow between adjacent k-space lines varies the bulk signal's phase between readouts [95].

Schar et al. carried out an in-depth evaluation on 3T cine-bSSFP imaging, emphasizing the importance of localized shimming [95] to mitigate off-resonance effects. This was similar to Deshpande et al's 1.5T work on coronary artery imaging, which proposed pursuing pre-scans to find the appropriate central frequency to limit the outflow artifact's extent [32]. Unfortunately, this method requires a "trial and error" approach for acquiring an image with minimal outflow corruption. Datta et al. proposed having a net through-plane dephasing gradient in the bSSFP acquisition in an attempt to cancel out the outflowing spins [30]. The overall outflow signal intensity from the bSSFP stopbands is reduced as a result; however, the range of off-resonances showing noticeable outflowing signal is widened. The dephasing gradient also does not discriminate between in-slice versus out of slice, corrupting the slice's actual signal. Bieri et al. carried out work to reduce mis-phase-encoding in bSSFP imag-

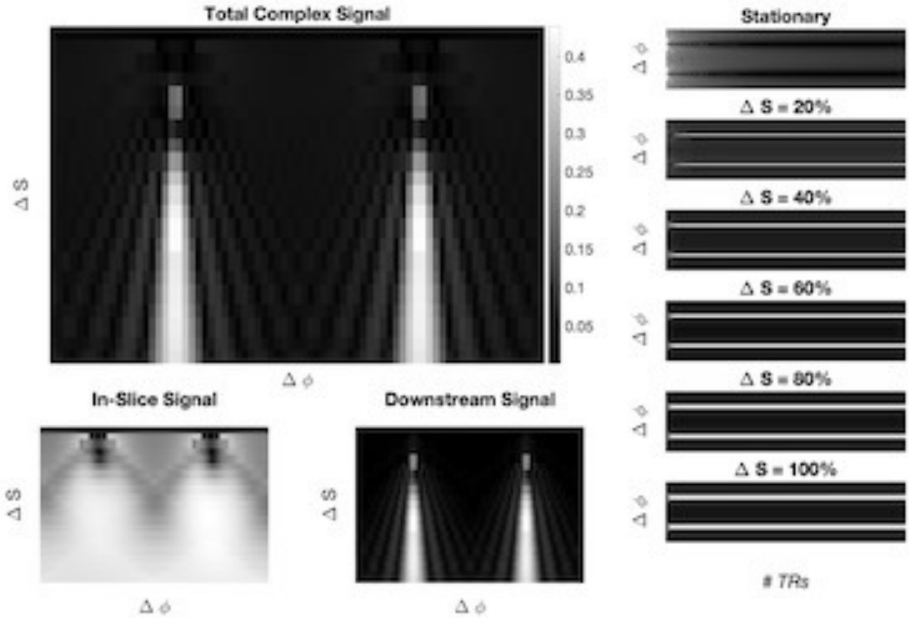


*Figure 4.2: Bloch-simulated results with the following parameters: Flip angle = 60°, TR = 4ms, T1/T2 = 100/150 ms, off-resonance accrual per TR, $\Delta\phi = [-2\pi, 2\pi]$, fractional spin-replacement rate $\Delta s \epsilon [0, 1]$, with a six-millimeter slice-thickness after 300 excitations. Right column: the approach to steady state equilibrium for the moving spins for selected fractional spin-replacement rates over a range of off-resonances. As Markl et al discussed [73], the moving spins on the off-resonant bands add up coherently, leading to an out-of-slice signal-enhancement. Left: Signal profiles from the sum of all spins (top, within the nominal slice (bottom left) and all downstream spins (bottom right) for a range of spin-replacement rates and off-resonances. The scaling similarities between the downstream and the total signal makes it clear that much of the bulk signal is contributed from the downstream spins. We published this in [3]*

ing. Originally intended for eddy current-induced phase-offsets in bSSFP imaging [10], he attempted to null the bulk-signal's flow-induced phase offsets with adjacent readouts. The method assumed adjacent k-space lines would have similar in-flow induced phase-accrual [9]. Therefore, bSSFP's linear RF phase ramp would contribute to cancelling their phase-accumulation if their readouts were consecutively acquired, minimizing the appearance of zipper artifacts. However, this method does not address the fact that there is still unlocalized signal beyond the imaged slice, letting it contribute to the acquisition's readout. Because outflowing spins gives the signal a 3D profile, we hypothesized that their associated artifacts can be reduced if they are spatially encoded for. As such, we propose adding through-slice phase-encoding steps ("slice-encoding") to increase the acquisition's through-slice field of view (FOV) beyond the nominal slice-thickness to localize this outflowing signal. We tested this hypothesis with Bloch-simulations, phantom scans, and on nineteen healthy volunteers.

## 4.2 Theory

### 4.2.1 Outflowing Signal

To conceptualize outflowing signal, imagine a system of through-plane flowing spins moving at a velocity $v$ and has already achieved steady equilibrium. Each ensemble of spins has its own specified off-resonant phase-accumulation per TR $\phi$ and will leave the slice with its magnitude decaying according to [73]

$$A_{\phi OS}(t) = A_{\phi 0} e^{\frac{-t}{T_2}} \tag{4.1}$$

where $t$ is the elapsed time from when it left the slice, with magnitude $A_{phi0}$. This equation can be expressed in terms of distance downstream from the slice, $\vec{r_s} = v_s \cdot t$. However, to get a sense of how impactful the OOS signal is to the entire acquisition, it makes sense to convey Equation 1 in terms of fractional spin-replacement rate, $\Delta s$ [72]. This describes the number of spins inflowing at each TR as a fraction of the slice's full capacity. With a nominal

slice-thickness, $S_T$, the flow's velocity is related to $\Delta s$ as:

$$v_s = \frac{\Delta s S_T}{T_R} \tag{4.2}$$

The out of slice amplitude from Equation 1 can then be expressed in terms of $\vec{r}_s$:

$$A_{\phi OS}(\vec{r}_s) = A_{\phi 0} e^{\frac{-|\vec{r}_s| T_R}{\Delta s S_T T_2}} \tag{4.3}$$

This relationship (Equation 4.3) argues for a more powerful case of the OOS spins' severity than a mere $\frac{|\vec{r}_s|}{v_s}$ substitution for $t$, showing that even slow ensembles could significantly corrupt the image if its nominal thickness is small.

It must be noted that this conceptualization is brief in that it discusses only a single outflowing ensemble. This narration does not analytically define the total acquired signal as a sum of all the spin ensembles within and outside of the imaging slice; however, the phenomenon it conveys is the cause of the image artifacts we aimed to remove with experiments detailed in the Methods section.

#### 4.2.1.1 Flow Compensation

Bieri et al. proposed two flow-compensation based techniques to limit flow effects in bSSFP [9]: the k-space pairing technique and M1 nulled gradient waveforms. Both aimed to eliminate the variable bulk signal phase when imaging with pulsatile flow. Eliminating this velocity-induced phase accumulation does well to minimize the bulk signal's phase variability from line-to-line in k-space, however it does not eliminate the outflowing signal.

### 4.2.2 Pulse Sequence

We propose the pulse sequence illustrated in Figure 4.1B to mitigate the aforementioned artifacts, which includes Fourier spatial encoding along the slice-select's direction. The resulting data has a through-slice resolution, $\Delta z$, typically chosen as the nominal slice-thickness. With $N_{SE}$ total partitions, the effective through-slice FOV is expanded to $N_{SE}\Delta z$,

describing the through-slice k-space resolution as $\Delta k_s = \frac{1}{N_{SE}\Delta z}$. According to equation 2.25 incremental gradient-lobe amplitude needed to achieve such a k-space resolution can be solved as $\Delta G_{SE} = \frac{2\pi}{\gamma N_{SE}\Delta z T_{SE}}$, with $T_{SE}$ being its duration. These slice-encoding steps would give the raw data three spatial dimensions, unlike two for the standard bSSFP sequence. After a 3D inverse Fourier transform is performed on k-space, the final image unfolded from the outflow artifacts will be held in the center slice. The additional up-and-downstream slices of the 3D space will serve as a buffer to tolerate outflow-induced aliasing, before the target image is contaminated.

## 4.3 Methods

### 4.3.1 Bloch Simulation

Much of the following was based off of the Bloch simulation designed by Markl et al [72]. The Bloch simulations made for this study investigated the physical effects involved and sought to assess how those effects impact the acquisition. This is illustrated in Figure 4.3.

The physical effects included in this investigation were through-plane flow, an imperfect slice excitation-profile, and coil sensitivity. An array of equally spaced spin ensembles was arranged along the slice-select's direction. The excitation profile's full width at half maximum (FWHM) –the imaging slice– was divided into $N_s$ subslices. The flow's motion was modeled by a downstream shift of the ensembles by $\Delta s$ $N_s$ subslices per TR. This simulation had to include all measurable transverse magnetizations in their complex sum for the bulk signal. Therefore, estimating an appropriate number of downstream subslices, $N_{os}$, must consider the spins' T2 relaxation. The transverse magnetization loses relevance beyond 3 T2 time constants after excitation, suggesting $N_{os} = \Delta s N_s 4T_2/T_R$.

Parameters were set to have $N_s = 20$, TR = 4ms, and bloodlike relaxation properties of T1/T2 = 1000ms/150 ms. The number of upstream subslices was made equal to the down-

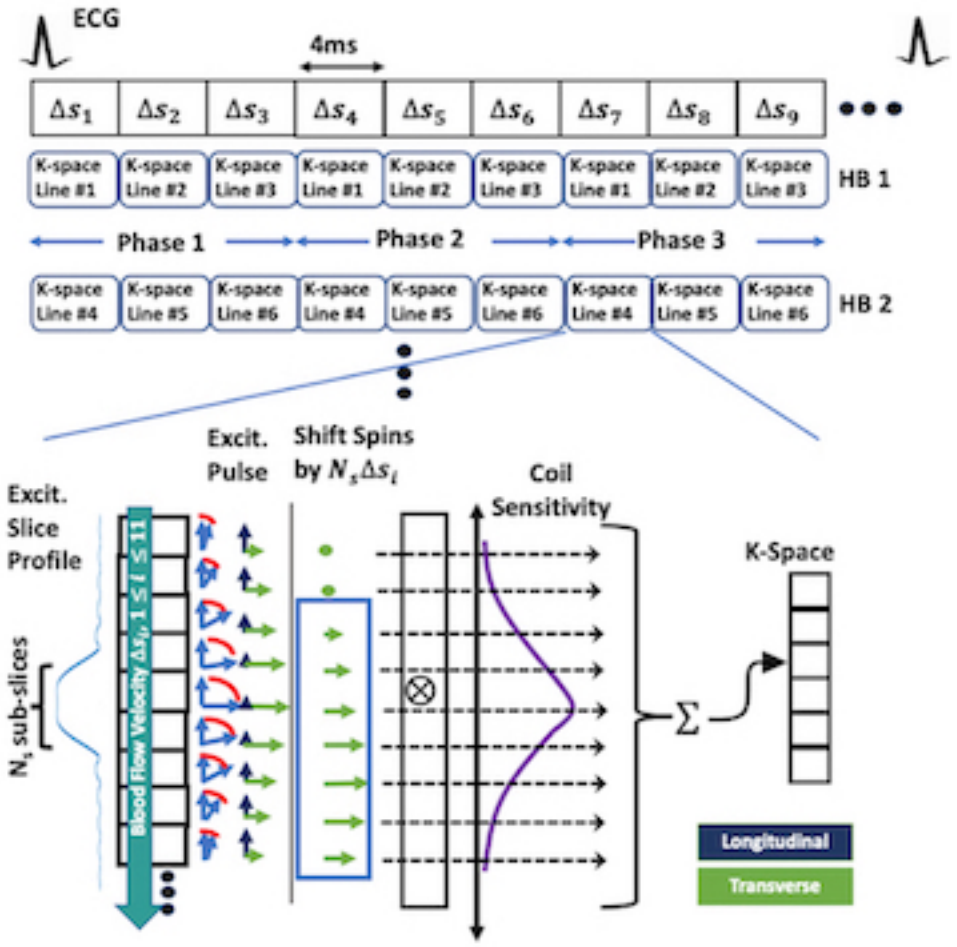


*Figure 4.3: A visual narration describing how our Bloch simulations were carried out. The entire k-space-segmented cardiac cine acquisition was simulated along with the time-varying through-plane blood flow –indicated by the fractional spin-replacement rate for each TR (4ms),$\Delta s$ –and the time-varying B1 excitation (described in 4.3.1 ). The $\Delta s$ pulsatile flow waveform used during the cardiac cycle is illustrated in Figure 4.4 and the B1 excitation for each repetition had a linear $\pi$ rad/TR phase ramp, as is standard in bSSFP acquisitions. The steps involved in simulating the acquisition of each k-space line is shown in the bottom of the figure. After each excitation, the spins are shifted downstream by $N_s\Delta s_i$, with i being the excitation's index, to simulate the through-plane blood flow. At mid TR, after the appropriate T2-decay, T1-recovery, and rotations from off-resonances and slice-encoding gradients, the spins' transverse magnetizations were weighted by a spatial Gaussian coil-sensitivity function in a sum to fill the appropriate k-space element. The appropriate T2-decay, T1-recovery, remaining off-resonant rotating, and gradient refocusing were done before the start of the next excitation. The Gaussian weighting was included to mimic a reception coil's spatial sensitivity, artificially removing some out of slice signal that's further away from the slice, as in the clinical case when using localized phase-array coils. HB: heartbeat. We published this in [3]*

stream amount, having $N_s + N_{os} = 6000$ total subslices with the target slice positioned at the array's center. The simulated spins were exposed to an $800\mu$ s sinc-functioned RF-pulse designed for a 6-mm slice-thickness, a 60° nominal flip-angle, a 3 time-bandwidth-product (TBW), and an incremental $\pi$ rad/TR RF phase-ramp. The imperfect excitation profile was determined using a detailed Bloch simulation by dividing the sinc-pulse into $TP_{RF} = 120$ time-points. This excitation pulse was carried out on the array of spins, with each spin's motion being calculated during each of the pulse's $TP_{RF}$ timepoints.

The Bloch simulations investigated effects of a constant flowrate with $\Delta s$ ranging from 0 to 1, and pulsatile flow effects with the $\Delta s$ waveform displayed in Figure 4.4. For a six mm slice-thickness, $\Delta s$=1 corresponded to a 1500 mm/s velocity. This was chosen as our maximum flow velocity because it is amongst the fastest seen in the thoracic area [120].

To fill up the k-space along the slice-encoding/select direction, $k_{se}$, an excitation was dedicated to each of the $N_{SE}$ k-space "lines" after $N_{Prep}$ equilibrium-preparation excitations. $N_{Prep}$ was arbitrarily chosen to be 300 for the stationary spin, and 1000 for the pulsatile case. This led to four total cycles ("heartbeats") for preparation before an acquisition for the pulsatile-flow Bloch simulation. The acquisitions were done at TE = TR/2. Each ensemble's phase accumulation along the slice-encoding axis, $\vec{r}_s$, included the slice-encoding gradient lobe's induced dephasing and the ensemble's inherent off-resonance. Based off of equation 2.22, this phase accumulation is:

$$\theta_{SE,T_E} = 2\pi\vec{k}_{SE,T_E} \cdot \vec{r}_s + \Delta\phi_{Off,T_E} \tag{4.4}$$

where $k_{SE}$ and $\Delta\phi_{Off,T_E}$ are the slice-encoding's k-space coordinate and the off-resonance phase accumulation by TE, respectively. Each k-space element would be the complex sum of all spin-ensembles, weighted by a Gaussian receiver-sensitivity function [68] that had a 10mm standard deviation. This sensitivity function was included to mimic the effects local phased-array receivers have on an image's acquisition, where only transverse spins proximal

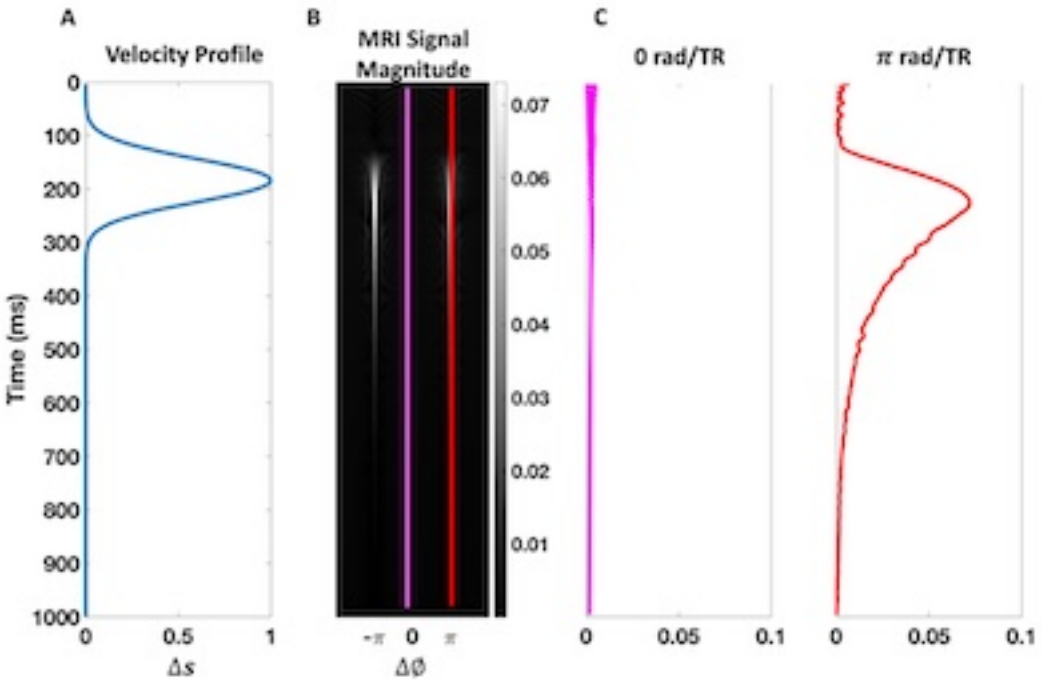


*Figure 4.4: Pulsatile flow Bloch simulation results. (A) The simulated velocity profile is given in terms of the fractional spin-replacement rate, $\Delta s$, as a function of time. (B) The simulated MRI signal magnitude for the range of off-resonances $\frac{\Delta\phi}{TR}\epsilon[-2\pi, 2\pi]]$. (C) The simulated MRI signal magnitude for the isochromats with 0 and $\pi$ rad/TR off-resonance frequencies, indicated by the pink and red colors, respectively, are plotted on the right. Just as Markl et al discussed [72], coherent signal enhancement is most pronounced for $\pi$ rad/TR isochromats, shortly after peak-systolic speeds. We published this in [3]*

to the coils make significant contributions to the k-space readouts. The rest of the $T_R$ would be completed with the slice-encode refocusing lobe to balance the gradients before the next excitation, remaining off-resonant rotation, and the remaining T2-decay and T1-recovery.

The Bloch simulation's acquisition scheme worked with a temporal resolution defined as $T_{Res} = V_{PS}T_R$, with $V_{PS}$ being the views per segment (VPS). For a given acquisition time, $T_{Acq}$, the number of frames acquired was $N_F = \frac{T_{Acq}}{T_{Res}}$ . Single $V_{PS}$ experiments were done with one, eight, and twenty-four encoding steps for a theoretical proof of concept of the sequence.

When investigating pulsatile flow effects, it was important to make sure that there was no outflow aliasing corrupting the nominal slice's signal. In order to achieve this, we slice-encoded for a large enough through-slice FOV such that outflow-induced aliasing would not be an issue. As such, we worked with twenty-four encoding steps because it has multiple factors to evenly segment the acquisition. Three simulated acquisitions were carried out with one, eight, and twenty-four VPS to investigate the pulsatility effects on the proposed sequence as the VPS was increased. All published simulation results were carried out for the $\pi$ rad/TR isochromats.

### 4.3.2 Phantom Experiments

Flow-phantom measurements were performed on a 3 T scanner (Prisma; Siemens Medical Solutions, Erlangen, Germany) using a birdcage head-coil. bSSFP was performed with a 6-mm slice thickness, $330 \times 196\text{mm}^2$ FOV, 256 x 146 in plane samples, 977 Hz/pixel readout bandwidth, 3.61 ms TR, and a sixty-degree nominal flip angle. The scans used linear top-to-bottom k-space increments. A custom rotary pump pushed tap water through the tubing. This pump had a time-averaged constant velocity of approximately 36 cm/s, but because of the pump's frequency, the fluid behavior was similar to rapid pulses. The FOV was positioned so that it would intersect perpendicularly with the tube's ascending and descending directions. No gating was done in order to see the proposed sequence's

capability in limiting the zipper artifacts. To investigate slice-encoding's effectiveness, images were acquired with twenty-three, fifteen, ten, five, and three slice-encoding steps and were compared with the 2D bSSFP image. This respectively left us with the following scan times: 12.1s, 7.9, 5.3, 2.6, and 1.6 seconds.

An additional scan was done with a faster pump in order to evaluate how the sequence performs for near-peak systolic velocities observable in patients. This pump's velocity profile was less pulsatile than the custom rotary pump and it generated an approximate velocity of 140 cm/s. We compared the standard scan with five, ten, fifteen, and twenty slice-encoding steps. All other scan parameters were the same as the previous phantom's scan.

### 4.3.3 Human Studies

Nineteen healthy volunteers were scanned on a 3T system (Prisma; Siemens Medical Solutions, Erlangen, German) using cardiac chest and spine coils. The healthy volunteers, whose ages ranged from 23-35 years, were asked to hold their breath for two TrueFISP cardiac-gated cine evaluations: one 2D bSSFP acquisition and the other being our proposed technique, using six slice-encoding steps. Horizontal long axis (HLA) and short axis (SA) views were selected as they have known vulnerabilities to outflowing signal in bSSFP imaging [73, 30]. The imaging plane had a six-millimeter nominal slice thickness with a $256 \times 184$ in-plane acquisition matrix, $1.4 \times 1.4\text{mm}^2$ in plane resolution, fifty-degree flip angle, 977 Hz/pixel readout bandwidth, and TE/TR of 1.805/3.61 ms. With 2X GRAPPA, 6/8 partial-Fourier, and 16 views per segment, scans were achieved in under about a twenty-two second breath-hold for the slice-encoded acquisition and in about 3.66 seconds for the 2D sequence. An additional 2D scan with six averages, which shared the same duration as the slice-encoded experiment, was done on one volunteer to see what impact the averaging effect provided by the added slice-encoding steps had on the resulting image.

#### 4.3.3.1 Statistical Analysis

Nineteen 2D and slice-encoded cine pairs were randomly selected to have their quality assessed by an expert radiologist–who had more than eight years of experience–for two statistical evaluations. She first performed a rank comparison test, where she compared each pair in a blinded fashion to deem if one had a superior quality over the other, or if they simply showed "no visual difference." In the second evaluation, she graded each individual cine's quality on a scale from 1 to 5 with the following criteria: 1: poor image quality; flow artifact obscures cardiac structures and distant structures such as chest wall structures. 2: fair image quality; artifact from vessel flowing perpendicular to the plane of the image obscures cardiac structures adjacent to the vessel without extending to the chest wall. 3: mild obscuration of cardiac structures intimate and adjacent to the vessel flowing perpendicular to the image. 4: minimal obscuration of cardiac structures intimate to the vessel flowing perpendicular to the plane of the image. 5: no obscuration of cardiac structures by flow perpendicular to the plane of the image. These image-quality scores were used for a nonparametric-paired evaluation, a Mann-Whitney Test for independent samples, to answer if there was any statistical difference between the slice-encoded and the 2D bSSFP cines. The two-sided evaluation was done for $\alpha = 0.05$ for significance.

## 4.4 Results

### 4.4.1 Bloch Simulations

Figure 4.4 shows pulsatile flow Bloch simulation's results, using the plotted velocity-waveform. The results confirm Markl et al's labeled "frequency offset-dependent outflow effects", with the $\pi$ rad/TR isochromats contributing the most to the OOS signal [72]. This out of slice contribution and variable in-flow have signal-reception related consequences, as shown in Figure 4.5's Bloch simulated cine acquisition scheme. This figure displays the simulated signal of an array of spins with $\pi$ rad/TR off-resonance, using the velocity profile shown in Figure 4.4A.

Figure 4.5A shows the transverse magnetization's spatial profile at the simulation's peak systolic velocity for the $\pi$ rad/TR spins, for space within and out of the intended imaging slice. The simulated slice-encoded acquisition results, for a single VPS, are shown in Figure 4.5B which displays the peak systolic frames for one, eight, and twenty-four slice-encoding steps. With one slice-encode (i.e., 2D imaging), the out-of-slice signal shown in Figure 4.5A are aliased into the imaging slice, corrupting the signal profile within the intended slice. Figure 4.5B's in-slice profile becomes more similar to Figure 4.5A's as the number of slice-encoding steps increases, because the out-of-slice contributions are better localized. Figure 4.5C displays the spatial profile at peak systolic velocity for a simulated acquisition with 24 slice-encodes for one, eight, and twenty-four VPS. The pulsatile spin inflow adds bulk signal variability for adjacent k-space lines, impacting the spins' localization. With 24 VPS (single shot), the spins are smeared (or "zippered") along the slice's axis, impacting the in-slice signal. The intended slice's profile becomes more similar to Figure 4.5A's as the temporal resolution increases to a single VPS, because the amount through-slice zippering is heavily reduced.

### 4.4.2 Phantom Experiments

The custom rotary phantom results are displayed in Figure 4.6. Figure 4.6A compares the standard 2D bSSFP image to the three, five, ten, and twenty-three slice-encoded images. This motor's noticeable pulsatility made the acquisition prone to substantial in-flow variability in the time between adjacent k-space readouts, causing visible zippers in the one, three, and five slice-encoded experiments (green arrow). Another clinically common outflow artifact seen in the 2D bSSFP scan is the spatial mis-registration along the readout's direction (orange arrow), which is expectedly reduced with increasing slice-encoding steps. By ten slice-encoding steps, both of the artifacts are barely noticeable in the target slice and are eliminated from the twenty-three slice-encoded experiment's center slice (white arrows). To get a sense of the outflowing signal's extent, selected slices from the twenty-three slice-

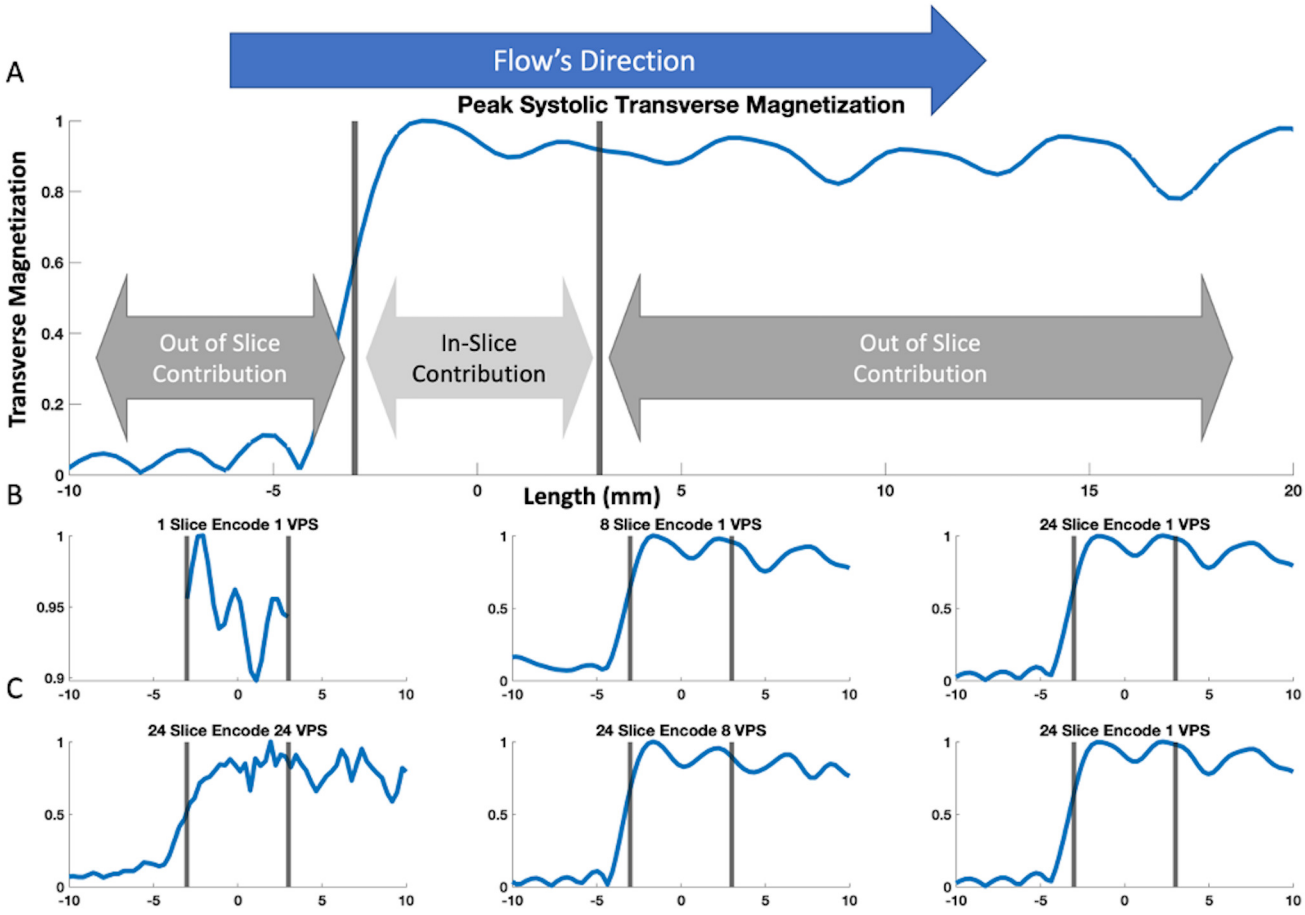


*Figure 4.5: Bloch-simulated transverse signal magnitude of the pulsatile spin movement. The nominal slice is indicated by the grey bars. (A) shows the ground truth transverse magnetization's spatial distribution at peak systole (see Figure 4.4). The figure is zoomed in to -10 to 20 mm from isocenter. There is minimal signal upstream of the slice, whereas downstream out-of-slice spins contribute substantial signal hundreds of mm distal from the nominal imaging slice. Parts (B) and (C) show the signal's spatial distribution according to the simulated acquisition outlined in Figure 4.3 using various combinations of the number of slice-encodes and views-per-segment (VPS). Part (B) shows single VPS results with one, eight, and twenty-four slice-encoding steps. Notice how the transverse signal profile is more properly resolved with increasing encoding steps; whereas using one slice-encode (i.e., conventional bSSFP) resulted in an aliased and corrupted signal profile. The simulation results using eight and twenty-four slice encodes in this example generated within-imaging-slice signal profiles similar to the ground truth in A. Part (C) shows twenty-four slice-encoding results for one, eight, and twenty-four VPS. The time-varying velocity adds an additional signal sum variability between adjacently acquired k-space segments, resulting in a the "zipper" phenomenon discussed by Schar et al [95]. In this example, simulations with eight and one VPS can properly resolve the within-imaging-slice signal profile, while twenty-four VPS resulted in a corrupted in-slice signal profile. We published this in [3]*

encoded experiment are shown in Figure 4.6B, with the thirteenth being the center partition. The complex sum of all non-center slices (bottom right) properly showed all of the artifacts. In addition to seeing how the readout mis-projections are localized outside of the slice, Figure 4.6B shows that the sequence's through-slice encoding scheme opens another avenue for the artifacts to "zipper" through.

Figure 4.7A displays flow phantom results with a faster flow velocity of 140cm/s. The readout mis-projection is the dominant artifact seen in these experiments (orange arrow), which is significantly reduced as the number of slice-encoding steps increases. Figure 4.7B displays images from selected outer partitions and the absolute value of all non-center partition's sum from a scan with 20 slice-encoding steps.

### 4.4.3 In Vivo Experiments

Figure 4.8A displays three columns comparing slice-encoded (top) and 2D (middle) peak-systolic images from three volunteers, each displaying a particular common outflow artifact that was reduced in the corresponding slice-encoded image. The third row displays the absolute value of the complex sum of all non-center slices. Each image-set was normalized and adjusted to the same level and window-width. The middle row shows the two commonly seen outflow-related artifacts in bSSFP imaging that Schar et al discussed [95]: "out of plane coherence artifacts" (red arrow) and the "through-plane flow transient artifacts" (green arrows). These both hamper the blood-myocardium contrast and reduce myocardial visualization. The coherence artifacts contribute to a readout mis-projection or as signal pileups, as shown in columns II and III respectively. Column I's 2D image shows a heart's SA view with a green arrow pointing to a zipper. The corresponding slice-encoded image has the zipper significantly reduced and it better demonstrates the endocardial border of the left ventricular septum. The third row shows that the zipper was mostly captured through the outer slices. Column II's 2D scan shows what appears to be some "false-anatomy", indicated by the red arrow, which is properly eliminated in its slice-encoded scan. It is evident that

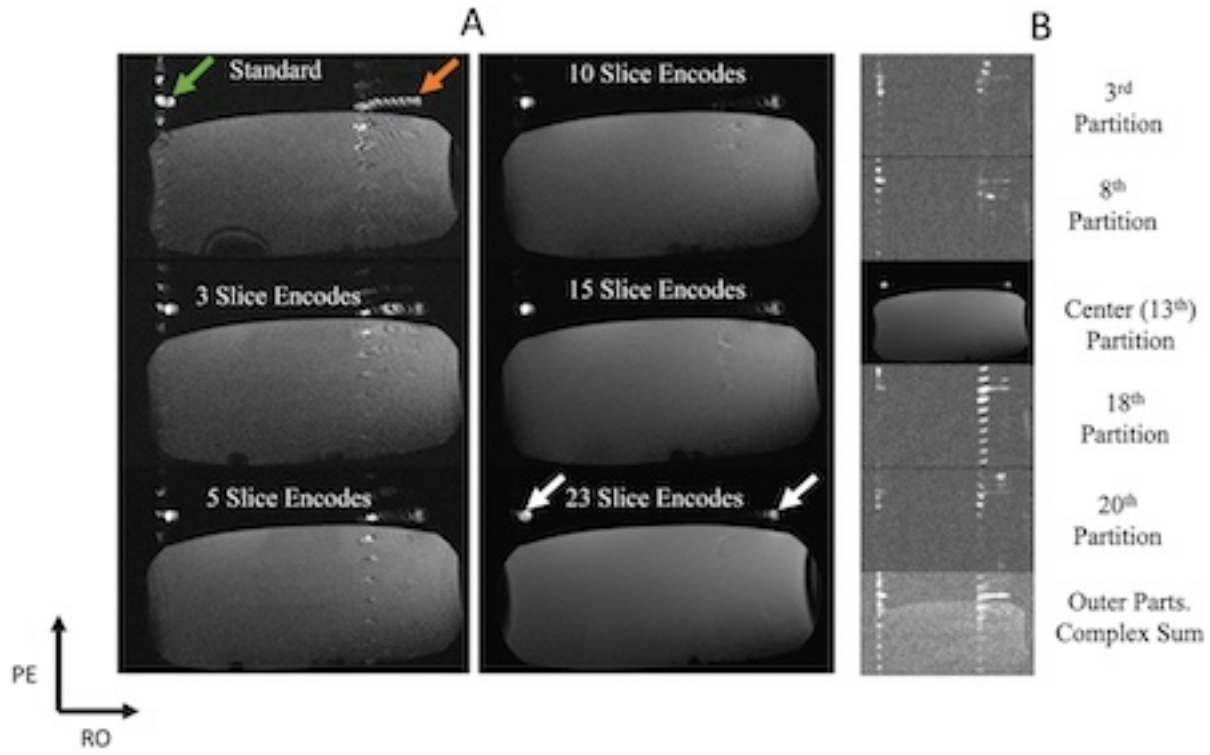


*Figure 4.6: A pulsatile flow phantom experiment, with a speed that averaged at 36 cm/s. The two tube cross-sections are of the same hose, with one flowing into and the other flowing out of the plane. The stationary phantom was placed to help load the coil. (A) Results that compare the 2D bSSFP scan image to the center slice of the slice-encoding approach with three, five, ten, fifteen, and twenty-three encoding steps, respectively. The 2D acquisition shows pulsatile zippers (green arrow) and a readout mis-projection (orange arrow). Both of these artifacts are reduced with increasing number of slice-encoding steps (white arrows). (B) Selected slices of the twenty-three-slice-encoding experiment. The bottom image is the complex sum of all signals from all non-center slices. It can be seen that the zipper is smeared along the through-slice axis and the mis-projection is localized in the non-center slices, limiting their extent in the center image. We published this in [3]*

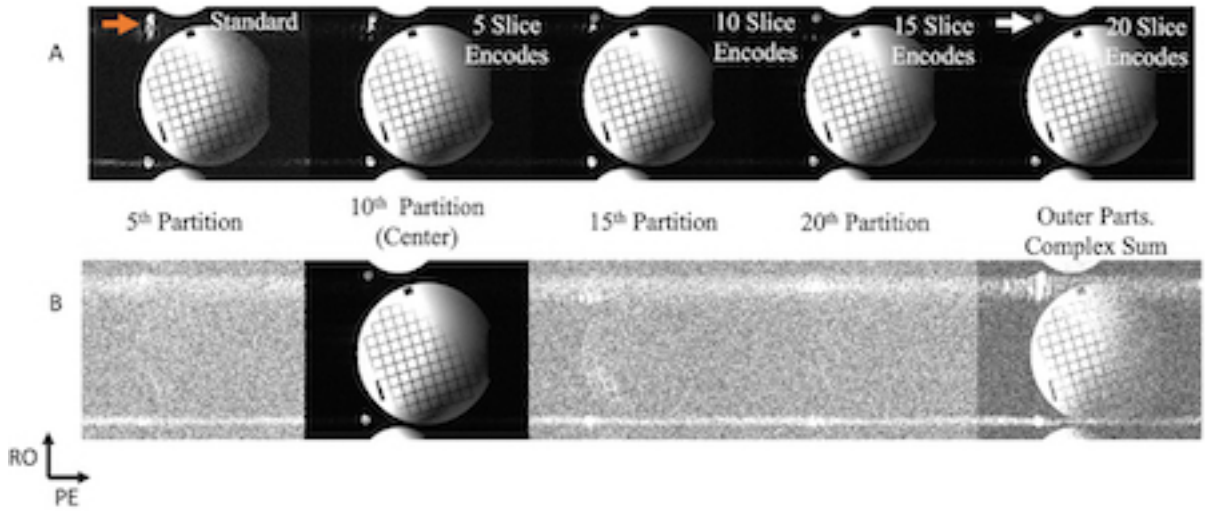


*Figure 4.7: A phantom experiment was done to evaluate the sequence's performance with constant flow, with its velocity running at a speed of approximately 140 cm/s. Just as in Figure 5's setup, the two tubes' cross-sections are of the same hose, and the stationary phantom was used to load the coil. (A) A flow corrupted 2D bSSFP comparison with five, ten, fifteen, and twenty slice-encoding steps. The out of slice coherent sum mis-projected during the readout (orange arrow) is the main artifact seen in this experiment's 2D acquisition (with some minor pulsatile phase-encoded zippers), which is significantly reduced with increasing slice-encoding steps (white arrow). (B) Selected slices of the twenty slice-encoded experiment, with the right furthest image being the complex sum of all non-center slices. This complex sum image shows how a significant portion of the readout's mis-projection was localized in the non-center slices, relieving that artifact from the center image. We published this in [3]*

this is false anatomy as this is preserved in the out of slice's complex sum. Column III shows two severe outflow-related artifacts. The first, marked with a green arrow, is a misregistered signal between the aorta and the para-aortic fat, caused by the zipper. A red arrow points to an apparent wave-like, outflow-enhanced blurring centered within the right atrium, obscuring evaluation of the interatrial septum and tricuspid valve. These are complicated outflow artifacts, but their impacts are all substantially reduced in the slice-encoded image. The out of slice complex sum's row shows how these artifacts are localized in the outer slices.

Figure 4.8B shows the outer-slice's images from Figure 4.8A's third column. The fourth partition is the center, with the higher slices being downstream and the lower three being upstream. Some of the flow wraps around, however the upstream slices protect the center partition from the aliased signal. Most of the descending aorta's corruption in the 2D acquisition was captured in the two downstream slices and the corruption originally around the right atrium was mostly captured in the upstream slices.

To see how this technique performs in cine imaging, the previous example's first eight of fifteen cardiac phases are displayed in Figure 4.9. The outflow artifacts are obviously cardiac-phase dependent, and only have moderate myocardial-wall definition after the fifth frame. On the contrary, the corresponding slice-encoded images show clear septal, lateral-wall, and left-ventricular apex definition with minor variations through each frame.

The proposed technique with six slice-encoding steps was compared to the 2D technique averaged six times in a comparison to see what impact the technique's inherent averaging had on the outflowing signal's presence in the resulting image. Figure 4.10 shows their comparison along with the 2D technique, convincing that simple averaging does not reduce the flow artifacts.

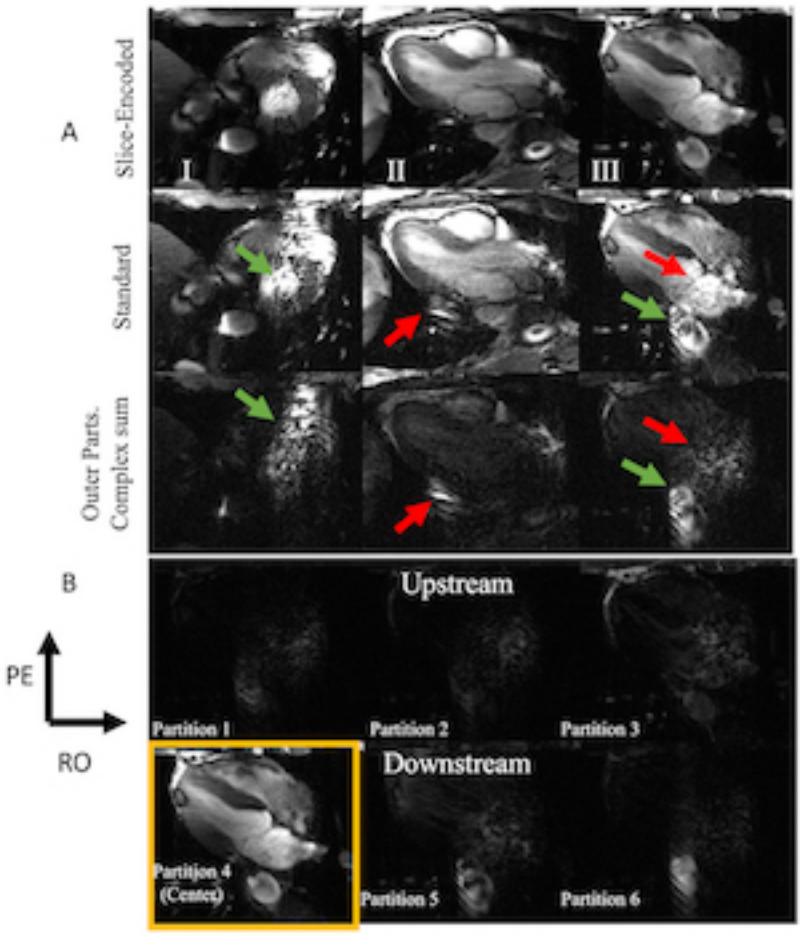


*Figure 4.8: (A) Peak systolic image comparison between three six slice-encoded experiments (top) and their corresponding 2D bSSFP scan (middle). The bottom row of 4.8A is the image of the non-center slices' complex sum. The slice-encoded image shows significant reduction in outflow artifact across short axis, vertical long axis, and horizontal long axis imaging. Green arrows point to Schar et al's "through-plane flow transient artifacts" ("zippers") and the red arrows point to the coherent sum outflow artifacts [19], resulting in readout mis-projections. (B) All of panel III's image partitions. Partitions five and six capture the downstream slices. Notice how partitions five and six capture much of the 2D acquisition's artifacts. We published this in [3]*

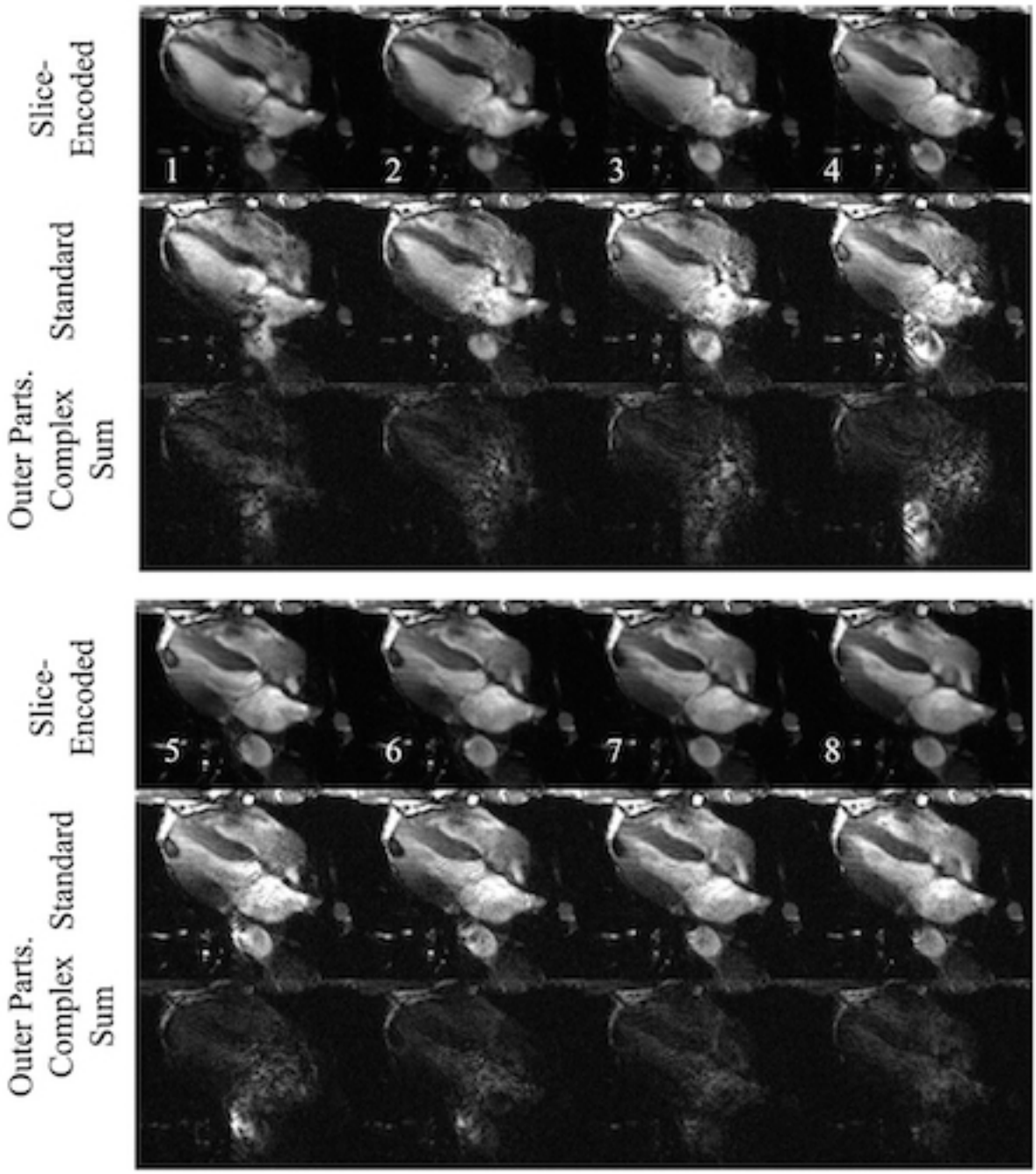


*Figure 4.9: The first eight out of fifteen cardiac phases of Figure* **??** *III's acquisition. The proposed sequence produces cine results with fewer outflow disturbance. Much of the 2D acquisitions' artifacts are captured in the outer partitions. We published this in [3]*

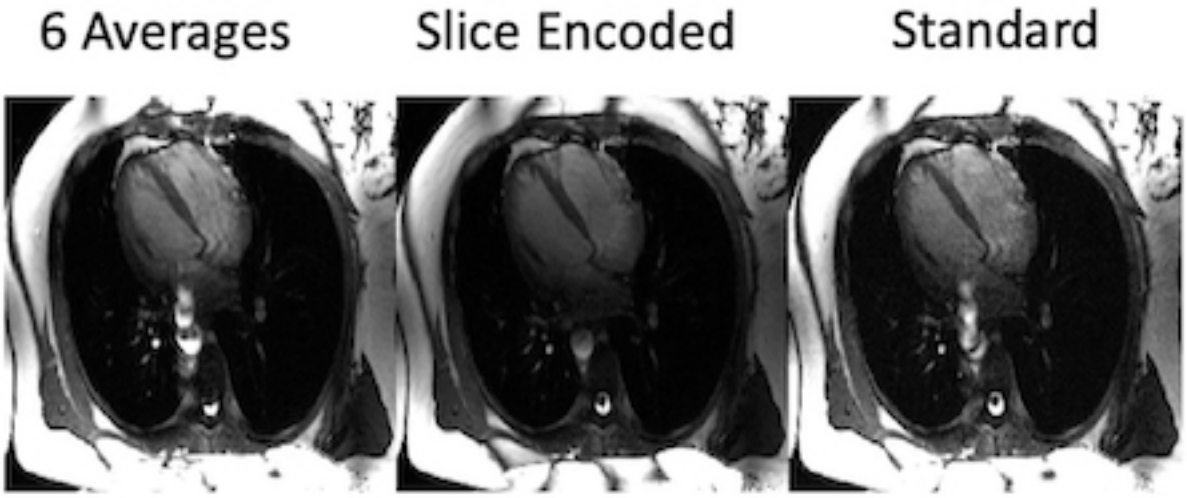


*Figure 4.10: Comparisons between the 2D acquisition with six averages, six slice-encoding steps, and the 2D bSSFP sequence. Minimal changes between the added averages and the 2D technique shows that the feature of the slice-encoding sequence reducing the artifact's extent is a result of the outflow's localization instead of signal-averaging. We published this in [3]*

#### 4.4.3.1 In Vivo Experiments: Statistical Analysis

The rank comparison test indicated that all of the slice-encoded images had quality superior to the 2D method. Despite the prolonged breath-hold, we did not observe any added issues, most likely because we scanned middle-aged, healthy subjects.

The nonparametric test involved the quality-score distribution of the 2D bSSFP and of the slice-encoded cines, with a null hypothesis that the two cine populations had the same score distribution. The test came to a 0.01 significance, suggesting to reject the null hypothesis. The reassurance from the rank-comparison test made it clear that the slice-encoded images provided a superior image quality than the 2D bSSFP cines.

## 4.5 Discussion

In this study, we sought to reduce flow artifacts in cardiac cine imaging by introducing slice-encoding steps in order to spatially localize the outflowing spins. As excited spins leave the slice, the signal profile no longer spans a 2D space, spreading over a 3D volume. Instead of having a planar data set we resolve up to an effective 3D FOV along the slice-select's direction with the anticipated slice positioned at the center. This treatment is similar to a 3D acquisition, but without any change to the 2D excitation profile.

This technique was greatly inspired by Lu et al's SEMAC sequence [65] as well as Glover et al's 3D z-Shim method [39], which were proposed to resolve through-plane metal-induced field inhomogeneities. The SEMAC technique uses the slice-encoding technique to correctly encode 2D excitation slices that are distorted in the slice-select direction by metallic objects. In our case, the 2D excitation's slice profile is not necessarily distorted; however, the same strategy is effective in reducing or eliminating image artifacts caused by OOS signal that persist throughout successive TR's, such as from outflowing spins.

Our Bloch simulations established a theoretical basis of our proposed method effectively reducing much of the outflow-related artifacts by localizing the OOS spins, given a large enough encoding FOV. The phantom and the in vivo images show significant alleviation from the outflow-related artifacts.

The Bloch simulations showed that the sequence isn't immune to what causes the "zippers", however this artifact's significance is reduced with increasing temporal resolution. Fortunately, temporal resolution isn't the only avenue for reducing this artifact's occurrence. Encoding through the slice's axis allows the zipper-smearing to occur along that direction as well, reducing their extent on the center slice. This is evident with the in vivo scans of Figures 4.8, 4.9, and 4.10, all of whom had a 57.76 ms temporal resolution. Their OOS complex sum images show much of their zippers being localized in the outer slices.

Both, the Bloch simulations and the phantom experiments were done more for demonstrative purposes rather than for figuring proper scanning parameters. The Bloch simulations were done with an arbitrary pulsatile flow waveform and receiver coil sensitivity. The phantom experiments were done with tap water, whose T1 and T2 are much larger than blood's. To get a sense of the difference, consider cerebral spinal fluid, which is predominantly water. It has a 3T longitudinal recovery time of over 4s [26] and a T2 decay around 1.6s [106], while adult blood has T1 and T2 estimated at around 1-2 seconds and 150 ms respectively [64]. Therefore, one cannot make any inferences on the number of slice-encoding steps needed to resolve much of the outflowing signal from the intended image in the in vivo studies from these experiments. However, these studies did provide a useful proof of concept free of any external or unwanted variables, including limited breath-hold duration, motion, and susceptibility issues.

Our in vivo results proved the proposed method to be of promising use. The SA acquisition's zipper of Figure 4.8's column I disturbs much of the left ventricle and corrupts anatomical detail of the septum and right ventricular lumen. In a clinical sense, myocardial contraction, and therefore blood ejection is greatest at peak systole, and the heart's SA view is often used for determining ejection fraction. Clear delineation of the endocardial and epicardial contours is critical for accurate volumetric and mass quantification. Artifacts like these would impose a barrier for such an evaluation, especially for young-adult subjects. Overall, the slice-encoded images benefit from improved visualization of the interatrial septum, tricuspid valve, descending aorta and para-aortic soft tissues.

An argument could be made in favor of 3D-bSSFP imaging with the same slice-thickness and number of slice-encoding steps as a means to resolve the outflowing signal from the slice of interest. However, 3D through-slice imaging is known to result in a reduced blood-myocardium contrast due to reduced fresh blood enhancement that 2D cardiac cine imaging typically relies on [82, 61]. Another reason for the reduced blood-myocardium contrast in 3D

cine bSSFP imaging is because blood-signal of various spin histories mixes in the acquisition [74, 81]. Our technique preserves the blood-myocardium contrast of 2D cardiac cine imaging while removing the outflowing signal artifacts.

We chose to work with six encoding-steps in our in vivo experiments thanks to our Bloch simulations' results (Figure 4.5). This choice was made knowing that our simulation took account for a 1500 mm/s peak systolic velocity that is typically seen in healthy young adults [120] recruited in our study. If this were to be used in the clinical case, the number of necessary encoding steps would need to be adjusted based on the approximate flow velocity of each patient. If the flow velocity is expected to be substantially lower than 1500 mm/s, then reducing the number of slice-encoding steps would result in significant acquisition time savings.

Our results from Figure 4.10 indicate that no averaging effects are assisting the removal of outflow artifacts. However, all three of the experiments were done with a 57 ms temporal resolution, which provides ample opportunity for pulsatile through-plane flow transient artifacts. A 2D cine acquisition with six-times higher temporal resolution may reduce the extent of the transient artifacts, as indicated by Figure 4.5C, however will not be immune to the coherent out-of-slice sum projecting onto the image.

Regarding the three "ingredients" to outflow artifacts, the proposed sequence localizes the artifacts from the outflowing signal, thereby reducing the extent of readout mis-projections and signal pileups in the intended slice. The added slice-encodes provides an additional dimension for pulsatile-induced zippers to smear along, also reducing their extent in the intended image.

Using our proposed technique, scan time will be longer due to the slice-encoding steps. In this work, our goal was to demonstrate the technique using relatively conservative acceleration rates. Further developments to accelerate the scan are clearly warranted. Because this

involves encoding in three directions, one could exploit a radial means of undersampling and spread the incoherence in the transform domain into three dimensions [66]. There has been work in a similar domain, using 3D radial bSSFP for whole heart coronary imaging [109] that is compatible with our slice-encoded 2D method. This application of the undersampling technique is intriguing for two reasons - not only could this serve as a potential means of reducing the scan time, but it could do so with an expanded effective through-slice FOV, further minimizing aliasing effects.

## 4.6 Conclusion

We propose a slice-encoding technique for 2D bSSFP cardiac cine imaging to effectively reduce or eliminate several types of commonly seen flow-dependent artifacts. The types of flow-related artifacts are not seen on every clinical case at our center, but occur with enough frequency, particularly in younger patients, and at higher field imaging, to warrant development of a pulse sequence to correct for these artifacts. Therefore, our technique would be a useful supplemental technique for patients whose blood flow results in artifacts on 2D cardiac cine images.

# CHAPTER 5

# Unfolding Coil Localized Errors from an imperfect slice profile using a Structured cAlibration Matrix (UNCLE SAM): An Application to outflow effects in cine bSSFP Imaging

## 5.1 Introduction

As discussed in the previous chapter, 2D bSSFP imaging is core to cardiac MR, but is vulnerable to excited outflowing spins from being misprojected onto the target slice. By applying slice-encoding steps to encode for a FOV beyond the target slice, we were able to unfold the outflowing spins from the target slice, guaranteeing that the artifact spans a volumetric signal profile. This is summarized in 5.1. Unfortunately, its prolonged duration makes it unlikely to be used for patients with severe outflow effects or to be integrated with research sequences, such as MOLLI [76]. A means of reducing the extent of outflow signal corruption from the target slice without too much of an increase in scan time would be beneficial for subjects with severe outflow effects. Because the outflowing spins are away from the target slice, there could conceivably be enough localized coil sensitivity to use parallel imaging methods to unfold them from the image.

Working to unfold these outflowing spins from the target slice without explicitly slice-encoding makes the problem in the signal profile similar to the problem faced in simultaneous

multi-slice (SMS) imaging. In this sub-field of magnetic resonance imaging, slices are excited *simultaneously*, with each slice excitation phase having a different RF phase-ramp per phase-encoding step, shifting the FOV of each slice by a different amount [40]. This required spatially encoding for a larger in-plane FOV along the phase-encoding direction. As parallel MR imaging methods developed, the nominal FOV of slice was prescribed, resulting in the slices to add onto each other [14, 15]. Shifting the FOV of simultaneously acquired slices is called "controlled aliasing in parallel imaging" (CAIPI), and is beneficial because it causes overlap of slice regions with different channel sensitivity profiles [14]. The slices can then be unfolded by traditional parallel imaging means, i.e. SENSE [90] or GRAPPA [43], given the sensitivity profile of each slice.

For the case of outflow effects, we excite a single slice, and signal is leaking into the adjacent downstream slices, not making it feasible to achieve CAIPI conditions. An alternative family of approaches that does not require CAIPI are based off of the "slice-GRAPPA" concept [99, 25]. Specifically, slice-GRAPPA fits the k-space entries of the superimposed slice to the k-space entries of the individual slice calibration data. Because the fitting is done from k-space of the collapsed slices to the k-space of individual slices, this type of fitting is not working to estimate the spatial harmonics of missing k-space lines. Rather, this fitting determines the weights needed to cancel the signal of all other slices, keeping only the target slice. This approach works well — even without FOV shifts — for discretely positioned slices, but destructive interference begins to impact the target slice for for cases if other slices are adjacently spaced which is the case for outflowing spins.

In this chapter, we propose a means of unfolding the outflowing spins from the target slice using the localized coil sensitivity difference between the target slice and outflowing spins titled Unfolding Coil Localized Errors from an imperfect slice profile using a Structured cAlibration Matrix (UNCLE SAM). Rather than explicitly slice-encoding for the duration of the acquisition, we acquire a 2D acquisition with a separate slice-encoded calibration

scan in the same breath-hold. By regarding the acquired 2D data as the center partition of a volumetric k-space having $N_{SE}$ partitions, the non-center partitions are imposed to be linearly consistent with a subspace defining the linear relationship of the local k-space neighbors of the slice-encoded calibration. This means we use the slice-encoded calibration to help use estimate the non-center k-space partitions needed for one to unfold most outflowing spins from the target slice. This approach of unfolding out of slice signal from the target slice was inspired by the following low rank parallel imaging based methods: PRUNO [129], SAKE [100], and LORAKS [48, 46, 47, 49].

## 5.2 Theory

In this section, we will briefly recap outflow artifacts and review the foundation behind low rank modeling of local k-space neighborhoods before detailing our proposed reconstruction scheme.

The 2D acquisition of a specific channel, $j$, in a setting of outflowing, through-plane spins can be described as the following:

$$\begin{aligned} S_j(k_{ro}, k_{pey}) &= \iiint C_j(r_{ro}, r_{pey}, r_s) M_\perp(r_{ro}, r_{pey}, r_s) e^{-i2\pi\cdot(k_{ro}r_{ro}+k_{pey}r_{pey})} dr_{ro} dr_{pey} dr_s \\ &= \int C_j(\vec{r}) \cdot M_\perp(\vec{r}) e^{-i2\pi(\vec{k}_{ro}+\vec{k}_{pey})\cdot\vec{r}} d\vec{r} \end{aligned} \tag{5.1}$$

Because a 2D acquisition only acquires the $k_{se} = 0$ partition, the gradient encoding scheme described in Equation does nothing to distinguish in-slice spins from outflowing spins, ultimately leaving the outflowing spins projected — or aliased — onto the imaged slice. To avoid the time-penalty from slice-encoding, we sought to take advantage of the coil sensitivity profiles to spatially unfold the out of slice spins. As discussed in chapter 2.6.3.2, an entry of multi-channel k-space is linearly dependent on all of its neighbors across all channels:

$$S_j(\vec{k}_l) = \sum_{c}^{N_c} \sum_{b}^{N_b} n_c^j(b) S_c(\vec{k}_{l,b} \tag{5.2}$$

where equation 5.2 is generalization of equation 2.43. Here, $\vec{k}_{l,b}$ refers to the neighbors surrounding k-space coordinate $\vec{k}_l$, and $n_c^j(b)$ is the weight of k-space neighbor $b$ from channel $c$. In this scenario, the kernel defining the k-space neighborhood has $N_b+1$ k-space members, whose width along the $k_{ro}$, $k_{pey}$, and $k_{se}$ directions are $w_{ro}$, $w_{pey}$, and $w_{se}$ respectively, such that $w_{ro} \cdot w_{pey} \cdot w_{se} = N_b + 1$. According to equation 5.2, sliding the kernel through the multi-channel k-space and vectorizing its entries each position to be their own row of a data matrix, $\mathbf{A}$, will result in linearly dependent columns of that matrix [100]. Furthermore, constructing $\mathbf{A}$ from a sliding kernel will result in repeated k-space entries, giving it block Hankel structure [100]. The "forward" operation going from the multi-channel k-space to the structured data matrix will be denoted as $H_F$. For any set of multi-channel k-space, $\mathbf{x}$, $\mathbf{A} = \mathrm{H}_F(\mathbf{x})$.

For a kernel staying within the bounds of a k-space matrix of size $N_{ro} \times N_{pey} \times N_{SE} \times N_c$, the dimensions of the resulting $\mathbf{A}$ matrix will be $(N_{ro} - w_{kro} + 1)(N_{pey} - w_{kpey} + 1)(N_{SE} - w_{ks} + 1) \times (N_b + 1)N_c$. Moving the terms of Equation 2 to the same side would result in a net zero weighted sum of all multi-channel k-space elements in the neighborhood with $-1$ being the target entry's $(S_j(k_l))$ weight. Arranging these weights as a vector just as how the kernel entries were vectorized when constructing a row of $\mathbf{A}$ would give a vector $\vec{v}_\perp$ such that:

$$\mathbf{A}\vec{v}_\perp = 0 \tag{5.3}$$

This implies that the row space of $\mathbf{A}$ is low rank [24-32] and has a null space $\mathbf{V}_\perp$ such that:

$$\mathbf{A}\mathbf{V}_\perp = 0 \tag{5.4}$$

where each column vector of $\mathbf{V}_\perp$ has length $(N_b + 1)N_c$. This null space defines linear

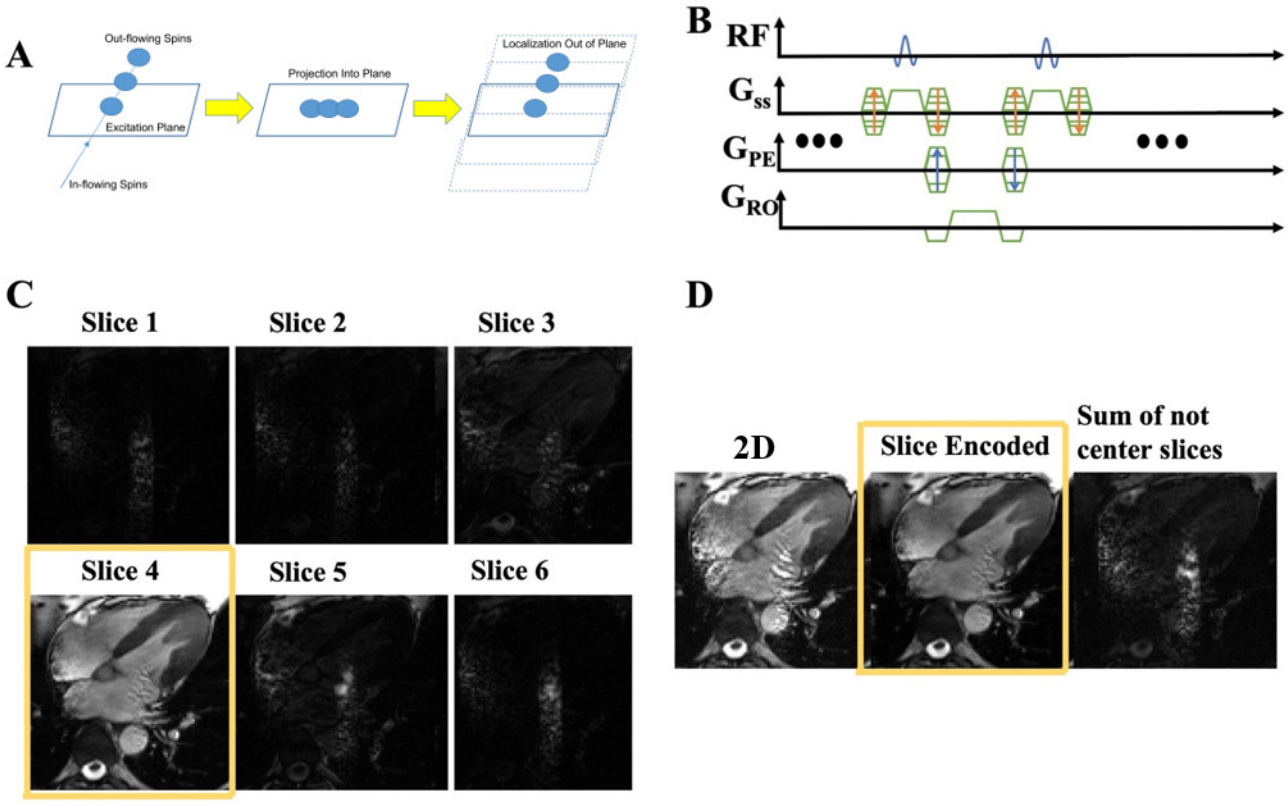


*Figure 5.1: (A) An illustration of the outflow effect problem in bSSFP imaging. Blood flow going through the target slice carries excited spins downstream, ultimately being projected onto the intended image. The pulse sequence in (B) uses $G_{ss}$ phase encodes for a volume beyond the slice to localize the outflowing spins, without any change to the 2D excitation. (C) shows all slice-encoded partitions of an example that otherwise would have had outflow artifacts, with center slice — number 4 — showing the target slice unfolded from these effects. The 2D example with flow artifacts is shown in (D) and is compared against the slice encoded example from (C) and the magnitude of the complex sum of all but the center slice. The artifact in the image can be seen captured in the outer slices.*

dependence of multi-channel k-space entries within the neighborhood defined by the kernel used to construct $\mathbf{A}$. This subspace can be determined from a calibration matrix, $\mathbf{A}^{\text{cal}}$, that is constructed from a fully sampled low resolution calibration k-space, $\mathbf{x}_{\text{cal}}$, such that $\mathbf{A}^{\text{cal}} = \mathrm{H}_F(\mathbf{x}_{\text{cal}})$.

This was first shown in detail and taken advantage of by Zhang et al's work with PRUNO [129]. The unacquired k-space samples can then be determined by imposing they be consistent with these null space constraints [129, 100, 48, 46].

Because of the repeated entries from the block Hankel structure of $\mathbf{A}$, a transformation from $\mathbf{A}$ to the multi-channel k-space requires enforcing consistency of the entries of $\mathbf{A}$ corresponding to the same k-space coordinates for each channel. This is often done by taking their mean [100, 48, 47, 49], which was what we used, or their median [20]. This "backward" linear operation will be referred to as $H_B$, which enforces block Hankel structural consistency as a result.

### 5.2.1 Determining the Subspace of the Slice-Encoded Calibration

To unfold the signal from a target slice onto $N_{SE} - 1$ other slices, a slice-encoded calibration was acquired which encoded for a through-slice FOV of $N_{SE}S_T$. If the calibration was acquired as a cine, matching the excitation profile of the 2D acquisition and temporal resolution, then the calibration readout will capture the same signal profile as the acquisition cine. Having the acquisition and the calibration in the same breath-hold will let us safely assume both having similar localized channel sensitivity profiles for each frame. These two features, reading out the same signal profile and sharing the same channel sensitivity profiles, are necessary for the two acquisitions sharing a subspace describing the linear relationship of local k-space neighbors.

The null space of $\mathbf{A}^{\text{cal}}$, which is what determines the linear relationship of local k-space

neighbors, can be determined from its SVD:

$$\mathbf{A}^{\text{cal}} = \mathbf{U}^{\text{cal}}\mathbf{S}^{\text{cal}}[\mathbf{V}^{\text{cal}}]^{H} \tag{5.5}$$

where the columns of $\mathbf{V}^{\text{cal}}$ provides the basis of the rows of $\mathbf{A}^{\text{cal}}$ and $\mathbf{S}^{\text{cal}}$ is a diagonal matrix of $\mathbf{A}^{\text{cal}}$'s singular values. The columns of $\mathbf{V}^{\text{cal}}$ corresponding to the significant singular values define $\mathbf{A}^{\text{cal}}$'s row space, $\mathbf{V}_{||}^{\text{cal}}$, and the columns of $\mathbf{V}^{\text{cal}}$ corresponding to the insignificant singular values correspond to its null space, $\mathbf{V}_{\perp}^{\text{cal}}$. A diagonal matrix, $\mathbf{T}$, can be determined to filter between significant from non-significant singular values, forcing the lower singular values to zero, and thereby designating the corresponding singular vectors as the null space. A reasonable estimation of the null space would be the singular vectors correspond to singular values less than the noise floor of the SVD of $\mathbf{A}^{\text{cal}}$, $\sigma_{floor}$ [8, 37, 119, 56, 16]. The shrinkage operator being applied to the $\kappa^{th}$ singular vector of $\mathbf{V}^{\text{cal}}$— which corresponds to singular value $\sigma_{\kappa}$ — can be a hard threshold or some other filter. The minimum variance filter [119, 56, 31, 37]:

$$\begin{aligned} f_{\kappa} &= max(1 - \frac{\sigma_{floor}^2}{\sigma_{\kappa}^2}, 0) \\ \mathbf{T} &= diag(f_{\kappa}) \end{aligned} \tag{5.6}$$

has been shown to generate the closest approximate to $\overline{\mathbf{A}^{\text{cal}}}$ — in the Frobenius norm [119, 56]. This has been used as a shrinkage operation by Bydder et al [16, 20, 19, 18] to avoid explicit rank determination in MRI applications. An illustration of the construction of $\mathbf{A}^{\text{cal}}$ from the slice-encoded calibration, along with examples using minimum variance and hard threshold filters to distinguish $\mathbf{V}_{||}^{\text{cal}}$ from $\mathbf{V}_{\perp}^{\text{cal}}$ is displayed in Figure 5.2A.

### 5.2.2 Iterative Reconstruction Algorithm to Reduce Outflow Corruption

A 2D acquisition is equivalent to an $N_{SE}$ - partition volumetric k-space that has all $N_{SE} - 1$ $k_s \neq 0$ partitions unacquired, with the 2D k-space placed at the $k_s = 0$ plane. Let $\mathbf{x}_{2D}$

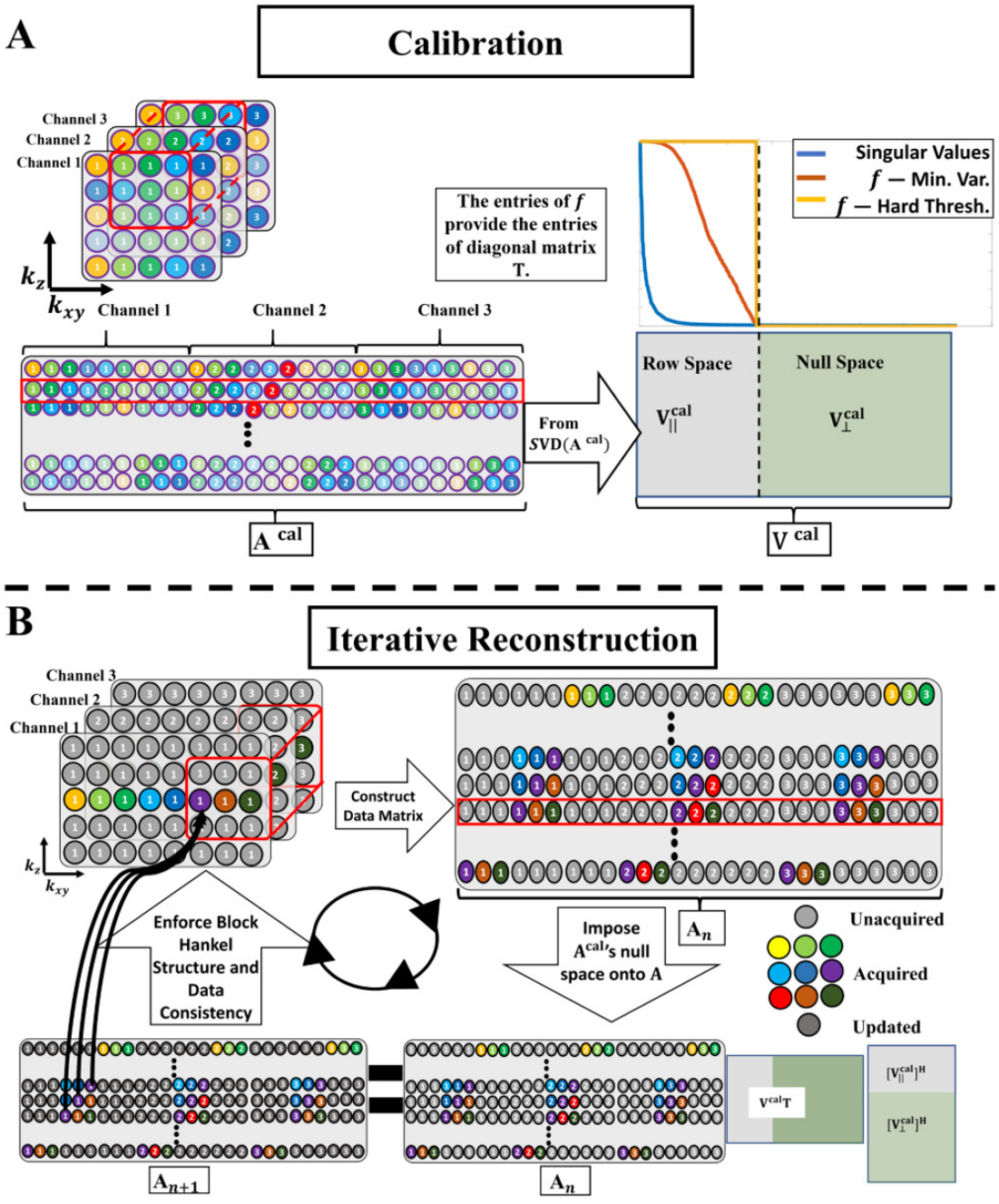


*Figure 5.2: Caption on next page*

*Figure 5.2: A diagram of UNCLE SAM's reconstruction scheme using three-channels to illustrate. (A) The calibration step: Determining* $\boldsymbol{V}^{cal}$ *and* $\boldsymbol{T}$*. The kernel (in this case a 3x3* $< k_{xy}, k_z >$*) slides through the multichannel k-space with the entries of each kernel being vectorized to form a row of a structured autocalibration matrix,* $\boldsymbol{A}^{cal}$*. The linear dependence of local k-space neighbors implies that the rows of the* $\boldsymbol{A}^{cal}$ *reside in a low-rank subspace, which can be verified by a plot of its singular values. Proper thresholding can distinguish the "significant" from the "insignificant" singular values, categorizing their corresponding right singular vectors as either the row space* $\boldsymbol{V}_{||}^{cal}$ *or the null space* $\boldsymbol{V}_{||}^{cal}$*, respectively. Two different filtering functions that can achieve this are displayed here: the minimum variance filter (orange) and the hard threshold (yellow). The filter function used will be the entries of a diagonal matrix,* $\boldsymbol{T}$*. (B) UNCLE SAM's iterative reconstruction. The 2D k-space is treated as the* $k_z = 0$ *partition of a volumetric k-space, with all* $k_z \neq 0$ *unacquired partitions initially set to zero. In each nth iteration, we construct* $\boldsymbol{A}_n$ *(Table 5.1, 7a). This is followed by imposing the null space of* $\boldsymbol{A}^{cal}$ *onto* $\boldsymbol{A}_n$*, by post-multiplying* $\boldsymbol{A}_n$ *by* $\boldsymbol{V}^{cal}\boldsymbol{T}[\boldsymbol{V}^{cal}]^H$ *(Table 5.1, 2B), which was determined from the calibration step, where T enforces the product of any of* $\boldsymbol{A}_n$*'s rows with the columns of* $\boldsymbol{V}^{cal}$ *that correspond to insignificant singular values to zero. Block Hankel structure is imposed on the repeated k-space locations of* $\boldsymbol{A}_{n+1}$ *by averaging the values of the repeated k-space coordinates when returning to an updated multi-channel k-space (Table 5.1, 2C), followed by enforcing data consistency with the acquired 2D k-space (Table 5.1, 2D).*

| | |
|---|---|
| **1** | Calibration (Figure 5.2A) |
| **1A** | $\mathbf{A}^{\text{cal}} = \text{H}_F(\mathbf{x}_{\text{cal}})$ |
| **1B** | $\mathbf{A}^{\text{cal}} = [\mathbf{U}^{\text{cal}}][\mathbf{S}^{\text{cal}}][\mathbf{V}^{\text{cal}}]^H$ |
| **1C** | Estimate $\sigma_{floor}$ |
| **1D** | $f_\kappa = \max(1 - \frac{\sigma^2_{floor}}{\sigma^2_\kappa})$ |
| **1E** | $\mathbf{T} = diag(f)$ |
| **1F** | $\mathbf{x}_0 = D^H \mathbf{x}_{2D}$ |
| **2** | Iterative Reconstruction. Start with $n = 0$ (Figure 5.2B) |
| **2A** | $\mathbf{A}_n = \text{H}_F(\mathbf{x}_n)$ — Construct data matrix. |
| **2B** | $\mathbf{A}_{n+1} = \mathbf{A}_n[\mathbf{V}^{\text{cal}}][\mathbf{T}][\mathbf{V}^{\text{cal}}]^H$ — Impose the null space of $\mathbf{A}^{\text{cal}}$ |
| **2C** | $\mathbf{x}_{n+1} = \text{H}_B(\mathbf{A}_{n+1})$ — Enforce structural consistency of repeated k-space coordinates. |
| **2D** | $\mathbf{x}_{n+1} = (I_d - D)^T(I_d - D)\mathbf{x}_{n+1} + D^T\mathbf{x}_{2D}$ — Data consistency |

*Table 5.1: A description of the iterative, singular value filtering, algorithm used for UNCLE SAM.*

describe this volumetric, multi-channel k-space, with its center partition being the acquired 2D data and zeros in all non-acquired partitions. Allow to $\mathbf{x}$ to be the volumetric multi-channel k-space that we are trying to solve for. With $\mathbf{A} = \text{H}_F(\mathbf{x})$, one can impose the null space constraints of $\mathbf{A}^{\text{cal}}$ onto the unacquired entries of $\mathbf{x}$ by post-multiplying $\mathbf{A}$ with $\mathbf{V}^{\text{cal}}\mathbf{T}[\mathbf{V}^{\text{cal}}]^H$. As a result, the following can be formulated to solve for the unacquired $N_{SE}-1$ k-space partitions[129, 46, 47]:

$$
\begin{aligned}
&\min||\mathbf{A}\mathbf{V}^{\text{cal}}\mathbf{T}[\mathbf{V}^{\text{cal}}]^{H} - \mathbf{A}||_F^2, \\
&st.\mathbf{A} = H_F(\mathbf{x}), \\
&\mathbf{x}_{2D} = D\mathbf{x}, \\
&and\ \mathbf{x} = H_B(\mathbf{A})
\end{aligned}
\tag{5.7}
$$

where $D$ is a matrix that selects the sampled locations from the entire volumetric k-space. Equation 5.7 was solved using a POCS algorithm [22, 21, 23, 38] and whose steps are shown in Figure 5.2 and illustrated in Figure 5.2B. Iterations continued until a convergence of $\frac{||A_n - A_{n-1}||_2}{||A_{n-1}||_2} < 10^{-4}$ was achieved.

## 5.3 Methods

This study was approved by our institutional review board (IRB) and all nine healthy subjects obtained written and approved consent. All acquisitions were carried out on a 3T system (Prisma; Siemens Medical Solutions, Erlangen, Germany). The reconstruction was implemented in MATLAB (Mathworks, Inc.) on an 8GB GPU (Nvidia Titan X; Santa Clara, CA). An implementation algorithm and examples can be found at `www.github.com/faa5115/uncle_sam_recon`.

### 5.3.1 Acquisition

The acquisition parameters were like the previous aim's [3]. They are as follows: $256 \times 184$ in-plane samples, $1.4 \times 1.4\text{mm}^2$ in-plane resolution, 977 Hz/pixel readout bandwidth, 50-degree nominal flip angle, 1.8/3.6 TE/TR, in-plane GRAPPA $2X$ (12 $k_{pey}$ calibration lines for 2D), 6/8 partial Fourier, 12 views-per-segment (VPS). This resulted in a 26 second scan for six-slice-encoded experiments and 4.3 second scan for 2D acquisitions. Because the UNCLE SAM acquisition required having a 2D acquisition being acquired along with a 12 in-plane phase-encoding and 6 slice encoding steps, the prospective UNCLE SAM acquisition required

increasing the breathhold to 10.3 seconds.

### 5.3.2 UNCLE SAM Parameters

A $3 \times 3 \times 3$ $< k_{ro}, k_{pey}, k_s >$ kernel was used when structuring the multichannel k-space when creating the $\mathbf{A}^{\text{cal}}$ and $\mathbf{A}$ data matrices. This kernel size was chosen because, adjacent elements in a kernel have the best spatial harmonic estimation for a target k-space entry [35], in addition to the fact that it was within the limitation of our GPU's memory.

### 5.3.3 UNCLE SAM Evaluation

We used the slice-encoded acquisition as a reference to compare UNCLE SAM with the flow corrupted 2D image on a frame-by-frame basis. This was done to see if UNCLE SAM significantly reduces the extent of outflowing spins corrupting the target slice. We evaluated the residual flow artifacts on the UNCLE SAM reconstructed images, noting that its best performance can only be as good as what slice-encoding can unfold for a given number of slice-encoding steps. The difference of either the center slice of the UNCLE SAM image or of the 2D image with the center slice of the slice-encoded image gives the residual flow artifact in the 2D plane. The L2 norm of either of these differences was calculated and normalized against the L2 norm of the center slice of the slice-encoded image. This gave a quantitative measure of the residual outflow artifact in both images:

$$\Delta F_{SE}(Im_{Test}) = \frac{||(Im_{Test} - Im_{SE}(C_{slice}))_{sos}||_2}{||(Im_{SE}(C_{part}))_{sos}||_2} \tag{5.8}$$

$Im_{SE}$ is the slice-encoded image with $C_{slice}$ refers to its center slice index and $Im_{test}$ refers to either the center slice of the UNCLE SAM reconstruction or the flow corrupted 2D slice. The difference in the $()_{sos}$ is a complex subtraction. This was done for each frame on each patient. In this manuscript, this evaluation will be referred to as the "relative L2 norm difference with slice-encoding." We carried out a two-sided Mann-Whiteny U test for independent samples

to investigate the null hypothesis, which is if there is no statistical difference between the norm of the residual flow effects between the UNCLE SAM reconstructed image and the flow corrupted 2D for $\alpha = 0.05$ significance.

Because the flow artifact manifests as a confounding signal, overshadowing or impacting how the anatomy appears, we compared the structural similarity index measures (SSIM) between the center slices of the UNCLE SAM reconstruction and slice-encoding with the SSIM of the 2D acquisition with the center slice of slice-encoding for each subject. For each of the nine subjects, a Mann-Whitney U test for independent samples was done to answer whether is no statistical difference between the flow corrupted 2D and the UNCLE SAM reconstructed SSIMs. The two-sided evaluation was done for $\alpha = 0.05$ significance.

Lastly, we wanted to evaluate how UNCLE SAM reduction of the outflowing spins from the target slice correlates with the outflow reduction from slice-encoding. The difference of either the center slice of the UNCLE SAM image or of the slice-encoded image with the flow corrupted 2D image results in the flow artifacts subtracted from center slice of either methods. For both, we calculated the L2 norm of the difference of the center slice of UNCLE SAM or of slice-encoding with the 2D acquisition:

$$\Delta F_{2D}(Im_{Test}) = ||(Im_{Test} - Im_{2D})_{sos}||_2 \tag{5.9}$$

where $Im_{Test}$ is either $Im_{SE}(C_{slice})$ or $Im_{US}(C_{slice})$, which is the center slice of the UNCLE SAM reconstruction, and $Im_{2D}$ is the flow corrupted 2D image. This difference was calculated for each frame of each subject of the UNCLE SAM and slice-encoded cines. The null hypothesis was that correlation coefficient between $F_{2D}(Im_{SE}(C_{slice})$ and $F_{2D}(Im_{US}(C_{slice})$ was 0 for $\alpha = 0.05$ significance.

### 5.3.4 Noise Amplification Evaluation

Because we are unfolding signal that spans $N_{SE} - 1$ slices from the target slice, we anticipate noise amplification along the through-sice direction. Because of this we carried out a

geometric factor noise analysis (g-factor) on the reconstruction [90]. For a given dataset, the iterative UNCLE SAM algorithm was run until convergence was achieved. The number of iterations required to reach convergence is denoted as $N_{conv}$. The $\mathbf{V}^{\text{cal}}$ and $\mathbf{T}$ operators were then used on a multi-channel k-space matrix of pure noise entries. This simulated k-space was initialized to have 2X undersampling and partial Fourier in-plane, with the 2D "noise" k-space being the center partition of a volumetric multi-channel k-space with all non-center partitions initialized to zero, just as the UNCLE SAM acquisition described in 5.2.2 and 5.3.1. For slice-encoded, this volumetric mask would be 2X undersampling and partial Fourier in-plane with fully acquisition of all six slice-encoding steps.

The pre-acquisition noise scan is done at a pre-defined bandwidth that is out of the user's control. To determine the noise standard deviation, we added a separate 0 degree flip angle scan to run in the same breathhold the acquisition ran on, with a readout bandwidth the acquisition used in order to determine the noise-standard deviation, $\sigma_{noise}$. An expression for a line of k-space of $N_{ro}$ readout points is $\frac{(\text{randn}(N_{ro},1)+i\cdot\text{randn}(N_{ro},1))\cdot\sigma_{noise}}{\sqrt{2}}$.

The noise simulated UNCLA SAM reconstructions were repeated $N_{sim}$ times. The noise amplification factor was calculated for each spatial voxel as the standard deviation of the voxel entry across across all $N_{sim}$ simulations. For a standard error of 5%, $N_{sim} = 201$.

## 5.4 Results

### 5.4.1 Outflow Artifact Reduction with UNCLE SAM

Figure 5.3 displays a side-by-side comparison of the flow corrupted 2D (left, "2D"), UNCLE SAM (middle, "US"), and slice-encoded (right, "SE") acquisitions for three subjects. The bottom row of each is the square root SOS of the of the complex difference for each channel of $SE-2D$ and $SE-US$. UNCLE SAM and slice-encoding both displays significantly reduced outflow effects. These subtractions treat the slice-encoded images as a reference, because it

explicitly encodes for the volume beyond the target slice to unfold these artifacts, leaving its target slice with no (or minimal) out of slice spins. This results in the $SE - US$ image with only the the flow artifacts UNCLE SAM could not unfold and all outflow artifacts in the $SE - 2D$ image. The extent of the residual outflow effects in the UNCLE SAM images are noticeable, however they show a significant reduction compared to the $SE - 2D$.

A quantitative metric for the residual outflow effects in UNCLE SAM and the flow corrupted 2D image is the relative L2 norm difference with slice-encoding, shown in equation 5.8. This was calculated for each frame of the center slice of UNCLE SAM and the 2D cine for of each volunteer. A pair of box and whisker plots for each subject is shown in Figure 5.4 with the red box plot corresponding to the relative L2 norm difference with each UNCLE SAM frame and black corresponding to the relative L2 norm difference with each 2D frame for a subject. The p-values for each subject's Mann-Whitney U-Test were all ¡ 0.01, suggesting a rejection of the null hypothesis that the two relative L2 norms come from the same statistical population. This implies that UNCLE SAM has less residual outflow effects than a corresponding 2D image, and therefore makes a noticeable improvement in reducing the outflow effects.

There is an obvious skew noticed of the relative L2 norm difference from slice-encoding of the 2D data sets. A histogram of all relative L2 norm differences with slice-encoding for 2D and UNCLE SAM also shows this skew on the 2D data sets. These pairs of histograms are shown in Figure 5.5. These large differences in the 2D data correspond to the extreme out of slice effects seen for peak systolic frames of the subjects. The relative L2 norm difference with slice-encoding for UNCLE SAM is much less skewed, showing its capability to unfold most outflowing spins, even in extreme cases. Across all frames of all subjects, there is a statistically significant difference in relative norm of the residual outflow effects between UNCLE SAM and 2D, as indicated by a p-value $< 0.01$.

The noticeable outflow artifact reduction seen in UNCLE SAM was further confirmed with the SSIM results comparing UNCLE SAM and 2D with slice encoding. Box plots of these

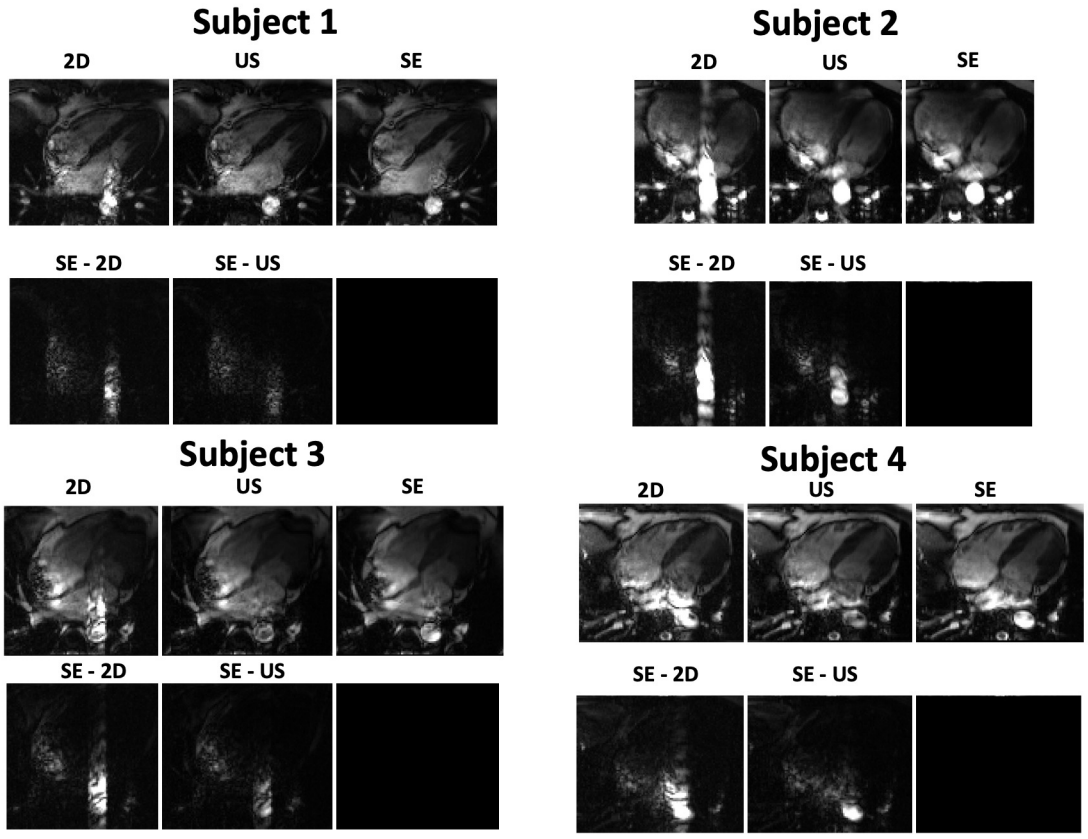


*Figure 5.3: Example images of peak systole from three subjects, with two rows each. Top row (left to right): flow corrupted 2D image ("2D"), center slice of the image from UNCLE SAM ("US"), and the center slice of the slice encoded ("SE") image. Bottom row: the sum of squares image of the channel by channel subtraction of the center slice of the slice-encoded image from the 2D image (right, "$SE - 2D$") and from the center slice of the image from UNCLE SAM ("SE - US"). The 2D acquisition shows an outflowing signal pileup that is significantly reduced in slice-encoding's and UNCLE SAM's images. SE–2D shows the complex sum of all outflowing spins + slight residual difference from the imperfect excitation profile. The SE–US image shows some residual outflow effects that UNCLE SAM could not capture.*

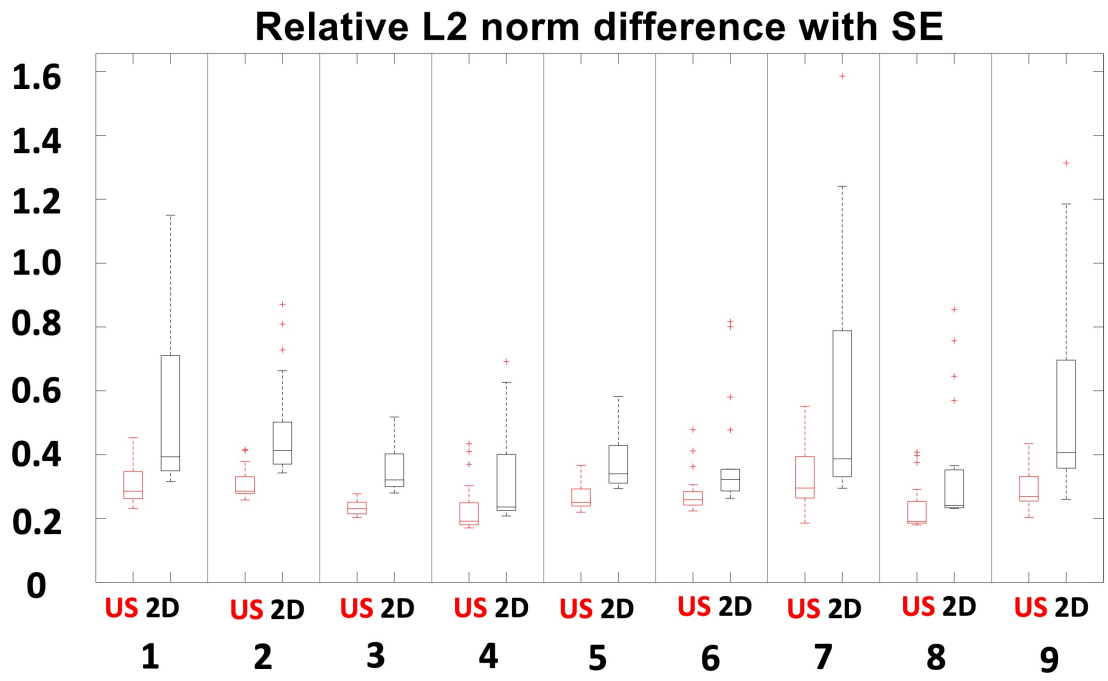


*Figure 5.4: Box and whisker plots showing the summary of the relative L2 norm difference (equation 5.8) with slice-encoding of each frame for each of the nine subjects. Red box plots display the summary of the range of the relative L2 norm difference with UNCLE SAM, and the black box plots show the relative L2 norm difference with the flow corrupted 2D images. The wide range seen in the relative L2 norm difference of the 2D images result because the peak systolic frames have much more through-plane outflow effects than the diastolic frames. p-Values of Mann-Whitney U-Tests were all ¡ 0.01, indicating that the relative L2 norm difference between UNCLE SAM and 2D have with slice-encoding is significantly different when imaging in the presence of through-plane flow effects.*

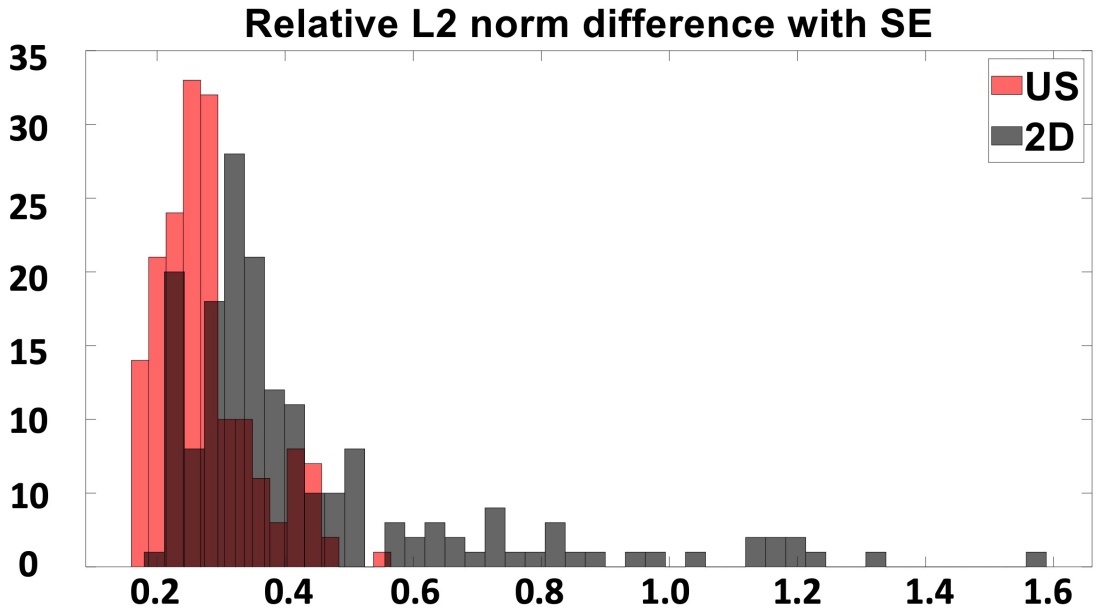


*Figure 5.5: A histogram of the relative L2 norm difference with SE for UNCLE SAM (red) and 2D (black) for all frames, across all volunteers.*

results are shown for each subject in Figure 5.6. All p-valeus were ¡ 0.01, showing that there is a significant difference between each of there structural comparison with the slice-encoded image.

Results comparing UNCLE SAM's slices to slice-encoding's are shown in Figure 5.7 The top displays all slice-encoded slices while the bottom shows the recovered six UNCLE SAM slices. The center slice for both is slice number four, and is indicated with an orange and yellow box for slice-encoding and UNCLE SAM, respectively. Although the recovered UNCLE SAM slices show similar outflow profiles as the slice-encoded acquisition, its unfolding of the outflowing spins from the adjacent slices (3 and 5) was not as good as the unfolding of slices further away. We suspect that this likely contributed to the residual effects seen in the *SE–US* subtractions in Figure 5.3. This shortcoming is likely to occurred as a result of limited channel sensitivity variation between slice 4 and either of its two adjacent slices.

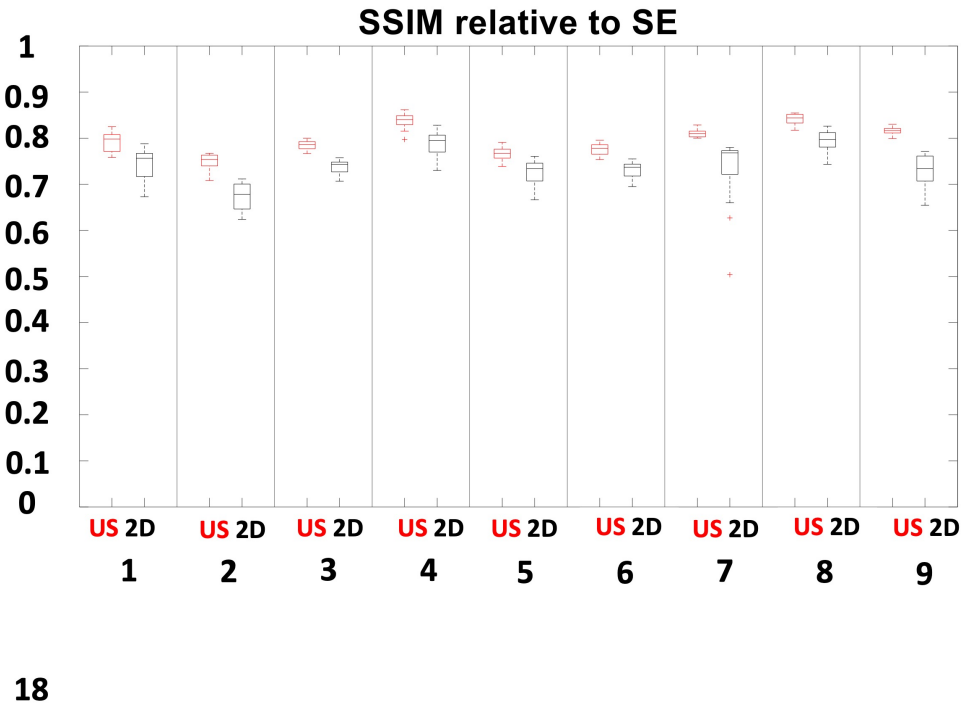


*Figure 5.6: A histogram of the SSIM with with SE for UNCLE SAM (red) and 2D (black) for all frames, across all volunteers. p-Values of Mann-Whitney were all less than 0.01 for each subject, indicating that the SSIM relative to slice-encoding between UNCLE SAM and 2D is significantly different when imaging in the presence of through-plane flow effects. SSIM values close to 1 indicate structural similarity*

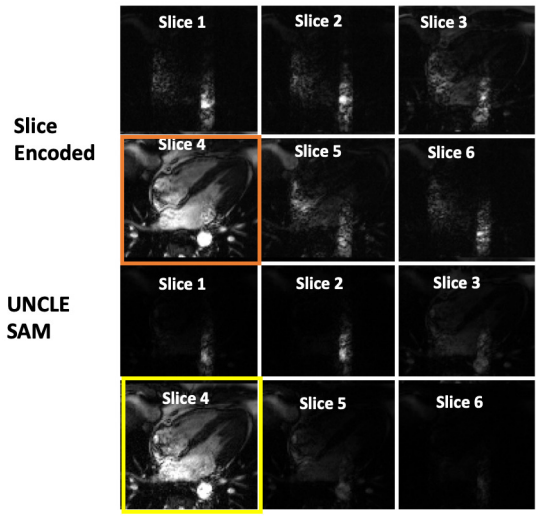


*Figure 5.7: All six slices of the slice-encoded (top) and UNCLE SAM(bottom) images, with the center slices indicated with brown and yellow boxes of the two respective methods. UNCLE SAM performed much better in unfolding the outflow effects seen in slices further away from the target, noticeably slices 1 and 2, than the slices directly adjacent.*

This limitation of UNCLE SAM's is further shown in the bottom two rows of Figure 5.8. The columns in this figure correspond to peak systolic frames of a subject. The top three rows show the center slice of UNCLE SAM ("US"), center slice of slice-encoding ("SE"), and the 2D ("2D") frames respectively. The bottom two rows show the sum of squares of the images that result from a complex subtraction of the individual channels of the 2D data from the respective UNCLE SAM ("$US - 2D$") and slice-encoded ("$SE - 2D$") frames. Subtracting these images from the flow corrupted 2D data show a 2D plane projection of the outflow effects they were able to unfold from the target slice. Because slice-encoding removes most outflowing spins from the target slice, $SE - 2D$ gives us the projection almost all of the outflow artifacts present in the acquisition. These projections show that UNCLE SAM could only most of the outflow artifacts present in the acquisition. The amount of outflow effects vary for each frame, as does the amount of unfolded spins from UNCLE SAM, which means that the unfolding of UNCLE SAM scales with the amount of artifacts present. This

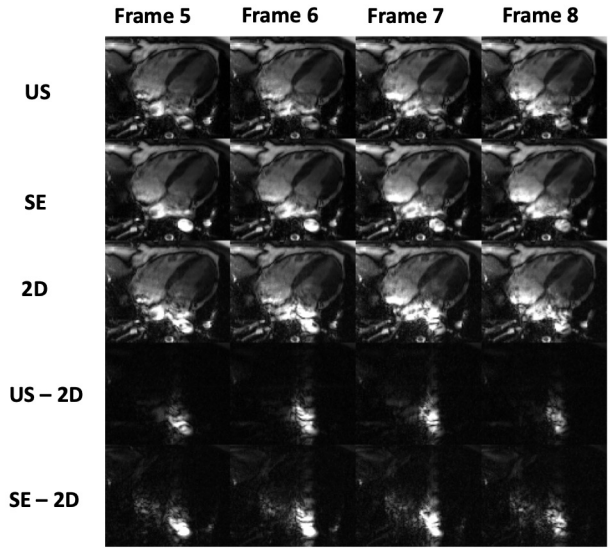


*Figure 5.8: Top three rows show the systolic frames (5, 6, 7, and 8) of a subject's UNCLE SAM ("US"), slice-encoding ("SE"), and flow corrupted 2D ("2D") images. The next two rows show the sum of squares of the complex subtraction of the 2D images subtracted from the UNCLE SAM ("$US-2D$") and from slice-encoding ("$SE-2D$") images respectively. These bottom two rows show the outflow effects unfolded from the target slice projected on a 2D plane.*

is verified by the correlation between the L2 norm of the 2D subtraction from UNCLE SAM and from slice-encoding. The R value for each is shown in Table 5.2.

| Parameter | Vol1 | Vol2 | Vol3 | Vol4 | Vol5 |
|---|---|---|---|---|---|
| R | 0.9982 | 0.9955 | 0.9954 | 0.9850 | 0.9846 |
| Parameter | Vol6 | Vol7 | Vol8 | Vol9 | X |
| R | 0.9847 | 0.9896 | 0.9844 | 0.9902 | X |

*Table 5.2: The Pearson Correlation test results for the L2 norm of the subtraction of the 2D data from UNCLE SAM and slice-encoding for each subject. Because slice-encoding unfolds most outflowing spins, $||SE-2D||_2$ provides the norm of almost all outflow effects corrupting the 2D image. The p values were all less than 0.01. This indicate the unfolding of outflow effects using UNCLE SAM strongly correlates with the extent of outflow artifacts in an acquisition.*

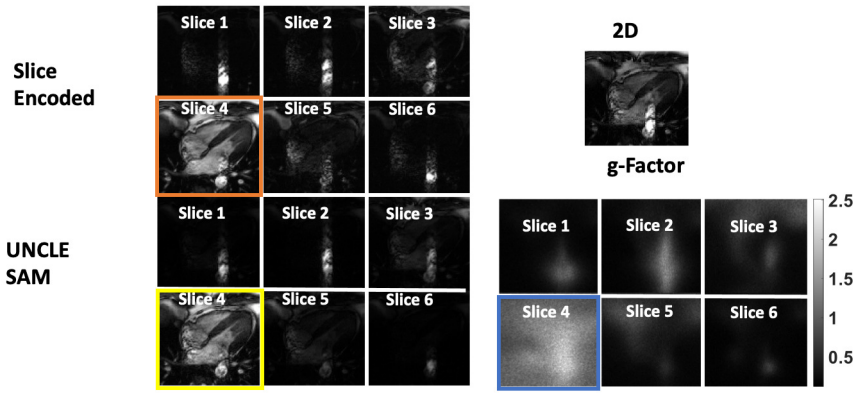


*Figure 5.9: A g-factor analysis of UNCLE SAM, relative to the six slice-encoded experiment, described in section 5.3.4. Peak noise amplification occurred at 2.5, where the outflowing spins would typically appear.*

Figure 5.9 displays slice-by-slice results of a g-factor measurement, relative to slice-encoding. g-Factor peaked at 2.5 in the targe slice in the region from where the flow artifacts unfolded.

## 5.5 Discussion

In this project, we sought to build upon our previous slice-encoding technique by exploiting the localized channel sensitivity of the outflowing spins to substitute for slice-encoding steps. We credit the achievements of previous parallel imaging techniques — which expressed linear dependence of neighboring multi-channel k-space elements as a structured low-rank block-Hankel matrix — for laying the foundation for this work. As a result of this linear dependence, each local k-space neighborhood across all channels resides in a compact subspace. UNCLE SAM works by explicitly imposing a null space onto $\mathbf{A}$ at each iteration, which is determined from the slice-encoded calibration data. This is like PRUNO [129] and auto-calibrated LORAKS [46, 47]. Specifically, they enforce an equality constraint between the acquired and not acquired k-space entries in a kernel, with each entry dotted by its respective null space coefficients. This is equivalent to our approach, where we post-multiply $\mathbf{A}_n$ by $\mathbf{V}^{\text{cal}}\mathbf{T}[\mathbf{V}^{\text{cal}}]^H$ in each n iteration, where $\mathbf{V}^{\text{cal}}$ and $\mathbf{T}$ are both determined from the slice-encoded calibration before the reconstruction starts. As a shrinkage or thresholding

operator, $\mathbf{T}$ forces the product of $\mathbf{A}_n$'s rows with $\mathbf{V}^{\text{cal}}$'s columns that correspond to $\mathbf{A}^{\text{cal}}$'s insignificant singular values to zero, imposing $\mathbf{A}^{\text{cal}}$'s null space onto $\mathbf{A}_n$. We used the noise floor to threshold for the null space by employing the minimum variance filter, which is the most proximal estimation of $\mathbf{A}^{\text{cal}}$ in the Frobenius norm [119, 56]. We are not claiming novelty over the use of this filter. Rather we used it as a pragmatic thresholding criterion for the null space from the SVD of $\mathbf{A}^{\text{cal}}$, like other MR imaging applications [16, 20, 19, 18]. We show a comparison between using the minimum variance filter and a manual threshold in Figure 5.10. The left image of part A illustrates the normalized singular values (colored blue) along with the minimum variance filter (orange) and the hard thresholding filter (yellow). The right image shows plots of Equation 5.7 for UNCLE SAM's first 800 iterations when using the minimum variance filter (orange) and the hard threshold (yellow) as the diagonal entries of $\mathbf{T}$. Equation 5.7 converged after 298 iterations when using the minimum variance filter (red vertical bar) and converged after 605 iterations when using the hard threshold. From left to right, part B shows a side-by-side comparison of the outflow corrupted 2D image, UNCLE SAM's reconstruction using the minimum variance filter, UNCLE SAM's reconstruction using hard thresholding, and the magnitude of the complex difference between the minimum variance and hard threshold images. Both filters resulted in similar outflow unfolded images, which makes sense because both imposed the same null space that defines the relationship of local k-space neighbors. An in-depth evaluation of the shrinkage criteria is beyond the scope of this project and is an active research topic [8].

Because UNCLE SAM incorporates aspects of prior parallel imaging developments, it is important to emphasize that the novelty of this work comes from the application of exploiting the linear dependence of slice-encoded k-space neighbors to unfold outflow effects rather than any specific algorithm. In fact, an early version was implemented using SMASH [2]. We make of use the insight that the coils inherently encode a 3D volume even though the sequence encodes for 2D only. Similarities can be drawn with prior simultaneous multi-slice (SMS) methods [60, 78] , where multiple discretely positioned slices are unfolded from one

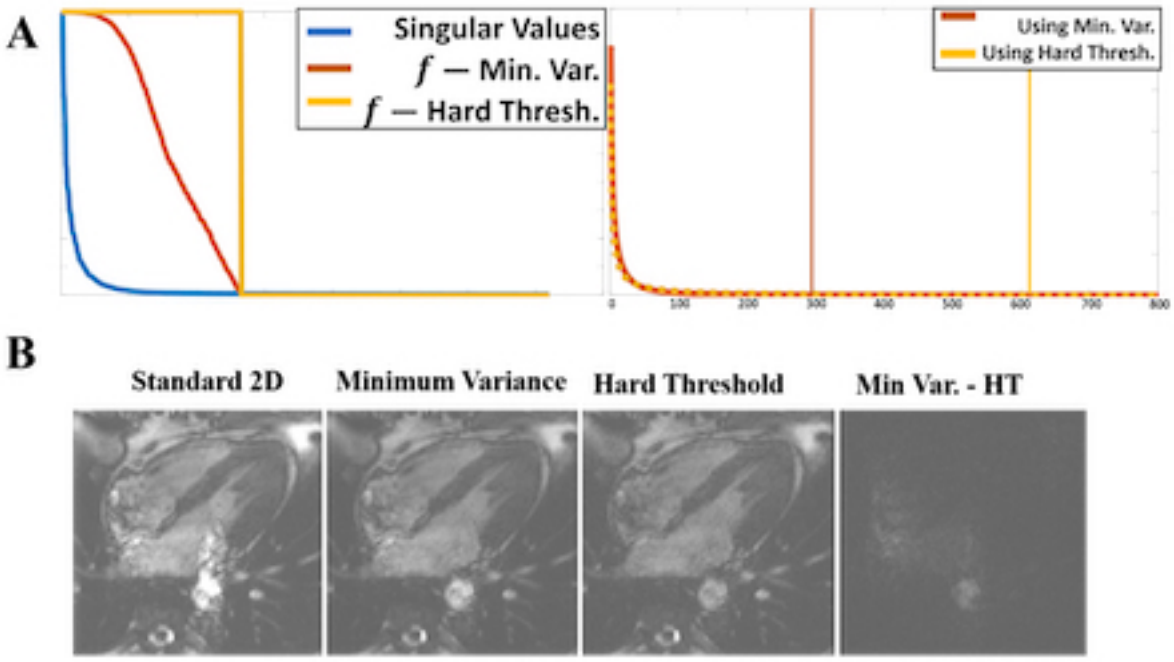


*Figure 5.10: (A) Left Image: A comparison of thresholding criterion used to determine the null space: minimum variance threshold (orange) and hard thresholding at the noise floor (yellow). Both are plots of the normalized singular values and the thresholding filter, $f$. The thresholding filter served as the diagonal entries of the thresholding operator, $\boldsymbol{T}$. Right Image: plots of Equation 5.7 for each iteration using the a minimum variance filter (orange) and the hard threshold (yellow) filter as the diagonal entries of $\boldsymbol{T}$. The orange and yellow vertical bars indicate when Equation 5.7 evaluated to less than $10^{(}-4)$ when using the minimum variance filter and hard thresholding for $\boldsymbol{T}$ respectively. Convergence occurred after 298 iterations when using the minimum variance filter, while occurred after 605 iterations when using hard thresholding. (B) A side-by-side comparison of the fiwo corrupted 2D image, the center slice of UNCLE SAM using the minimum variance filter, the center slice of UNCLE SAM using a hard threshold, and a difference of the minimum variance and hard thresholded filter images. The thresholding operator's significance is only to determine the null space that defines the linear relationship between the local neighborhoods of slice-encoded k-space entries. Because of this, both filters achieved similar outflow unfolding.*

another after being excited simultaneously. More recently developed SMS methods benefit from controlled aliasing in parallel imaging (CAIPI) condition [14, 15], where the spins from different slices each accumulate different FOV shifts in-plane. Unfortunately this method of encoding is not possible for the current case, because all excited spins come out of the center slice, making it impossible to impart slice-specific encoding. Slice-GRAPPA [99, 25] was developed as a method that doesn't inherently rely on, but would still benefit from, CAIPI. In the calibration step, weights are determine to fit the multi-channel k-space weights of the sum of all slices to the k-space of the individual slice. This k-space fitting is different from traditional k-space weighting in parallel imaging. In parallel imaging, the weights are estimated to miming the spatial harmonics achieved for k-space sampling. In slice-GRAPPA, the weights are working to vectorially cancel the signal of all other slices, leaving only the target slice, in a manner similar to beamforming[70, 58] along the slice direction. Without CAIPI, slice-GRAPPA works best for slices separated by great lengths. Because excited spins come out of the center slice in flow artifacts, it is difficult for slice-GRAPPA to consistently vectorially cancel outflowing spins from slices adjacent to the target slice, limiting the resolvable of outflow artifacts coming from the nearest slices. This is shown in an example in Figure 5.11.

The slice-encoded raw data was used to test UNCLE SAM's fidelity in a direct comparison with explicit slice-encoding. Both methods unfolded similar outflow profiles (Figure 5.7). Because the 2D image was from the $k_s = 0$ plane of the slice-encoded data, the sum of squares of the channel-by-channel 2D subtraction from the slice-encoded gave the projected sum of all outflowing spins (second row of all images of Figure 5.3). In contrast, we showed in Figure 5.3 that the complex subtraction of the UNCLE SAM image from the slice-encoded resulted in marginal residual through-plane flow effects. Because slice-encoding explicitly encodes for the space where most of outflowing spin reside, the complex subtraction of the slice-encoded image from UNCLE SAM or 2D only leaves residual outflow effects. We quantified the extent of these residual outflow effects by calculating the relative L2 norm difference

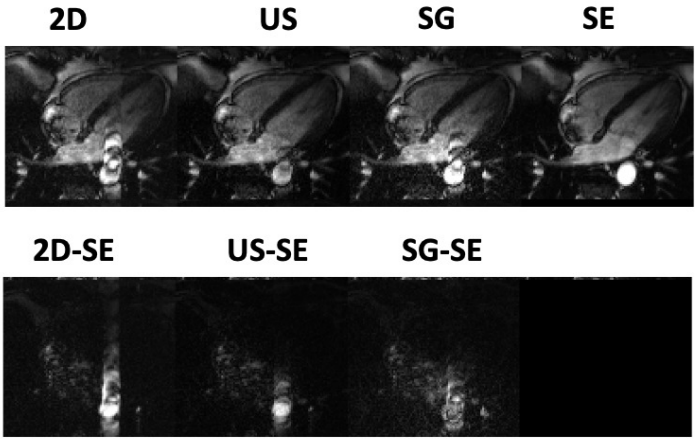


*Figure 5.11: Top from left to right: 2D, UNCLE SAM, slice-GRAPPA ("SG"), and slice-encoding. Bottom shows the sum of squares of the channel-by-channel complex subtraction of (from left to right): $2D - SE$, $US - SE$, and $SG - SE$. This is illustrates a side-by-side comparison between UNCLE SAM and slice-GRAPPA, showing that UNCLE SAM can unfold more than slice-GRAPPA for six SE step experiments.*

from slice-encoding, in equation 5.8. For each frame of each subject, this difference was significantly less for UNCLE SAM than it was for the flow corrupted 2D image. This indicated by p-value ¡ 0.01 for the Mann-Whitney U-Tests for each subject's UNCLE SAM and 2D cines, as well as for all pairs of UNCLE SAM and 2D frames for all subjects (Figures 5.4 and 5.5). It must be noted that these subtractions did introduce a bias because singular value shrinkage does inherently denoise the UNCLE SAM images. We also carried out SSIM evaluations for the UNCLE SAM and 2D images in comparison to the slice-encoded image to have feature a metric that isn't as sensitive to denoising effects. The SSIM evaluations for the UNCLE SAM and 2D images in comparison to the slice-encoded image is a appropriate because outflow effects provide visual corruption of the image. These evaluations further confirmed the significant reduction of outflow effects using UNCLE SAM. As this was all retrospective from the slice-encoded data, these results provided a theoretical and demonstrative evidence UNCLE SAM's acquisition and reconstruction scheme, without any concern of misregistration.

We suspect that the residual through-plane flow effects of the "*SE–US*" images in the second row of Figure 5.3 had to do with the limited resolution of the localized channel sensitivity along the slice direction. Imperfections in UNCLE SAM's unfolding can be seen in slices 3 and 5 of Figure 5.7, which are directly adjacent to the center slice. The through-slice FOV between the center slice to either of its two adjacent slices is too small for significant channel sensitivity differences [51]. As a result, using UNCLE SAM for the spatial unfolding of these artifacts is best for fast moving outflowing spins, particularly for those moving along the slice's normal. Because of this, UNCLE SAM is unlikely to be suitable for distinguishing stationary spins across different slices, at least without some additional phase-encoding. Through-slice localization could be potentially improved for acquisitions featuring a phased array system with more localized through-slice channel sensitivity [51, 50], particularly if the center of the channel's sensitivity profile could be positioned at each midpoint of the unfolding slices [60, 78]. Despite this limitation, we showed that UNCLE SAM was able to unfold most of what slice-encoding was able to achieve in Figure 5.8 by directly subtracting the image from each of them. This complex subtraction from their center slices leaves the artifacts they unfolded.

Better localized through-slice channel sensitivity provides better estimation of through-slice spatial harmonics. Channel sensitivity profile sets a limit on how many through-slice encoding steps UNCLE SAM can achieve. Figure 5.12 shows two UNCLE SAM comparisons with slice-encoding. The top left shows a comparison with six slice-encoding steps and the top right shows a comparison with eight slice-encoding steps. UNCLE SAM with six encoding steps achieved a better estimation of the outflow profile than it did with eight encoding steps. Presumably this reflects the impossibility of achieving 8-fold linear acceleration across adjacent slices.

Prospective UNCLE SAM scans, whose calibration featured 12 in-plane samples for six slice-encoding steps, increased the total breath-hold by six seconds for 12 VPS evaluations. To put

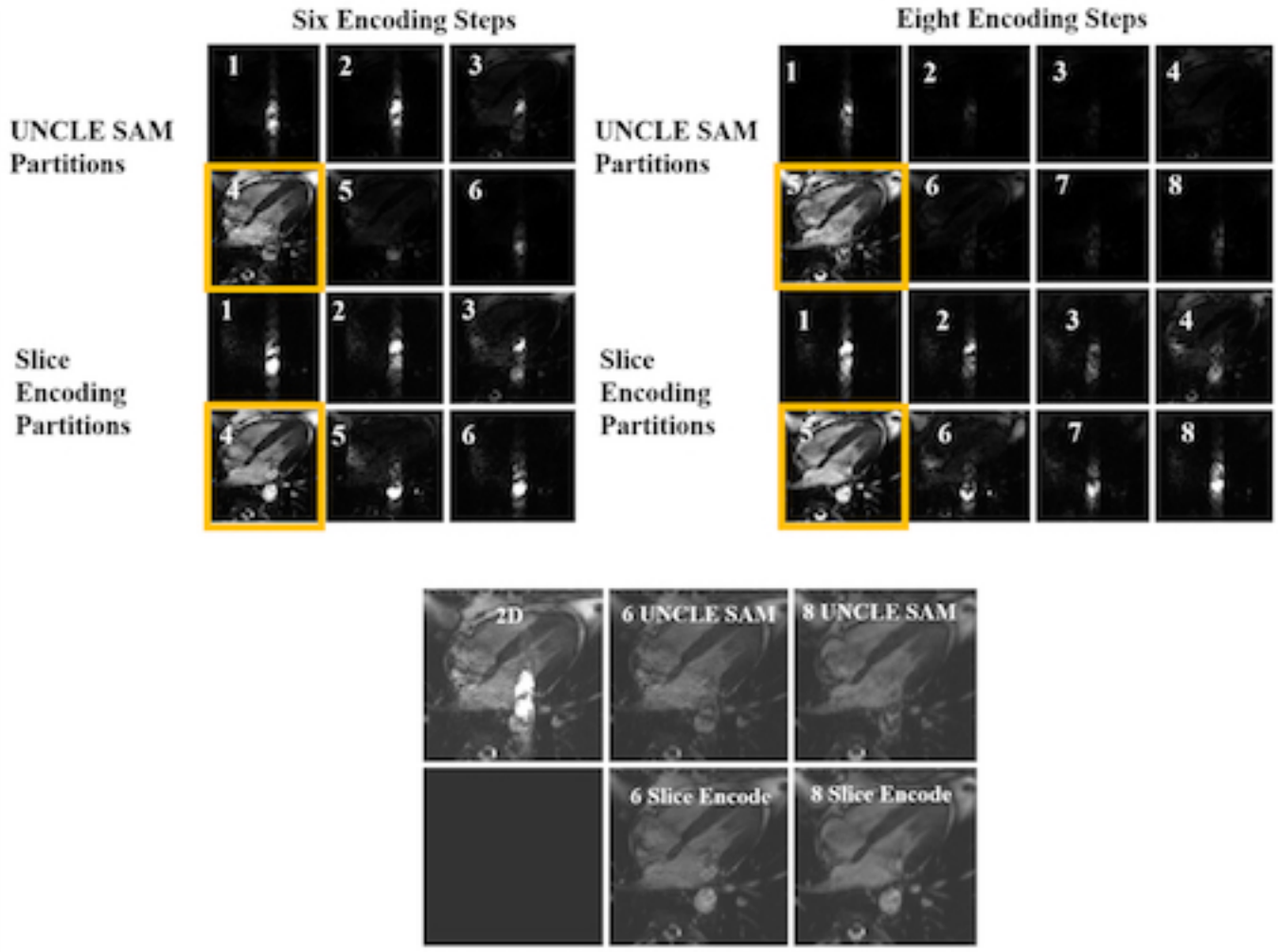


*Figure 5.12: Top: Slice-by-slice comparison of UNCLE SAM with slice-encoding for six encoding steps (left) and eight (right). With Siemens's standard chest coil for the Prisma, UNCLE SAM was better able to achieve the six-encoding step resolved outflow profile than it was for eight encoding steps. Bottom: a side-by-side comparison of the 2D image with the center slice of the six encoded UNCLE SAM, the eight encoded UNCLE SAM, the six slice-encoded, and eight slice-encoded images. Because of the improved outflow profile localization of the six encoded UNCLE SAM experiment, six UNCLE SAM steps achieved better outflow unfolding from the center slice than using eight UNCLE SAM steps.*

this increased scan time in perspective, slice-encoded acquisition times scaled by a factor of the number of slice-encoding steps. Despite subtle channel localized imperfections, UNCLE SAM was able to unfold most of the outflowing signal profile from the target slice with only a marginal increase in the breath-hold duration of the 2D acquisition.

Some other limitations of the study should be noted. The reconstruction time is presently on the order of minutes to hours, as is common with null space algorithms. Incorporating the GIRAF framework [83] could potentially speed the computation. Alternatively, a less sophisticated parallel imaging techniques may be implemented to obtain similar results [2] but potentially less artifact reduction. The requirement for a calibration scan to measure the coil sensitivities is another limitation. In our implementation the acquisition consisted of a 2D acquisition combined with a six slice-encoded calibration, which effectively only increased the breath-hold by six seconds. Because these two cines are acquired together in the same breath-hold, and have the same temporal resolution, they will have consistent channel sensitivity and transverse signal profiles for each frame. This will help guarantee the two cines share the same subspace, even for cases with severe outflow effects. This is also how calibration consistency in cardiac cine is guaranteed for in-house parallel imaging techniques, including GRAPPA [43] and SENSE [90]. Because of this implementation, the issue with severe outflow effects is more related to the number of encoding steps needed to significantly unfold them from the center slice, which requires a sufficient channel sensitivity variation along the slice's direction. This is a significant improvement from increasing the scan's time by a factor of the number of slice-encoding steps. Different implementations could use a separate breath-hold for calibration or internal calibration, in common with other parallel imaging techniques.

## 5.6 Conclusion

In this study, we sought to unfold most outflow effects in bSSFP imaging in a time- efficient manner, relative to through-plane phase-encoding. We integrated concepts from recently developed parallel imaging methods that featured a low-rank framework with our slice-encoding approach. In retrospective and prospective acquisitions, we were able to show that our proposed method can significantly reduce a large fraction of the outflow present in the standard clinical protocol.

# CHAPTER 6

# Summary and Future Directions

## 6.1 Summary

We investigated through-plane flow effects in this thesis. On one hand, these effects have use and can be exploited for clinical purposes. In the first specific aim, we specifically used through-plane effects in arterial spin labeling to assess for regional foot perfusion. These initial results were promising, as they showed that ASL MRI can provide regional foot assessment in patients with diabetic foot ulcers, detecting increased perfusion closer to the foot ulcer than regions further away. Further investigation is needed in order to see how the ASL measurements can help predict the healing potential of a wound.

The next two specific aims focused on a specific through-plane flow problem in MR Imaging: outflow effects in 2D bSSFP acquisitions. In specific aim two, we treated the outflow effects in 2D bSSFP imaging as a volumetric signal profile by applying slice-encoding steps to spatially encode for a through-slice FOV beyond the target slice in order to unfold them from the image. In our methods, we encoded for a through-slice FOV of $N_{SE}S_T$. Through thorough Bloch simulations of through-plane flowing spins, and flow phantom experiments with through-plane flow, we should that outflow effects can be reduced with an increasing number of slice-encoding steps, and ultimately removed if the encoding FOV covers the span of the outflowing signal. This was tested on several healthy subjects and showed a significant reduction of outflow effects on 2D bSSFP imaging on a 3 Tesla system.

However, incorporating slice-encoding steps in clinical or research protocols for cases with severe outflow effects is impractical because of the penalty in acquisition time. Because the spins are moving through the slice, we decided to take advantage of the difference between the localized channel sensitivities between the outflowing spins and the target slice in order to reduce the needed breath-hold to unfold out of slice spins. In addition to the 2D cine, we acquired a slice-encoded calibration, which only added about six seconds to the total scan time. We used the calibration data to learn the subspace defining the linear relationship amongst local slice-encoded k-space neighbors. By treating the acquired multi-channel 2D data as the center slice of a volumetric k-space with zeros everywhere else, we imposed this subspace onto the k-space to estimate the non-center k-space partitions.

## 6.2 Future Directions

In this section, I mention some potential future projects, along with preliminary results. I can provide the relevant source code.

### 6.2.1 An UNCLE SAM implementation of Slice-GRAPPA

Slice-GRAPPA is an SMS method that estimates a k-space entry of a target slice of a single channel as a linear combination of k-space neighbors of another slice across all channels [99]. We recently implemented a low rank interpretation of this, whose implementation is similar to UNCLE SAM, with a preliminary result being shown in Figure 6.1. A further investigation would include a direct comparison with UNCLE SAM, such as relative L2 norm difference with slice-encoding, L2 norm evaluation in difference from 2D, g-factor analysis, along with seeing if including beyond six encoding steps in the calibration would result in more outflow unfolding.

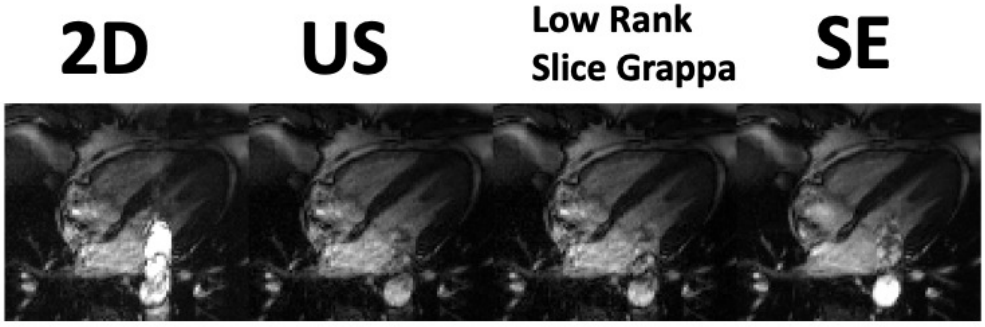


*Figure 6.1: Side-by-side comparisons of 2D, UNCLE SAM, Low Rank Slice Grappa, and Slice Encoding.*

### 6.2.2 A Low Rank Approach to Reduced FOV Imaging

Recent development in MRI involved the incorporation of beamforming concepts for reduced FOV imaging [70, 58]. So far these implementations were based off of the stochastic matched filter Walsh et al discussed [122]. Instead of reducing the noise power, which was what Walsh discussed, they reduced the power from the signal of an unwanted region, while maximizing the power from the signal within the desired FOV. These approaches resulted in coil compressed (*virtual coils*) data.

Conceptually, the reconstruction for slice-grappa [99] operates as reduced FOV. In the calibration step, slice-grappa fits the k-space of the sum of all slices to the k-space of a target slice. The weighted sum of the multi-slice k-space will result in the k-space of the target image, with the signal of all other slices cancelled.

On a similar note, one should be able to fit the calibration k-space spanning a full FOV to the k-space of a cropped FOV of that calibration image. Then the weighed sum of the acquisition k-space should result in the reduced FOV. Preliminary results are shown in Figure 6.2.

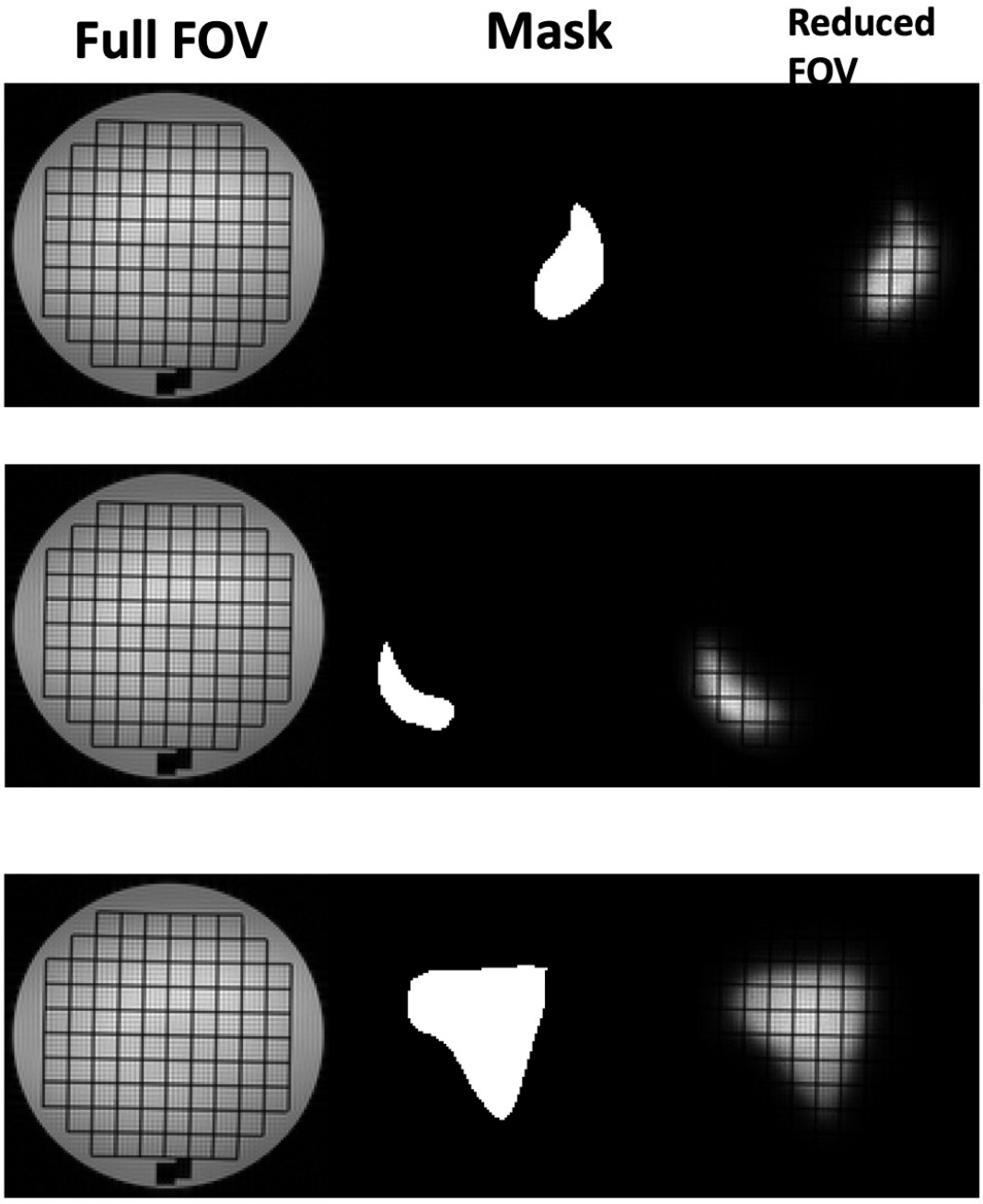


*Figure 6.2: Preliminary results of the reduced FOV method.*

# APPENDIX A

# Appendix

Here we describe a simplified view of E-SPIRiT [118], coming from a spatial harmonic perspective. This was something I did on the side to test my understanding of the k-space based parallel imaging methods, and was glad to see (or rediscover) that sensitivity maps could come GRAPPA weights.

The k-space of a given channel $j$:

$$S_j(k_x, k_y) = \iint C_j(x, y) M_\perp(x, y) e^{-i2\pi\cdot(k_x x + k_y y)}\, dx\, dy \tag{A.1}$$

Any k-space element at position $(k'_x, k'_y)$ of channel $j$ can be estimated as a linear combination of surrounding neighbors across all channels. If we consider the neighbors that lie within a $M_x$ and $M_y$ elements away along the $\vec{x}$ and $\vec{y}$ directions respectively, the following estimation is carried out:

$$S_j(k'_x, k'_y) = \sum_{l=1}^{N_c} \sum_{\substack{m_x=-M_x,\\ m_y=-M_y}}^{M_x, M_y} S_l(k'_x + m_x\Delta k_x, k'_y + m_y\Delta k_y) n_l^{(m_x, m_y, j)}\big|_{\substack{m_x \\ \wedge m_y \neq 0}} \tag{A.2}$$

$m_x$ and $m_y$ cannot both equal zero at the same time because that refers to missing index.

Expressing A.2 in terms of A.1 :

$$S_j(k'_x, k'_y) = \iint C_j(x,y) M_\perp(x,y) e^{-i2\pi\cdot(k'_x x + k'_y y)}\, dx\, dy = \sum_{l=1}^{N_c} \iint C_l(x,y) M_\perp(x,y) \cdot \sum_{\substack{m_x=-M_x,\\ m_y=-M_y}}^{M_x,M_y} e^{(-i2\pi\cdot((k'_x+m_x\Delta k_x)x+(k'_y+m_y\Delta k_y)y))} n_l^{(m_x,m_y,j)}\big|_{\substack{m_x\\ \wedge m_y\neq 0}} dx\, dy \quad \text{(A.3)}$$

Rearranging A.3 gives:

$$S_j(k'_x, k'_y) = \iint C_j(x,y) M_\perp(x,y) e^{-i2\pi\cdot(k'_x x + k'_y y)}\, dx\, dy = \iint M_\perp(x,y) e^{(-i2\pi\cdot(k'_x x + k'_y y))} \cdot \sum_{l=1}^{N_c} C_l(x,y) \cdot \sum_{\substack{m_x=-M_x,\\ m_y=-M_y}}^{M_x,M_y} e^{(-i2\pi\cdot((m_x\Delta k_x)x+(m_y\Delta k_y)y))} n_l^{(m_x,m_y,j)}\big|_{\substack{m_x\\ \wedge m_y\neq 0}} dx\, dy \quad \text{(A.4)}$$

Equaling like terms gives us

$$\hat{C}_j(x,y) = \sum_{l=1}^{N_c} C_l(x,y) \sum_{\substack{m_x=-M_x,\\ m_y=-M_y}}^{M_x,M_y} e^{(-i2\pi\cdot((m_x\Delta k_x)x+(m_y\Delta k_y)y))} n_l^{(m_x,m_y,j)}\big|_{\substack{m_x\\ \wedge m_y\neq 0}} \quad \text{(A.5)}$$

where $\hat{C}_j(x,y)$ is the estimated spatial sensitivity of channel $j$. Let's condense the harmonic summation:

$$H_l^j(x,y) = \sum_{\substack{m_x=-M_x,\\ m_y=-M_y}}^{M_x,M_y} e^{(-i2\pi\cdot((m_x\Delta k_x)x+(m_y\Delta k_y)y))} n_l^{(m_x,m_y,j)}\big|_{\substack{m_x\\ \wedge m_y\neq 0}} \quad \text{(A.6)}$$

This gives us the following dot product to estimate $\hat{C}_j(x,y)$:

$$\begin{aligned} \hat{C}_1(x,y) &= [H_1^1(x,y), H_2^1(x,y), ...H_{N_c}^1(x,y)] \cdot \vec{C}(x,y) \\ \hat{C}_2(x,y) &= [H_1^2(x,y), H_2^2(x,y), ...H_{N_c}^2(x,y)] \cdot \vec{C}(x,y) \\ &... \\ \hat{C}_{N_c}(x,y) &= [H_1^{N_c}(x,y), H_2^{N_c}(x,y), ...H_{N_c}^{N_c}(x,y)] \cdot \vec{C}(x,y) \end{aligned} \quad \text{(A.7)}$$

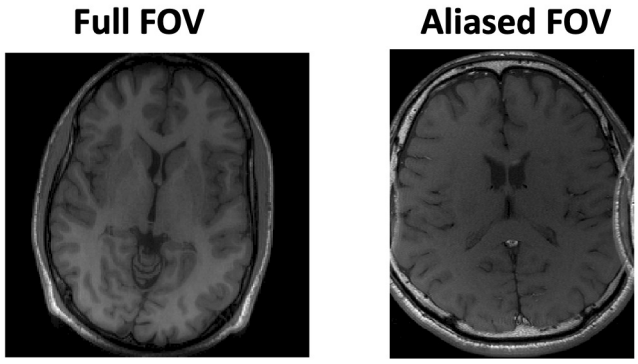


*Figure A.1: The brain data sets we tested this interpretation of E-SPIRiT on. We will work with a full FOV (left) and an aliased (right) datasets.*

where $\hat{C}(x, y)$ indicates the estimated channel sensitivity. or in short:

$$\hat{\vec{C}}(x, y) = [\mathbf{H}(x, y)]\vec{C}(x, y) \tag{A.8}$$

This shows that the channel sensitivities can be estimated by determining the eigen vectors corresponding to eigen value 1 of $\mathbf{H}(x, y)$.

We tested this on multi-channel brain data from Michael Lustig's website (Figure A.1) using a $7 \times 7 < k_{ro}, k_{pey} >$ kernel. Figure A.2 shows the result for the full FOV dataset. Thresholding for the eigenvalues of $\approx 1$ ($> 0.98$) provides exact outline of the brain anatomy. The resulting eigenvector for each pixel's first eigenvalue gives the sensitivity profile of each channel. You can see the matching rows of the first and bottom rows.

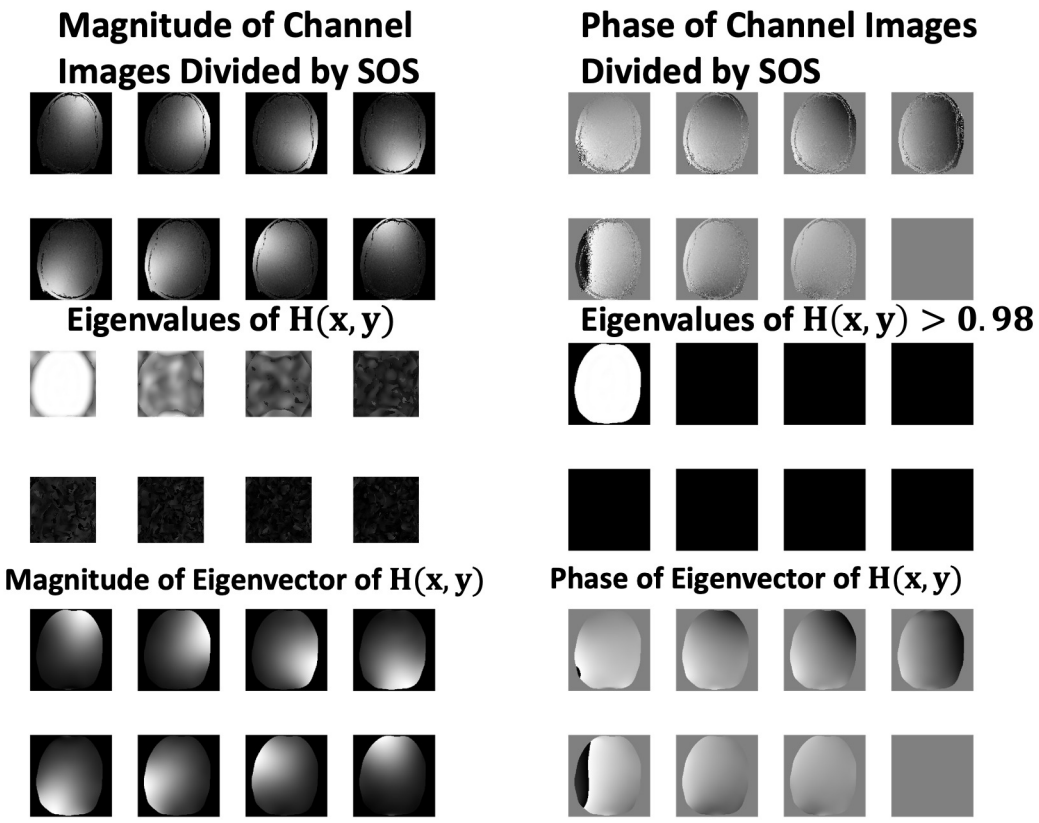


*Figure A.2: Top shows the magnitude and the phase of the individual channel images being divided by the square root sum of squares of the entire dataset. Middle left shows the eigenvalues of the harmonic matrix, $H(x, y)$, of equation A.8. The middle right shows only the eigenvalues $> 0.98$ . Notice only the shape of the anatomy is left over. The bottom row shows the magnitude and the phase of the eigenvectors of $H(x, y)$.*

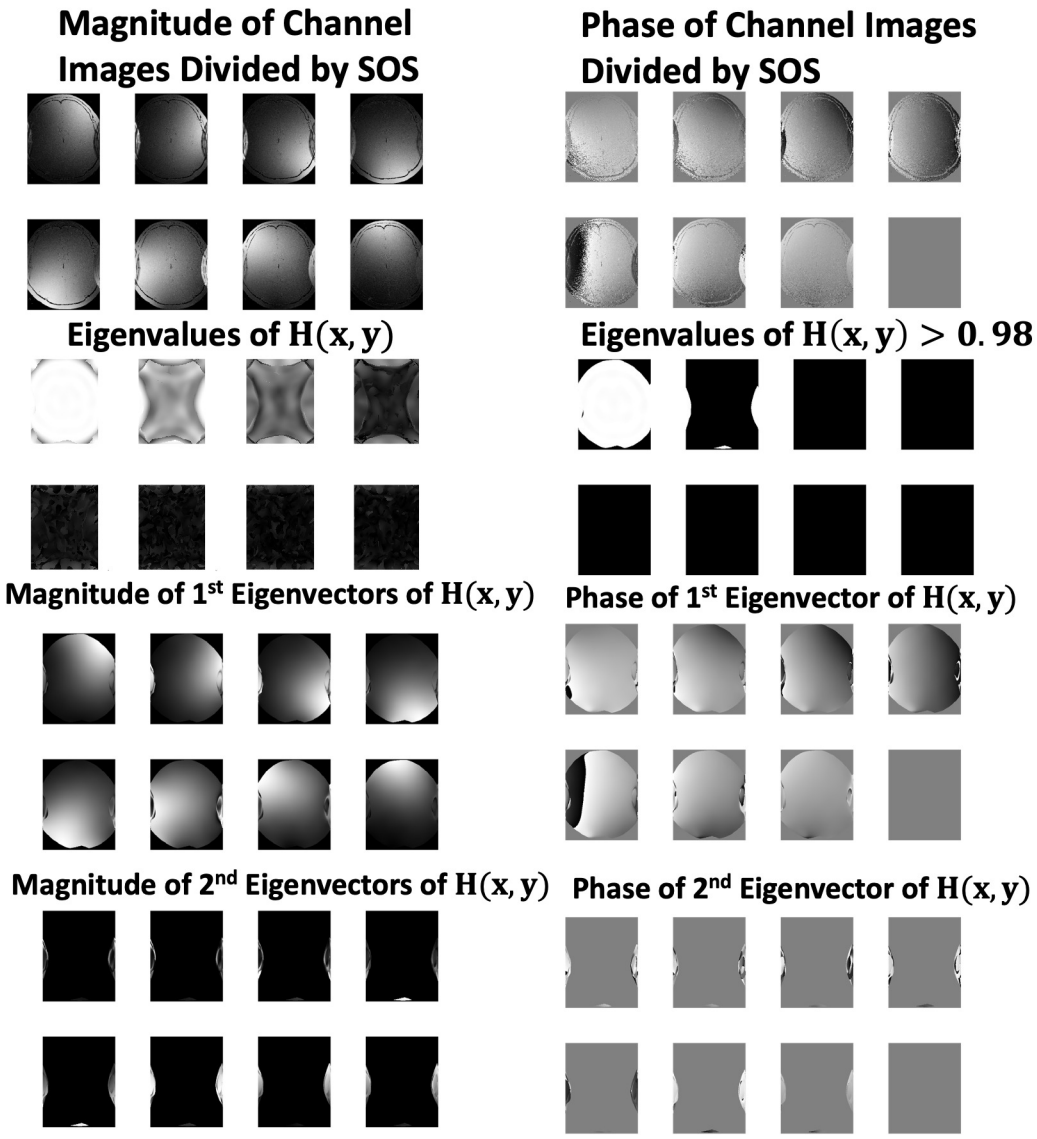


*Figure A.3: Top shows the magnitude and the phase of the individual channel images being divided by the square root sum of squares of the entire dataset. This time the FOV is reduced along the $\hat{u}_{pey}$ direction, resulting in aliasing. The second row shows the eigenvalues of $H(x, y)$. Where aliasing occurs, there is an overlap of two different anatomies, each with its own different channel sensitivities. You can think the channel sensitivity for a voxel located at $< x, y >$ being an $N_c \times 1$ channel vector. For this example of aliased anatomy, there are two distinct channel profiles for those aliased voxels. This results in two different eigenvectors that satisfy equation A.8, as is evidenced by the thresholded eigenvalues in the right half of the second row. The last two rows show the corresponding eigenvectors for each voxel for these two eigenvalue maps, which shows the aliased sensitivity profiles.*

Bibliography

[1] Khaled Alfakih et al. “Normal human left and right ventricular dimensions for MRI as assessed by turbo gradient echo and steady-state free precession imaging sequences”. In: *Journal of Magnetic Resonance Imaging: An Official Journal of the International Society for Magnetic Resonance in Medicine* 17.3 (2003), pp. 323–329.

[2] F Ali, JP Finn, and M Bydder. “Using SMASH Spatial Harmonics to Slice-Encode Outflow Artefacts in bSSFP Imaging.” In: *Proceedings of the 31st Annual Meeting of ISMRM, Toronto, Canada*. 2023, p. 7398.

[3] Fadil Ali et al. “Slice encoding for the reduction of outflow signal artifacts in cine balanced SSFP imaging”. In: *Magnetic resonance in medicine* 86.4 (2021), pp. 2034–2048.

[4] David C Alsop and John A Detre. “Reduced transit-time sensitivity in noninvasive magnetic resonance imaging of human cerebral blood flow”. In: *Journal of Cerebral Blood Flow & Metabolism* 16.6 (1996), pp. 1236–1249.

[5] Weston A. Anderson. “Electrical Current Shims for Correcting Magnetic Fields”. In: *Review of Scientific Instruments* 32.3 (Mar. 1961), pp. 241–250. DOI: 10.1063/1.1717338.

[6] David G Armstrong, Lawrence A Lavery, and Lawrence B Harkless. “Validation of a diabetic wound classification system: the contribution of depth, infection, and ischemia to risk of amputation”. In: *Diabetes care* 21.5 (1998), pp. 855–859.

[7] Jonathan Arnold and Valerie L Marmolejo. “Interpretation of near-infrared imaging in acute and chronic wound care”. In: *Diagnostics* 11.5 (2021), p. 778.

[8] Danny Barash and Matan Gavish. “Optimal shrinkage of singular values under random data contamination”. In: *Advances in Neural Information Processing Systems* 30 (2017).

[9] O Bieri and K Scheffler. "Flow compensation in balanced SSFP sequences". In: *Magnetic Resonance in Medicine: An Official Journal of the International Society for Magnetic Resonance in Medicine* 54.4 (2005), pp. 901–907.

[10] Oliver Bieri, Michael Markl, and Klaus Scheffler. "Analysis and compensation of eddy currents in balanced SSFP". In: *Magnetic Resonance in Medicine: An Official Journal of the International Society for Magnetic Resonance in Medicine* 54.1 (2005), pp. 129–137.

[11] F. Bloch. "Nuclear Induction". In: *Phys. Rev.* 70 (7-8 Oct. 1946), pp. 460–474. DOI: 10.1103/PhysRev.70.460. URL: https://link.aps.org/doi/10.1103/PhysRev.70.460.

[12] Fbys Bloch. "Dynamical theory of nuclear induction. II". In: *Physical Review* 102.1 (1956), p. 104.

[13] Andrew JM Boulton et al. "The global burden of diabetic foot disease". In: *The Lancet* 366.9498 (2005), pp. 1719–1724.

[14] Felix A Breuer et al. "Controlled aliasing in parallel imaging results in higher acceleration (CAIPIRINHA) for multi-slice imaging". In: *Magnetic Resonance in Medicine: An Official Journal of the International Society for Magnetic Resonance in Medicine* 53.3 (2005), pp. 684–691.

[15] Felix A Breuer et al. "Controlled aliasing in volumetric parallel imaging (2D CAIPIRINHA)". In: *Magnetic Resonance in Medicine: An Official Journal of the International Society for Magnetic Resonance in Medicine* 55.3 (2006), pp. 549–556.

[16] Mark Bydder and Jiang Du. "Noise reduction in multiple-echo data sets using singular value decomposition". In: *Magnetic resonance imaging* 24.7 (2006), pp. 849–856.

[17] Mark Bydder, David J Larkman, and Joseph V Hajnal. "Generalized SMASH imaging". In: *Magnetic Resonance in Medicine: An Official Journal of the International Society for Magnetic Resonance in Medicine* 47.1 (2002), pp. 160–170.

[18] Mark Bydder et al. “Low rank off-resonance correction for double half-echo k-space acquisitions”. In: *Magnetic Resonance Imaging* 94 (2022), pp. 43–47.

[19] Mark Bydder et al. “Minimizing echo and repetition times in magnetic resonance imaging using a double half-echo k-space acquisition and low-rank reconstruction”. In: *NMR in Biomedicine* 34.4 (2021), e4458.

[20] Mark Bydder et al. “Trimmed autocalibrating k-space estimation based on structured matrix completion”. In: *Magnetic Resonance Imaging* 43 (2017), pp. 88–94.

[21] James A Cadzow. “Signal enhancement-a composite property mapping algorithm”. In: *IEEE Transactions on Acoustics, Speech, and Signal Processing* 36.1 (1988), pp. 49–62.

[22] Jian-Feng Cai, Tianming Wang, and Ke Wei. “Fast and provable algorithms for spectrally sparse signal reconstruction via low-rank Hankel matrix completion”. In: *Applied and Computational Harmonic Analysis* 46.1 (2019), pp. 94–121.

[23] Emmanuel J Candes and Yaniv Plan. “Matrix completion with noise”. In: *Proceedings of the IEEE* 98.6 (2010), pp. 925–936.

[24] James C Carr et al. “Cine MR angiography of the heart with segmented true fast imaging with steady-state precession”. In: *Radiology* 219.3 (2001), pp. 828–834.

[25] Stephen F Cauley et al. “Interslice leakage artifact reduction technique for simultaneous multislice acquisitions”. In: *Magnetic resonance in medicine* 72.1 (2014), pp. 93–102.

[26] L Chen et al. “Measurements of T1 relaxation times at 3.0 T: implications for clinical MRA”. In: *Proceedings of the 9th Annual Meeting of ISMRM, Glasgow, Scotland*. 2001, p. 1391.

[27] Nathaniel Chiang et al. “Evaluation of hyperspectral imaging technology in patients with peripheral vascular disease”. In: *Journal of Vascular Surgery* 66.4 (2017), pp. 1192–1201.

[28] Michael S Conte et al. “Global vascular guidelines on the management of chronic limb-threatening ischemia”. In: *European Journal of Vascular and Endovascular Surgery* 58.1 (2019), S1–S109.

[29] Weiying Dai et al. “Continuous flow-driven inversion for arterial spin labeling using pulsed radio frequency and gradient fields”. In: *Magnetic Resonance in Medicine: An Official Journal of the International Society for Magnetic Resonance in Medicine* 60.6 (2008), pp. 1488–1497.

[30] Anjali Datta et al. “Mitigation of near-band balanced steady-state free precession through-plane flow artifacts using partial dephasing”. In: *Magnetic resonance in medicine* 79.6 (2018), pp. 2944–2953.

[31] Bart De Moor. “The singular value decomposition and long and short spaces of noisy matrices”. In: *IEEE transactions on signal processing* 41.9 (1993), pp. 2826–2838.

[32] Vibhas S Deshpande, Steven M Shea, and Debiao Li. “Artifact reduction in true-FISP imaging of the coronary arteries by adjusting imaging frequency”. In: *Magnetic Resonance in Medicine: An Official Journal of the International Society for Magnetic Resonance in Medicine* 49.5 (2003), pp. 803–809.

[33] Masoud Edalati et al. “Intravenous contrast-free standardized exercise perfusion imaging in diabetic feet with ulcers”. In: *Journal of Magnetic Resonance Imaging* 50.2 (2019), pp. 474–480.

[34] J Paul Finn et al. “Cardiac MR imaging: state of the technology”. In: *Radiology* 241.2 (2006), pp. 338–354.

[35] Christopher J François et al. “Left ventricular mass: manual and automatic segmentation of true FISP and FLASH cine MR images in dogs and pigs”. In: *Radiology* 230.2 (2004), pp. 389–395.

[36] Allen N Garroway, Peter K Grannell, and Peter Mansfield. "Image formation in NMR by a selective irradiative process". In: *Journal of Physics C: Solid State Physics* 7.24 (1974), p. L457.

[37] Matan Gavish and David L Donoho. "Optimal shrinkage of singular values". In: *IEEE Transactions on Information Theory* 63.4 (2017), pp. 2137–2152.

[38] Jonathan Gillard. "Cadzow's basic algorithm, alternating projections and singular spectrum analysis". In: *Statistics and its Interface* 3.3 (2010), pp. 335–343.

[39] Gary H Glover. "3D z-shim method for reduction of susceptibility effects in BOLD fMRI". In: *Magnetic Resonance in Medicine: An Official Journal of the International Society for Magnetic Resonance in Medicine* 42.2 (1999), pp. 290–299.

[40] Gary H Glover. "Phase-offset multiplanar (POMP) volume imaging: a new technique". In: *Journal of Magnetic Resonance Imaging* 1.4 (1991), pp. 457–461.

[41] Surya C Gnyawali et al. "High-resolution harmonics ultrasound imaging for non-invasive characterization of wound healing in a pre-clinical swine model". In: *PloS one* 10.3 (2015), e0122327.

[42] Richard J Goodall et al. "Current status of noninvasive perfusion assessment in individuals with diabetic foot ulceration". In: *Journal of Vascular Surgery* 69.2 (2019), pp. 315–317.

[43] Mark A Griswold et al. "Generalized autocalibrating partially parallel acquisitions (GRAPPA)". In: *Magnetic Resonance in Medicine: An Official Journal of the International Society for Magnetic Resonance in Medicine* 47.6 (2002), pp. 1202–1210.

[44] E Mark Haacke and Jens Frahm. *A guide to understanding key aspects of fast gradient-echo imaging*. 1991.

[45] EM Haacke and JA Tkach. "Fast MR imaging: techniques and clinical applications." In: *AJR. American journal of roentgenology* 155.5 (1990), pp. 951–964.

[46] Justin P Haldar. "AC-LORAKS: Autocalibrated Low-Rank Modeling of Local k-Space Neighborhoods". In: *Proc. Intl. Soc. Mag. Reson. Med.* Vol. 23. 2015, p. 2430.

[47] Justin P Haldar. "Autocalibrated LORAKS for fast constrained MRI reconstruction". In: *2015 IEEE 12th International Symposium on Biomedical Imaging (ISBI)*. IEEE. 2015, pp. 910–913.

[48] Justin P Haldar. "Low-rank modeling of local $k$-space neighborhoods (LORAKS) for constrained MRI". In: *IEEE transactions on medical imaging* 33.3 (2013), pp. 668–681.

[49] Justin P Haldar and Jingwei Zhuo. "P-LORAKS: low-rank modeling of local k-space neighborhoods with parallel imaging data". In: *Magnetic resonance in medicine* 75.4 (2016), pp. 1499–1514.

[50] Christopher J Hardy et al. "128-channel body MRI with a flexible high-density receiver-coil array". In: *Journal of Magnetic Resonance Imaging: An Official Journal of the International Society for Magnetic Resonance in Medicine* 28.5 (2008), pp. 1219–1225.

[51] Brian A Hargreaves et al. "Accelerated slice encoding for metal artifact correction". In: *Journal of Magnetic Resonance Imaging: An Official Journal of the International Society for Magnetic Resonance in Medicine* 31.4 (2010), pp. 987–996.

[52] Robin M Heidemann et al. "VD-AUTO-SMASH imaging". In: *Magnetic Resonance in Medicine: An Official Journal of the International Society for Magnetic Resonance in Medicine* 45.6 (2001), pp. 1066–1074.

[53] Luis Hernandez-Garcia, Anish Lahiri, and Jonas Schollenberger. "Recent progress in ASL". In: *Neuroimage* 187 (2019), pp. 3–16.

[54] RJ Hinchliffe et al. "IWGDF guidance on the diagnosis, prognosis and management of peripheral artery disease in patients with foot ulcers in diabetes". In: *Diabetes/metabolism research and reviews* 32 (2016), pp. 37–44.

[55] Peter M Jakob et al. “AUTO-SMASH: a self-calibrating technique for SMASH imaging”. In: *Magnetic Resonance Materials in Physics, Biology and Medicine* 7 (1998), pp. 42–54.

[56] Søren Holdt Jensen et al. “Reduction of broad-band noise in speech by truncated QSVD”. In: *IEEE Transactions on speech and audio processing* 3.6 (1995), pp. 439–448.

[57] Do-Young Jung et al. “A comparison in the muscle activity of the abductor hallucis and the medial longitudinal arch angle during toe curl and short foot exercises”. In: *Physical Therapy in Sport* 12.1 (2011), pp. 30–35.

[58] Daeun Kim et al. “Region-optimized virtual (ROVir) coils: Localization and/or suppression of spatial regions using sensor-domain beamforming”. In: *Magnetic Resonance in Medicine* 86.1 (2021), pp. 197–212.

[59] Adam Landsman. “Visualization of Wound Healing Progression With Near Infrared Spectroscopy: A Retrospective Study.” In: *Wounds: a Compendium of Clinical Research and Practice* 32.10 (2020), pp. 265–271.

[60] David J Larkman et al. “Use of multicoil arrays for separation of signal from multiple slices simultaneously excited”. In: *Journal of Magnetic Resonance Imaging: An Official Journal of the International Society for Magnetic Resonance in Medicine* 13.2 (2001), pp. 313–317.

[61] Gerhard A Laub. “Time-of-flight method of MR angiography.” In: *Magnetic resonance imaging clinics of North America* 3.3 (1995), pp. 391–398.

[62] Paul C Lauterbur. “Image formation by induced local interactions: examples employing nuclear magnetic resonance”. In: *nature* 242.5394 (1973), pp. 190–191.

[63] Dongwook Lee et al. “Acceleration of MR parameter mapping using annihilating filter-based low rank hankel matrix (ALOHA)”. In: *Magnetic resonance in medicine* 76.6 (2016), pp. 1848–1864.

[64] Peiying Liu et al. “T1 and T2 values of human neonatal blood at 3 Tesla: dependence on hematocrit, oxygenation, and temperature”. In: *Magnetic resonance in medicine* 75.4 (2016), pp. 1730–1735.

[65] Wenmiao Lu et al. “SEMAC: slice encoding for metal artifact correction in MRI”. In: *Magnetic Resonance in Medicine: An Official Journal of the International Society for Magnetic Resonance in Medicine* 62.1 (2009), pp. 66–76.

[66] Michael Lustig, David Donoho, and John M Pauly. “Sparse MRI: The application of compressed sensing for rapid MR imaging”. In: *Magnetic Resonance in Medicine: An Official Journal of the International Society for Magnetic Resonance in Medicine* 58.6 (2007), pp. 1182–1195.

[67] Michael Lustig and John M Pauly. “SPIRiT: iterative self-consistent parallel imaging reconstruction from arbitrary k-space”. In: *Magnetic resonance in medicine* 64.2 (2010), pp. 457–471.

[68] Ya-Jun Ma et al. “Improved SENSE imaging using accurate coil sensitivity maps generated by a global magnitude-phase fitting method”. In: *Magnetic resonance in medicine* 74.1 (2015), pp. 217–224.

[69] Julia K Mader et al. “Patients with healed diabetic foot ulcer represent a cohort at highest risk for future fatal events”. In: *Scientific reports* 9.1 (2019), p. 10325.

[70] Sagar Mandava et al. “Radial streak artifact reduction using phased array beamforming”. In: *Magnetic resonance in medicine* 81.6 (2019), pp. 3915–3923.

[71] Peter Mansfield and Peter K Grannell. “NMR’diffraction’in solids?” In: *Journal of Physics C: solid state physics* 6.22 (1973), p. L422.

[72] M Markl et al. “Flow effects in balanced steady state free precession imaging”. In: *Magnetic Resonance in Medicine: An Official Journal of the International Society for Magnetic Resonance in Medicine* 50.5 (2003), pp. 892–903.

[73] Michael Markl and Norbert J Pelc. "On flow effects in balanced steady-state free precession imaging: pictorial description, parameter dependence, and clinical implications". In: *Journal of Magnetic Resonance Imaging: An Official Journal of the International Society for Magnetic Resonance in Medicine* 20.4 (2004), pp. 697–705.

[74] Neil B Mascarenhas et al. "Fast 3D cine steady-state free precession imaging with sensitivity encoding for assessment of left ventricular function in a single breath-hold". In: *American Journal of Roentgenology* 187.5 (2006), pp. 1235–1239.

[75] Charles A McKenzie et al. "Coil-by-coil image reconstruction with SMASH". In: *Magnetic Resonance in Medicine: An Official Journal of the International Society for Magnetic Resonance in Medicine* 46.3 (2001), pp. 619–623.

[76] Daniel R Messroghli et al. "Modified Look-Locker inversion recovery (MOLLI) for high-resolution T1 mapping of the heart". In: *Magnetic Resonance in Medicine: An Official Journal of the International Society for Magnetic Resonance in Medicine* 52.1 (2004), pp. 141–146.

[77] Joseph L Mills Sr et al. "The society for vascular surgery lower extremity threatened limb classification system: risk stratification based on wound, ischemia, and foot infection (WIfI)". In: *Journal of vascular surgery* 59.1 (2014), pp. 220–234.

[78] Steen Moeller et al. "Multiband multislice GE-EPI at 7 tesla, with 16-fold acceleration using partial parallel imaging with application to high spatial and temporal whole-brain fMRI". In: *Magnetic resonance in medicine* 63.5 (2010), pp. 1144–1153.

[79] Stephan Morbach et al. "Long-term prognosis of diabetic foot patients and their limbs: amputation and death over the course of a decade". In: *Diabetes care* 35.10 (2012), pp. 2021–2027.

[80] M Ndosi et al. "Prognosis of the infected diabetic foot ulcer: a 12-month prospective observational study". In: *Diabetic Medicine* 35.1 (2018), pp. 78–88.

[81] K Nehrke, P Bornert, and C Stehning. "Flow-related problems in whole heart cine coronary MR angiography". In: *Proceedings of 14th Scientific Annual Meeting of the ISMRM, Seattle*. 2006.

[82] Reza Nezafat et al. "Inflow quantification in three-dimensional cardiovascular MR imaging". In: *Journal of Magnetic Resonance Imaging: An Official Journal of the International Society for Magnetic Resonance in Medicine* 28.5 (2008), pp. 1273–1279.

[83] Gregory Ongie and Mathews Jacob. "A fast algorithm for convolutional structured low-rank matrix recovery". In: *IEEE transactions on computational imaging* 3.4 (2017), pp. 535–550.

[84] A Oppelt et al. "FISP—a new fast MRI sequence". In: *Electromedica* 54.1 (1986), pp. 15–18.

[85] Joe Luis Pantoja et al. "Arterial spin labeling magnetic resonance imaging quantifies tissue perfusion around foot ulcers". In: *Journal of Vascular Surgery Cases, Innovations and Techniques* 8.4 (2022), pp. 817–824.

[86] Hiten M Patel et al. "Indocyanine green angiography to prognosticate healing of foot ulcer in critical limb ischemia: a novel technique". In: *Annals of Vascular Surgery* 51 (2018), pp. 86–94.

[87] Samuel Patz. "Steady-state free precession: an overview of basic concepts and applications". In: *Adv Magn Reson Imaging* 1 (1989), pp. 73–102.

[88] John Pauly, Dwight Nishimura, and Albert Macovski. "A k-space analysis of small-tip-angle excitation". In: *Journal of Magnetic Resonance (1969)* 81.1 (1989), pp. 43–56.

[89] Sven Plein et al. "Steady-state free precession magnetic resonance imaging of the heart: comparison with segmented k-space gradient-echo imaging". In: *Journal of*

*Magnetic Resonance Imaging: An Official Journal of the International Society for Magnetic Resonance in Medicine* 14.3 (2001), pp. 230–236.

[90] Klaas P Pruessmann et al. "SENSE: sensitivity encoding for fast MRI". In: *Magnetic Resonance in Medicine: An Official Journal of the International Society for Magnetic Resonance in Medicine* 42.5 (1999), pp. 952–962.

[91] E. M. Purcell, H. C. Torrey, and R. V. Pound. "Resonance Absorption by Nuclear Magnetic Moments in a Solid". In: *Phys. Rev.* 69 (1-2 Jan. 1946), pp. 37–38. DOI: 10.1103/PhysRev.69.37. URL: https://link.aps.org/doi/10.1103/PhysRev.69.37.

[92] S Rodriguez et al. "Diffuse optical images differentiate healing from non-healing wounds in diabetic foot ulcers". In: *Biomed. J. Sci. Tech. Res* 5 (2018), pp. 1–5.

[93] R Kevin Rogers et al. "Assessment of foot perfusion: Overview of modalities, review of evidence, and identification of evidence gaps". In: *Vascular Medicine* 25.3 (2020), pp. 235–245.

[94] Françoise Roméo and DI Hoult. "Magnet field profiling: analysis and correcting coil design". In: *Magnetic resonance in medicine* 1.1 (1984), pp. 44–65.

[95] Michael Schär et al. "Cardiac SSFP imaging at 3 Tesla". In: *Magnetic Resonance in Medicine: An Official Journal of the International Society for Magnetic Resonance in Medicine* 51.4 (2004), pp. 799–806.

[96] Klaus Scheffler. "A pictorial description of steady-states in rapid magnetic resonance imaging". In: *Concepts in Magnetic Resonance: An Educational Journal* 11.5 (1999), pp. 291–304.

[97] Klaus Scheffler and Jürgen Hennig. "Is TrueFISP a gradient-echo or a spin-echo sequence?" In: *Magnetic Resonance in Medicine: An Official Journal of the International Society for Magnetic Resonance in Medicine* 49.2 (2003), pp. 395–397.

[98] JF Schenck. "Quantitative analysis of intensity artifacts in spin-echo images produced by variations in magnetic susceptibility within the field of view: equations for the rapid determination of susceptibilities and analogies with catastrophe optics and optical caustic curves". In: *Proceedings of the 12th Annual Meeting of the Society for Magnetic Resonance in Medicine (SMRM)*. Vol. 14. 1993, p. 20.

[99] Kawin Setsompop et al. "Blipped-controlled aliasing in parallel imaging for simultaneous multislice echo planar imaging with reduced g-factor penalty". In: *Magnetic resonance in medicine* 67.5 (2012), pp. 1210–1224.

[100] Peter J Shin et al. "Calibrationless parallel imaging reconstruction based on structured low-rank matrix completion". In: *Magnetic resonance in medicine* 72.4 (2014), pp. 959–970.

[101] Stephanie M Shors et al. "Accurate quantification of right ventricular mass at MR imaging by using cine true fast imaging with steady-state precession: study in dogs". In: *Radiology* 230.2 (2004), pp. 383–388.

[102] Nalini Singh, David G Armstrong, and Benjamin A Lipsky. "Preventing foot ulcers in patients with diabetes". In: *Jama* 293.2 (2005), pp. 217–228.

[103] Daniel K Sodickson. "Tailored SMASH image reconstructions for robust in vivo parallel MR imaging". In: *Magnetic Resonance in Medicine: An Official Journal of the International Society for Magnetic Resonance in Medicine* 44.2 (2000), pp. 243–251.

[104] Daniel K Sodickson and Warren J Manning. "Simultaneous acquisition of spatial harmonics (SMASH): fast imaging with radiofrequency coil arrays". In: *Magnetic resonance in medicine* 38.4 (1997), pp. 591–603.

[105] Michael G Sowa et al. "Review of near-infrared methods for wound assessment". In: *Journal of biomedical optics* 21.9 (2016), pp. 091304–091304.

[106] Jolanda M Spijkerman et al. “T 2 mapping of cerebrospinal fluid: 3 T versus 7 T”. In: *Magnetic Resonance Materials in Physics, Biology and Medicine* 31 (2018), pp. 415–424.

[107] “Spin warp NMR imaging and applications to human whole-body imaging”. In: *Physics in medicine & biology* 25.4 (1980), p. 751.

[108] Subashini Srinivasan and Daniel B Ennis. “Optimal flip angle for high contrast balanced SSFP cardiac cine imaging”. In: *Magnetic resonance in medicine* 73.3 (2015), pp. 1095–1103.

[109] C Stehning et al. “Fast isotropic volumetric coronary MR angiography using free-breathing 3D radial balanced FFE acquisition”. In: *Magnetic Resonance in Medicine: An Official Journal of the International Society for Magnetic Resonance in Medicine* 52.1 (2004), pp. 197–203.

[110] Michael C Stoner et al. “Reporting standards of the Society for Vascular Surgery for endovascular treatment of chronic lower extremity peripheral artery disease”. In: *Journal of vascular surgery* 64.1 (2016), e1–e21.

[111] Pippa Storey et al. “Flow artifacts in steady-state free precession cine imaging”. In: *Magnetic Resonance in Medicine: An Official Journal of the International Society for Magnetic Resonance in Medicine* 51.1 (2004), pp. 115–122.

[112] Michael B Strauss et al. “Reliability Assessment of an Innovative Wound Score.” In: *Wounds: A Compendium of Clinical Research and Practice* 28.6 (2016), pp. 206–213.

[113] Shiteng Suo et al. “Evaluation of skeletal muscle microvascular perfusion of lower extremities by cardiovascular magnetic resonance arterial spin labeling, blood oxygenation level-dependent, and intravoxel incoherent motion techniques”. In: *Journal of Cardiovascular Magnetic Resonance* 20.1 (2018), pp. 1–14.

[114] R Developement Core Team. “R: A language and environment for statistical computing”. In: *(No Title)* (2010).

[115] Nicholas A Telischak, John A Detre, and Greg Zaharchuk. "Arterial spin labeling MRI: clinical applications in the brain". In: *Journal of Magnetic Resonance Imaging* 41.5 (2015), pp. 1165–1180.

[116] Hiroaki Terasaki et al. "A quantitative method for evaluating local perfusion using indocyanine green fluorescence imaging". In: *Annals of vascular surgery* 27.8 (2013), pp. 1154–1161.

[117] "The NMR phased array". In: *Magnetic resonance in medicine* 16.2 (1990), pp. 192–225.

[118] Martin Uecker et al. "ESPIRiT—an eigenvalue approach to autocalibrating parallel MRI: where SENSE meets GRAPPA". In: *Magnetic resonance in medicine* 71.3 (2014), pp. 990–1001.

[119] Sabine Van Huffel. "Enhanced resolution based on minimum variance estimation and exponential data modeling". In: *Signal processing* 33.3 (1993), pp. 333–355.

[120] Pim Van Ooij et al. "Age-related changes in aortic 3D blood flow velocities and wall shear stress: implications for the identification of altered hemodynamics in patients with aortic valve disease". In: *Journal of Magnetic Resonance Imaging* 43.5 (2016), pp. 1239–1249.

[121] Shawn M Verbout, Christine M Netishen, and Leslie M Novak. "Polarimetric techniques for enhancing SAR imagery". In: *Synthetic Aperture Radar*. Vol. 1630. SPIE. 1992, pp. 141–173.

[122] David O Walsh, Arthur F Gmitro, and Michael W Marcellin. "Adaptive reconstruction of phased array MR imagery". In: *Magnetic Resonance in Medicine: An Official Journal of the International Society for Magnetic Resonance in Medicine* 43.5 (2000), pp. 682–690.

[123] Jiongjiong Wang et al. “Arterial transit time imaging with flow encoding arterial spin tagging (FEAST)”. In: *Magnetic Resonance in Medicine: An Official Journal of the International Society for Magnetic Resonance in Medicine* 50.3 (2003), pp. 599–607.

[124] Zhen Wang et al. “A systematic review and meta-analysis of tests to predict wound healing in diabetic foot”. In: *Journal of vascular surgery* 63.2 (2016), 29S–36S.

[125] Felix W Wehrli, Jeffrey L Duerk, and Gregory C Hurst. *Fast-scan magnetic resonance-principles and applications. Felix W. Wehrli, PhD. New York: Raven Press, 1991.* 45.00*: pp 176: 91 figures*. 1991.

[126] Donald S Williams et al. “Magnetic resonance imaging of perfusion using spin inversion of arterial water.” In: *Proceedings of the National Academy of Sciences* 89.1 (1992), pp. 212–216.

[127] Eric C Wong, Richard B Buxton, and Lawrence R Frank. “Implementation of quantitative perfusion imaging techniques for functional brain mapping using pulsed arterial spin labeling”. In: *NMR in Biomedicine: An International Journal Devoted to the Development and Application of Magnetic Resonance In Vivo* 10.4-5 (1997), pp. 237–249.

[128] Wen-Chau Wu et al. “Hyperemic flow heterogeneity within the calf, foot, and forearm measured with continuous arterial spin labeling MRI”. In: *American Journal of Physiology-Heart and Circulatory Physiology* 294.5 (2008), H2129–H2136.

[129] Jian Zhang, Chunlei Liu, and Michael E Moseley. “Parallel reconstruction using null operations”. In: *Magnetic resonance in medicine* 66.5 (2011), pp. 1241–1253.

[130] Jie Zheng et al. “Non-contrast MRI perfusion angiosome in diabetic feet”. In: *European radiology* 25 (2015), pp. 99–105.

[131] Jie Zheng et al. “Oximetric angiosome imaging in diabetic feet”. In: *Journal of Magnetic Resonance Imaging* 44.4 (2016), pp. 940–946.